Low-cost Bench-Top Microfabrication of Nano/Microstructured Electrodes for Electrochemical Biosensing

Low-cost Bench-Top Microfabrication of Nano/Microstructured Electrodes for Electrochemical Biosensing

By Sokunthearath Kevin Saem, H.B.Sc.

A Thesis Submitted to the School of Graduate Studies in the Partial

Fulfillment of the Requirements for the Degree of PhD in Chemistry

McMaster University

PhD in Chemistry (2019)

Hamilton, Ontario (Department of Chemistry and Chemical Biology)

TITLE: Low-cost Bench-Top Microfabrication of Nano/Microstructured Electrodes for Electrochemical Biosensing

AUTHOR: Sokunthearath (Kevin) Saem (McMaster University)

SUPERVISOR: Dr. Jose Moran-Mirabal

NUMBER OF PAGES: XXII, 161

Abstract

The lack of safe drinking water, access to medical treatment and equipment, and sustainable energy are some examples of problems affecting the majority of developing nations today, and are collectively responsible for over 15 million annual deaths globally. While technological advances have enabled developed countries to improve the average health quality and overall life expectancy of their populations, the adoption of such technologies is cost-prohibitive for countries with small healthcare budgets. One of the obstacles in achieving low-cost and simple-to-use biotechnologies are versatile and robust fabrication methods. Therefore, there is great demand for novel and feasible biomedical device technologies that can address the current healthcare challenges of resource-limited nations.

In this thesis, a low-cost and rapid bench-top fabrication method is introduced to create nano/microstructured electrodes (NMSEs) with applications in microfluidic cell sensing, enhanced energy capture, and hemolytic agent detection. Metal deposition and viscoelastic shape-memory polymers were used to rapidly create highly tuneable wrinkled electrodes with electrochemical surface area enhancements of up to 650% and miniaturization down to 16% from the original area. These shrunken metallic electrodes were transferred onto polydimethylsiloxane (PDMS) using a dissolvable photoresist liftoff technique. The result was a new, all PDMS-based flexible microfluidic cell sensor, capable of detecting 3T3 fibroblast cells down to $2\text{x}10^6$ cells/ml and able to withstand flowrates of up to 100 mL/min. In a second project, biofilms of *Geobacter sulfurreducens* were cultured onto wrinkled NMSEs with enhanced electroactive surface area, which served as bioanodes in a microbial fuel cell. This enhanced microbial fuel cell generated twice the power output of control devices containing planar electrodes in lieu of the larger wrinkled variety. Next, we developed a phospholipid membrane-on-a-chip platform for the electrochemical detection of membrane disrupting agents. We deposited a coating of 1,2-dimyristoyl-sn-glycero-3-phosphocholine (DMPC) phospholipids on the surface of the NMSEs to inhibit charge transfer between the redox reporter molecule in solution and the electrode. Lytic compounds were hypothesized to disrupt the coating, such that the exposed NMSE interface could facilitate the monitoring of the signal transduction from redox molecules in solution. A first round of experiments tested the DMPC-coated NMSEs against commercially available sodium dodecyl sulfate (SDS) and Polymyxin-B (PmB), an antibiotic known to cause membrane rupture through dissolution and pore formation. The results indicated viable devices with limits of detection at 10 ppm and 1 ppm for SDS and PmB respectively. Lastly, we added cholesterol to the DMPC phospholipids to create stable supported membranes on NMSEs. The addition of cholesterol to DMPC increased the supported membrane stability against SDS and PmB where pure DMPC membranes produce higher signal recovery than cholesterol rich membranes. As a proof-of-concept, we tested the cholesterol rich membranes against Pneumolysin (PLY), a hemolytic protein known to rupture cell membranes. The LOD of SDS, PmB, and PLY was determined to be 500 ppm, 1 ppm, and 600 ppb respectively. All three electroanalytical devices produced using our shape-memory polymer structuring technique exemplify the potential of this versatile platform to help address the issues currently facing developing countries.

Acknowledgements

It is in my core belief that there is no such a thing as a self-made man. To quote a curious thinker Isaac Newton, "If I have seen further it is by standing on the shoulders of Giants." I am extremely fortunate to be surrounded by loving, caring, and talented people. To thank everyone would require a second thesis, but there are key individuals who must be recognised.

First to my supervisor, Dr. Jose M. Moran-Mirabal, who took a chance on me 5 years ago and helped me rediscover my childhood curiosity for science. Jose's unpretentious genius, honesty, integrity, caring nature, and passion for science always amazes and inspires me. He has set the standard extremely high as a supervisor, leader, and mentor that is deserving of emulation. Throughout our time together, Jose has taught me more than how to do good science. He has always presented me with challenges and opportunities that has changed my life forever. Jose has become more than my supervisor, he is my mentor and a lifelong friend. I have great respect and admiration for Jose and while I have a long journey ahead, I will forever cherish our experiences together in memory and hold his lessons close to heart. Thank you, Jose. Thank you to my incredibly supportive committee team. Dr. Alex Adronov for co-supervising me on my undergraduate thesis, which sparked the fire in me to pursue my doctoral studies. Dr. Michael Brook for his passion in chemistry that got me excited to attend 7:30 am classes in undergrad. Thank you all for always being there whenever you are needed.

My deepest gratitude must go to my parents for all of the sacrifices they have made and without whom; I would not be the man I am today. I have a lot of growing to do and hope to make you proud. Your unconditional love and life lessons are my greatest gifts. To Dora who has been pivotal in my personal development over the past 5 years. You are the foundation of my success and a thank you is not enough to capture how important you are to me. Your love inspires me to be the best that I can be and I am incredibly blessed to have you in my life.

Lastly, to those who are unmentioned, you know exactly who you are. I want to thank you for your relentless friendship and support. It is a testament to how fortunate I am to have such caring people in my life. I am infinitely richer because of your love and care. I hope my future actions make you proud and thank you for always keeping me inspired.

Contents

List of Figures

Acronyms

NMSEs	Nano/microstructured electrode
μF	Microfluidics
PDMS	Polydimethylsiloxane
EASA	Electroactive surface area
DMPC	1,2-dimyristoyl-sn-glycero-3-phosphocholine
SDS	Sodium dodecyl sulfate
PmB	Polymyxin-B
WHO	World Health Organization
ECB	Electrochemical biosensor
S:N	Signal-to-noise ratio
PL	Photolithography
UME	Ultramicroelectrode
UMEA	Ultramicroelectrode array
BSA	Bovine serum albumin
PR	Photoresist
PS	Polystyrene
SMP	Shape-memory polymer
PVP	Polyvinyl pyrolidone
EIS	Electrochemical impedance spectroscopy
DPV	Differential pulse voltammetry
CV	Cyclic Voltammetry
CA	Chronoamperometry
CC	Chronocoulometry
NPV	Normal pulse voltammetry
DPV	Differential pulse voltammetry
SWV	Square wave voltammetry
NME	Nanostructured microelectrodes

CVD	Chemical vapor deposition
LOD	Limit of detection
NPG	Nanoporous gold
w-NPG	Wrinkled nanoporous gold
PC	Polycarbonate
PE	Polyethylene
LoC	Lab-on-a-chip
PoC	Point-of-care
WE	Working electrode
AE	Auxiliary electrode
RE	Reference electrode
DMSO	Dimethyl sulfoxide
DMEM	Dulbecco's modified eagle's medium
CFSE	5(6)-carboxyfluorescein diacetate N-succinimidyl ester
EAB	Electroactive biofilm
MFC	Microbial fuel cell
SEM	Scanning electron microscopy
RMS	Root mean square
SLB	Supported lipid bilayers
tBLM	Tethered bilayer membrane
IPA	Isopropanol
BLADE	Biological Large Angle Diffraction Experiment
RH	Relative humidity
KFeCy	Potassium ferrocyanide
HO	Herman's orientation
PLY	Pneumolysin
CHOL	Cholesterol
M-ECB	Membrane-based electrochemical biosensor
CMC	Critical micelle concentration
DLS	Dynamic light scattering

RCB	Red blood cell
LD_{50}	Median lethal dose
NIBS	Non-invasive backscattering
CBB	Coomassie Brilliant Blue G-250
LB	Lysogeny broth
IPTG	Isopropyl β-d-1-thiogalactopyranoside
HPLC	High-performance liquid chromatography
FPLC	Fast protein liquid chromatography
OD	Optical density
MoC-ECB	Membrane-on-a-Chip electrochemical biosensor

Our deepest fear is not that we are inadequate. Our deepest fear is that we are powerful beyond measure. It is our light, not our darkness, that most frightens us. Your playing small does not serve the world. There is nothing enlightened about shrinking so that other people won't feel insecure around you. We are all meant to shine as children do. It's not just in some of us; it is in everyone. And as we let our own lights shine, we unconsciously give other people permission to do the same. As we are liberated from our own fear, our presence automatically liberates others.

Marianne Williamson

Chapter 1: Bench-top Fabricated Nano/Microstructured Electrodes for Enhanced Electrochemical Biosensing

1.1. INTRODUCTION

1.1.1. A Cry for Innovation

Lack of safe drinking water, sustainable medical access, and sustainable energy are some examples of problems facing developing nations today. Such issues are responsible for 15 million annual deaths globally. According to the World Health Organization's (WHO) 2018 annual statistics report, the global life expectancy could be increased by up to 5 years if we could address these pressing health related issues. Primary barriers to medical access for developing countries include: (1) limited access to remote villages; (2) limited financial support from the government; and (3) lack of access and technical acumen for advanced medical tools and therapies. Health issues are exacerbated by the lack of clean drinking water, which resulted in approximately 870 000 deaths in 2016 alone. For some regions in Africa, this number represents a mortality rate four times greater than the global rate from similar causes.[1] A subset (100 000) of these deaths are a result of unintentional poisoning caused by contaminated water sources through pesticides, Kerosene, and household chemicals.[1] The regional mortality rates increase when other health risk factors characteristic of developing countries are considered. The burning of contaminant-laced fuel is one example, which speaks to the need for clean and sustainable energy sources. The result is 3.8 million deaths from non-communicable diseases such as stroke, heart disease, and cancer caused by household air pollution. Considerable work by governments, researchers, and businesses is required to bring the quality of life of people in developing countries to a standard comparable to that of developed nations. To this end, the WHO in advancing the global Sustainable Development Goals emphasizes the need to develop new sustainable technologies more accessible worldwide.

1.1.2. Electrochemical Biosensors (ECBs)

Electrochemical biosensors (ECBs) are analytical devices that allow tracking chemical processes by monitoring the exchange of electrons between two substances. They typically include a biological recognition element, which has specificity for a target molecule (i.e. the analyte),[2,3] and which is coupled to an electrochemical transducer (i.e. the electrode).[2,4–6] Some examples of bio-recognition elements are enzymes, antibodies, peptides, and nucleic acids.[4,5,7] Leland C. Clark first introduced enzymatic ECBs in the early 1960's in an easy to use electroanalytical handheld device for glucose monitoring in diabetic patients.[8,9] The success of Clarks' invention helped to save many lives and changed the way researchers approach biosensor development today. Electrochemical glucose sensors still dominate the biosensing market with over 60% of the market share. This is unsurprising, since ECBs are advantageous over conventional sensors due to their low fabrication cost, ease of use, rapid detection time, robustness, high specificity, quantitative data output, and small sample volume requirements.[2,10,11] However, ECBs have historically suffered from a lack of sensitivity compared to larger industrial scale technology, which has hindered the advancement of new ECB technologies.

ECBs typically use planar electrodes as transducers because they are easy to fabricate and have predictable electrochemical behavior (e.g. linear diffusion, uniform electric field, and capacitance). However, planar electrodes have relatively low signal-to-noise ratios (S:N) per unit area and are difficult to miniaturize without losing sensitivity. Therefore, structuring approaches have been used to modify flat electrodes to increase their electroactive surface area (EASA, which correlates with sensitivity) and tune their electrochemical properties.[12–17] Approaches used to modify the electrode topography include the use of shape memory polymers to create wrinkled metallic thin films,[18–21] micro porous electrodes,[16,21,22] nanoparticle electrodeposition,[23,24] and electrochemical roughening.[13] Other alternatives to enhance sensitivity include the use of photolithography techniques to reduce the electrode dimensions to extreme ratios that result in ultramicroelectrodes (UMEs) and ultramicroelectrode arrays (UMEAs), which exhibit a unique set of electrochemical properties different from macroscopic electrodes.[23–29]

1.1.3. Nano- and microstructured electrodes (NMSEs)

Nano- and microstructured electrodes (NMSEs) are electrodes that have topographical surface features with x-y-z dimensions that range from the nanometer to micrometer. Due to their small feature size, NMSEs have increased electroactive surface areas compared to their flat counterparts, and can be implemented in miniaturized platforms.[18,30] Some examples of reported NMSEs include 3D nanoporous metallic electrodes,[16,22,31] lithographically patterned ultramicroelectrode arrays (UMEAs),[26,32,33] 3D metallic nanorods,[34,35] and wrinkled metallic films.[12,21,36,37] The increased electroactive surface area allows electroanalytical chemists to design

ECBs with enhanced electrochemical signal (typically measured as total current output) and smaller footprints suitable for miniaturized platforms. In the case of surface functionalization with DNA, antibodies, proteins, and other small molecules, electrode surfaces with increased EASAs allow increased packing density of surface-bound bio-recognition elements.[15,38,39]

Porous metallic electrodes made by de-alloying,[40–42] electrodeposition,[22,43] sputter deposition,[44,45] and spray deposition[16] result in high electroactive surface area suitable for electrochemical applications. The fabrication of nanoporous 3D gold (Au) leaf electrodes has been previously reported with metallic sheets of a silver:gold (Ag:Au) alloy, followed by chemical etching of Ag in a concentrated nitric acid solution ($HNO_{3\,(aq)}$). The acid dissolves the Ag and leaves the inert porous Au structure behind (Figure 1.1). Large surface area nanoporous electrodes made in this way have been used in electrocatalysis[46,47] and heavy metal sensing applications.[48,49] Nanostructured porous Au electrodes have also been reported to exhibit improved anti-biofouling properties against transport proteins when compared to flat electrodes.[22] Blood transport proteins like human serum albumin (HSA) can cause electrode biofouling in devices used for clinical sample monitoring. In biosensors, this results in false signal generation or signal suppression , which makes them inaccurate. Small nanometre-sized pores in a 3D network can be used to prevent such fouling, because they restrict the migration of larger proteins into the porous network while still allowing access to small redox reporter molecules that generate the electrochemical signals.[50] Figure 1.2 shows a cartoon comparing the biofouling of planar Au electrodes and the minimal fouling seen on a nanoporous Au electrode. Based on the proposed mechanism, a prominent cyclic voltammogram signal would be maintained for a nanoporous Au electrode while biofouling from albumin would cause signal suppression for the planar Au electrode.

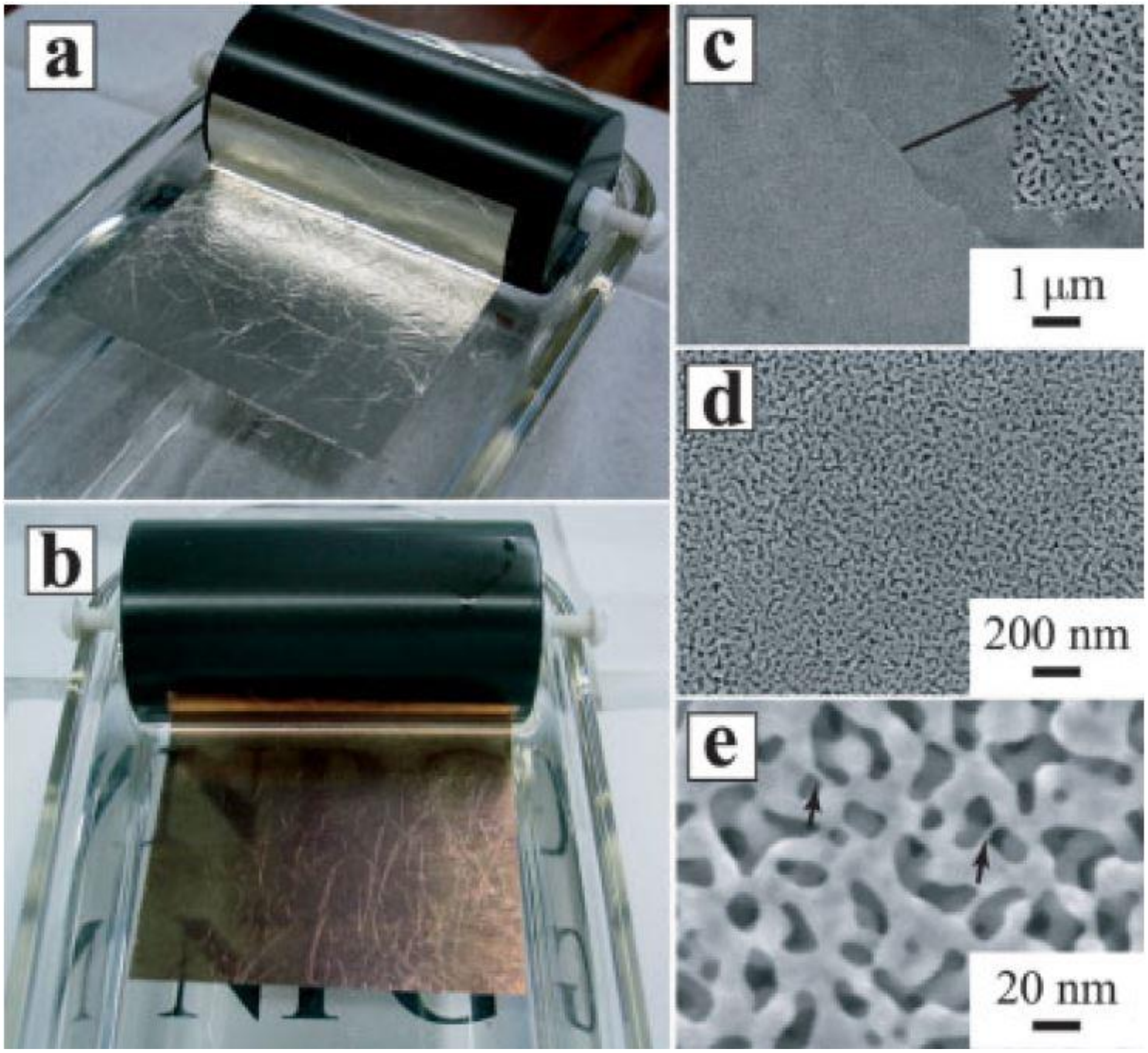

Figure 1.1. Optical images of white-gold leaf **(A)** before and **(B)** after nitric acid de-alloying, and (c, d, e) scanning electron micrographs of the nanoporous gold electrode at various magnifications. Adapted from Reference 31.

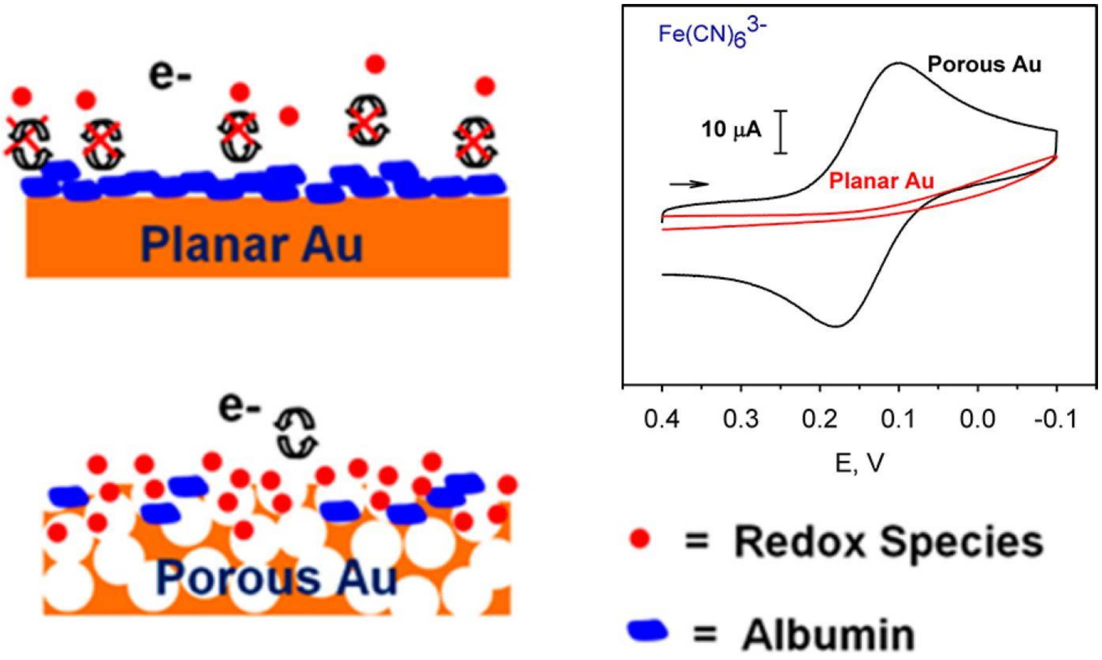

Figure 1.2. Diagram representing the biofouling of planar vs. nanoporous Au by albumin and the resulting effect on electrochemical signals produced by each device. The cyclic voltammogram shows that large redox peaks are observed for the nanoporous Au electrodes while the peaks are supressed for planar Au due to biofouling. Adapted from Reference 22.

In contrast to porous electrodes, ultramicroelectrodes (UMEs) benefit from having extremely small electrode dimensions. UMEs are electrodes with a tip diameter smaller than a critical dimension dictated by the electrochemical diffusion layer. Theoretical and empirical experiments have confirmed that operational UMEs must have critical dimensions smaller than 25 μm.[26,33,51] The ratio of the diffusion layer to the electrode size of UMEs give rise to interesting electrochemical properties such as increased signal-to-noise ratio (S:N), radial diffusion, and steady-state kinetics. According to the Randles-Sevcik model, the Faradaic signal current is proportional to $v^{\frac{1}{2}}$ (scan rate$^{1/2}$) while capacitive current (i.e. "noise" current) is linearly proportional to v.[52] Therefore, when using macroscale electrodes at a faster v, the large capacitive background current will overshadow the current of the Faradaic signal. This is not the concern with UMEs, in which the Faradic signal current can be separated from the noisy capacitive current. This results in the increased signal-to-noise ratios (S:N) that allow UMEs to be employed in environmental monitoring, for gas sensing, and in the detection of trace heavy metal contamination in water.[17,24,25]

In some instances, the low total current output can be challenging when trying to determine trace analyte concentrations, because the total signal intensity is low compared to that of a macroelectrode. Accordingly, arrays of UMEs (UMEAs) were developed to obtain higher total current output while maintaining the desirable microelectrode properties. Some groups have utilized traditional photolithography techniques to produce flat Au UMEAs, which were then modified with Au nanoparticles using electrodeposition.[17] Such electrode enhancements have been shown to preserve UMEA properties while enhancing the total electrochemical signal output of the device and increasing the range of the linear response for copper (II) detection.[17] Others have combined the concepts of surface area enhancement of porous 3D networks with UMEs to increase the efficiency of electrochemical devices.[53] Macroporous-UMEs were produced by coating an Au-wire tip with monodisperse colloidal silica particles followed by Au electrodeposition and removal of silica via hydrofluoric acid etching. An example of the resulting macroporous-UMEs is shown in Figure 1.3. Some limitations to these electrodes are their complex and expensive fabrication process, typically relying on traditional photolithography. Furthermore, UMEs can be fragile due to their small feature sizes and can be difficult to implement into medical devices that require robustness.

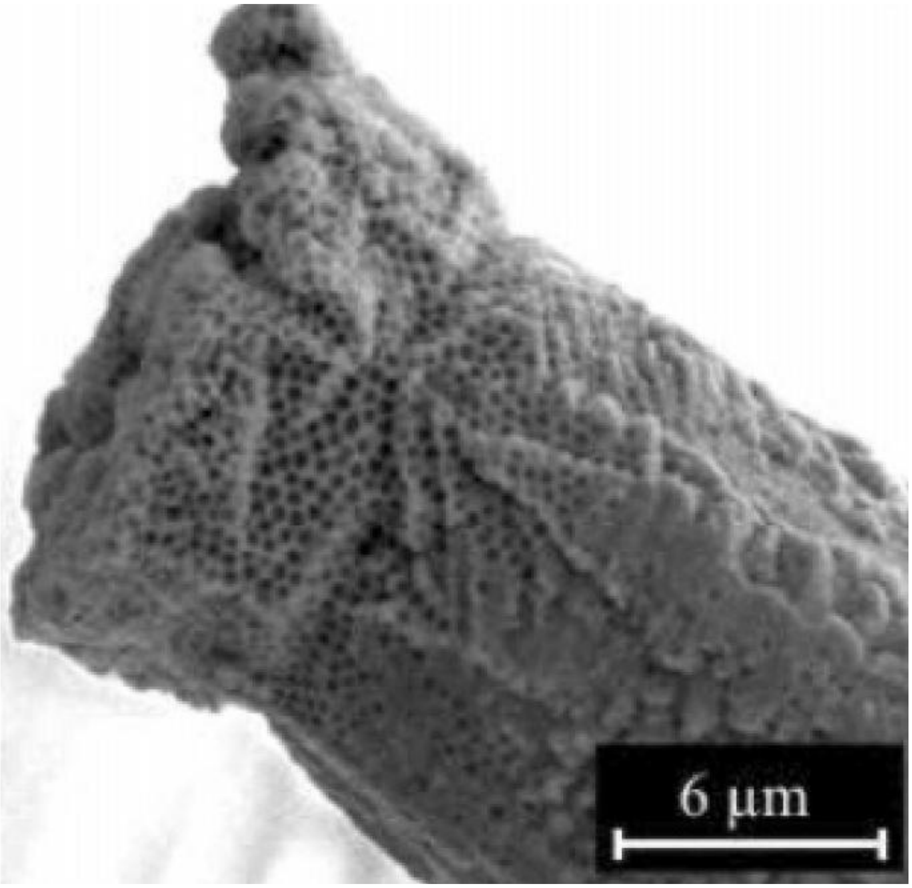

Figure 1.3. SEM image of a cylindrical macroporous-UME adapted from Reference 53.

While the biosensing community has traditionally employed photolithographic techniques to produce NMSEs, some researchers have proposed simpler and inexpensive fabrication techniques as ways to make these systems more accessible. Recently, bench-top microfabrication has captured the attention of the community as a low-cost alternative to traditional lithographic techniques. Bench-top fabrication, or microfabrication, refers to a set of processes that are simple enough for safe use on a laboratory bench to produce devices with critical feature sizes ranging from the submicron to the centimeter scale. Such processes can involve, but are not limited to, xurography, mask templating, computer numerical control machining, and additive manufacturing. Over the past two decades, bench-top microfabrication has been often linked to polydimethylsiloxane (PDMS) based soft lithography[54–56] and thermo-responsive polymer structuring techniques[12,57,58] where most, if not all, device assembly is performed on the bench-top. Some examples of processes involving soft lithography are the fabrication of microfluidic based biosensors,[37,58] capillary assembly and micro contact printing of microparticles and molecules. [54,59–61] Additionally, flexible PDMS substrates were one of the first substrates used in the fabrication of thermally-induced polymer nano/microstructuring of metallic thin films.[56,62] Despite the many strategies available for the fabrication of NMSEs, the remainder of this introduction will focus only on low cost bench-top methods and their application to make electrodes for biosensing and energy capture applications. The motivation behind this is the proven simplicity and efficacy of these techniques, which means they can be directly used in developing countries to decrease the overall cost related to the on-site fabrication of sensing devices. With their increased sensitivity, portability, and low cost, NMSEs offer a versatile platform for applications in biosensing, water purification, and sustainable energy capture. We believe bench-top microfabrication offers an excellent alternative to traditional lithography that is easily accessible to researchers in various disciplines, economically scalable, and feasible for the rapid prototyping of novel sensing technology.

1.2. HISTORY AND PRODUCTION OF WRINKLED NMSEs

1.2.1. Fascination with Wrinkles

The human fascination with wrinkled structures dates back to the ancient Egyptians, Chinese, Indians, and Greek civilizations with the prevention and treatment of human skin wrinkles. Skin wrinkles appear when external stress is applied to the skin or as a result of muscle movements. More specifically, the wrinkling of the skin is a result of the elastic modulus mismatch between the epidermis and dermis layers.[63] Because the skin is elastic, wrinkles tend to disappear upon relaxation or removal of the applied stress. The increase in skin thickness from sunlight exposure results in a large elastic modulus mismatch between the skin layers causing more prominent large wrinkle formation. This buckling/wrinkling phenomenon of stiff thin films on soft supporting materials has inspired researchers to design new wrinkled materials for applications in tissue engineering, biosensing, flexible electronics, templating, and enhanced energy capture.

1.2.2. Fabrication of wrinkled N-MSEs

Traditionally, NMSEs have been fabricated using photolithography techniques developed and matured by the semiconductor industry to make integrated circuits. The technique is highly tunable and allows the production of structures with feature sizes down to the nanometer range.[64–69] Typical photolithography techniques rely on the use of photosensitive polymers known in the industry as either negative or positive tone photoresists. Upon UV irradiation, negative tone resists will polymerize becoming insoluble in the alkaline developing solution. On the other hand, UV light will change the chemical structure in positive tone resists, thereby facilitating its solubilisation in the developing solution. Photoresists come in a range of molecular weights with higher molecular weight resist having higher viscosity. Higher molecular weight resists can be used to produce thicker layers and deeper patterns. Once a photoresist layer is patterned on a substrate, such as silicon wafer, metallic microelectrodes can be fabricated using techniques such as electron beam vapor deposition,[70] plasma sputter deposition,[18,19] or electrodeposition.[34,35,71,72] However, photolithography techniques require the use of cleanroom facilities, expensive equipment, highly trained technicians, and typically many fabrication steps. Therefore, researchers have recently explored simpler alternatives to microfabrication, especially when the applications do not require nanometer-size features.

1.2.3. Silicone Rubber Thermal Compression

One of the original bench-top methods used to produce wrinkled thin films was to use elastomeric PDMS as a thermo-responsive substrate.[63,64] In this approach, shown in Figure 1.4, metallic films as thin as 20 nm were deposited onto thermally expanded PDMS using vapour deposition. Subsequent cooling of the substrate resulted in a compressive stress in the system, where the mismatch in stiffness between the film and the substrate caused the former to buckle to relieve the applied stress. This resulted in the formation of ordered topographical structures that could be controlled and oriented.[62] An example of the controlled unidirectional Au wrinkles made through the thermally induced compression of PDMS substrates is shown in the optical micrograph in Figure 1.5. In the application shown, the PDMS was also patterned with steps, which upon thermal relaxation caused a larger compression strain to be applied perpendicularly to the top of the Au thin film. It has been reported that other features could be patterned to tune the feature sizes and periodicity of the wrinkled films.[62,63,73–75]

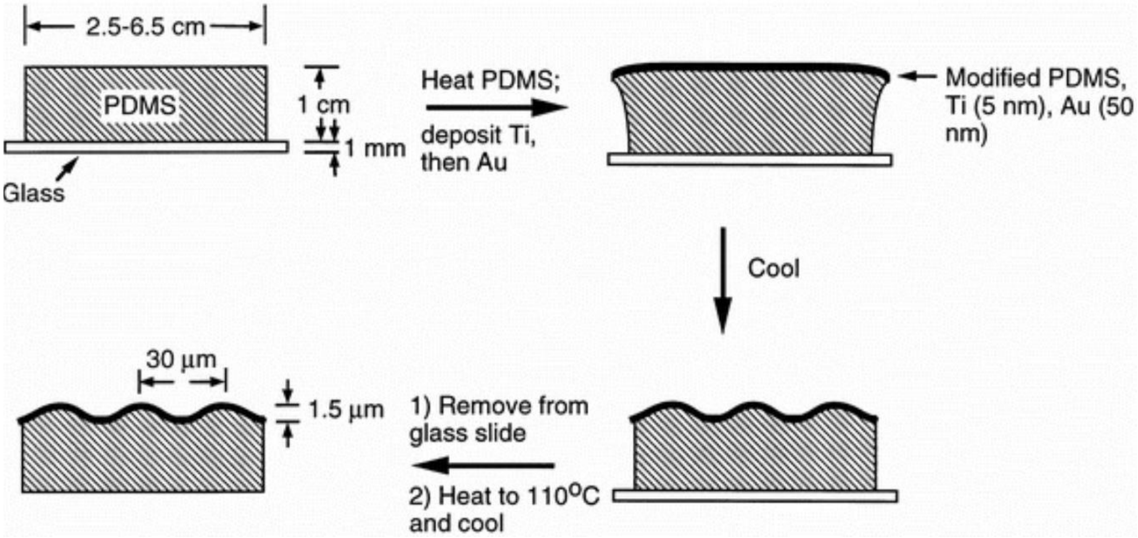

Figure 1.4. Diagram highlighting the thermal contraction induced buckling procedure that results in periodically wrinkled thin films. Adapted from Reference 62.

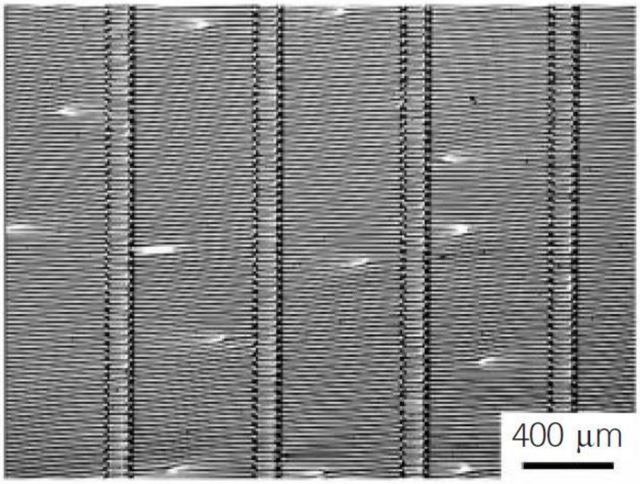

Figure 1.5. Optical micrograph of 50 nm thick Au wrinkled film on a PDMS substrate. Adapted from Reference 62.

One prevalent issue with PDMS-based microstructuring is the low interfacial adhesion of thin films to the silicon elastomer. Typically, this can be solved by adding a layer of chromium or titanium to the PDMS surface before depositing the metal of interest, albeit at the expense of increasing the number of fabrication steps and overall cost. The low material adhesion limits researchers from studying the intrinsic properties of the material of interest, since each additional material added contributes to the stiffness and thickness resulting in different wrinkle size and periodicity. The degree of shrinking of PDMS upon thermal relaxation is also limited and does not offer a large benefit in terms of size reduction. Therefore, alternative wrinkling methods that offer additional miniaturization benefits are desired to improve the applicability of this structuring method.

1.2.4. Shape-Memory Polymer Structuring

The limitations imposed by shrinking ratio and adhesion have led to the consideration of other thermally activated viscoelastic polymeric substrates to generate wrinkled films. In contrast to the buckling caused by the sequential thermal expansion and relaxation of the PDMS substrates, thermo-responsive pre-stressed polystyrene (PS) sheets can produce highly tunable biaxial and uniaxial compressive strain induced wrinkling.[12,18,57] PS sheets have been popularized as children's toys under the trademark "Shrinky Dinks", which can be decorated or cut into different designs before the polymer is baked in a cooking oven to induce shrinking. These are commercially produced by heating PS above 190 °C, and extruding it through a slot die to form 2.3 mm-thick slabs, which are further compressed between metal rollers and cooled to yield 254 – 300 μm thick pre-stressed PS sheets. The cooling process locks the stretched polymer chains in place. Once heated above the glass transition temperature (T_g) of 95 °C, the PS shrinks back into a smaller and thicker slab similar to the one produced by the slot die.

Understanding how thin rigid films buckle on top of soft materials can translate into better control over the periodicity of wrinkled structures and their size, as well as into methods to accurately assess an unknown thin film's physical properties. The theory behind the elastic buckling of rigid films has been developed,[77] from which it has been shown that a film of thickness h subjected to a small compressive stress produces periodic wrinkles with a wavelength $\lambda \propto \sqrt[3]{\eta}h$, where $\eta \propto \frac{Y_{film}}{Y_{sub}}$, Y_{film} and Y_{sub} are the Young's moduli for the rigid film and the substrate, respectively.[12] For the case of Au on PS, the Young's modulus is ~78 GPa for Au and ~3.5 GPa for PS.[78,79] This mismatch in stiffness justifies the formation of wrinkles on the Au film during the thermal shrinking of PS. Furthermore, large compressive stresses can lead to hierarchical wrinkles, where the first generation of wrinkles undergo additional wrinkling, something observed in the substrates depicted in Figure 1.6.

1.3. APPLICATIONS OF NANO AND MICROSTRUCTURED SURFACES

The past decade has experienced a surge of publications related to wrinkle thin film fabrication using pre-stressed polymer substrates. In 2008, we saw the implementation of shape-memory polymers (SMPs) in microfluidics and stem cell research.[58] One year later, SMPs were used to produce structured metallic electrodes for potential biomedical applications and studying cell membrane dynamics.[12] This work was further developed and led to the comprehensive electrochemical characterization of wrinkled electrodes, which exhibited enhanced EASAs as high as 665% and miniaturization down to 16% area compared to flat electrodes.[18] Figure 1.6 highlights how the variation in thin film roughness is influenced by Au thickness and shrinking temperature. These developments hinted at the promise of such structured electrodes for use in electrochemical-based detection, energy storage, photovoltaics, and tissue engineering.

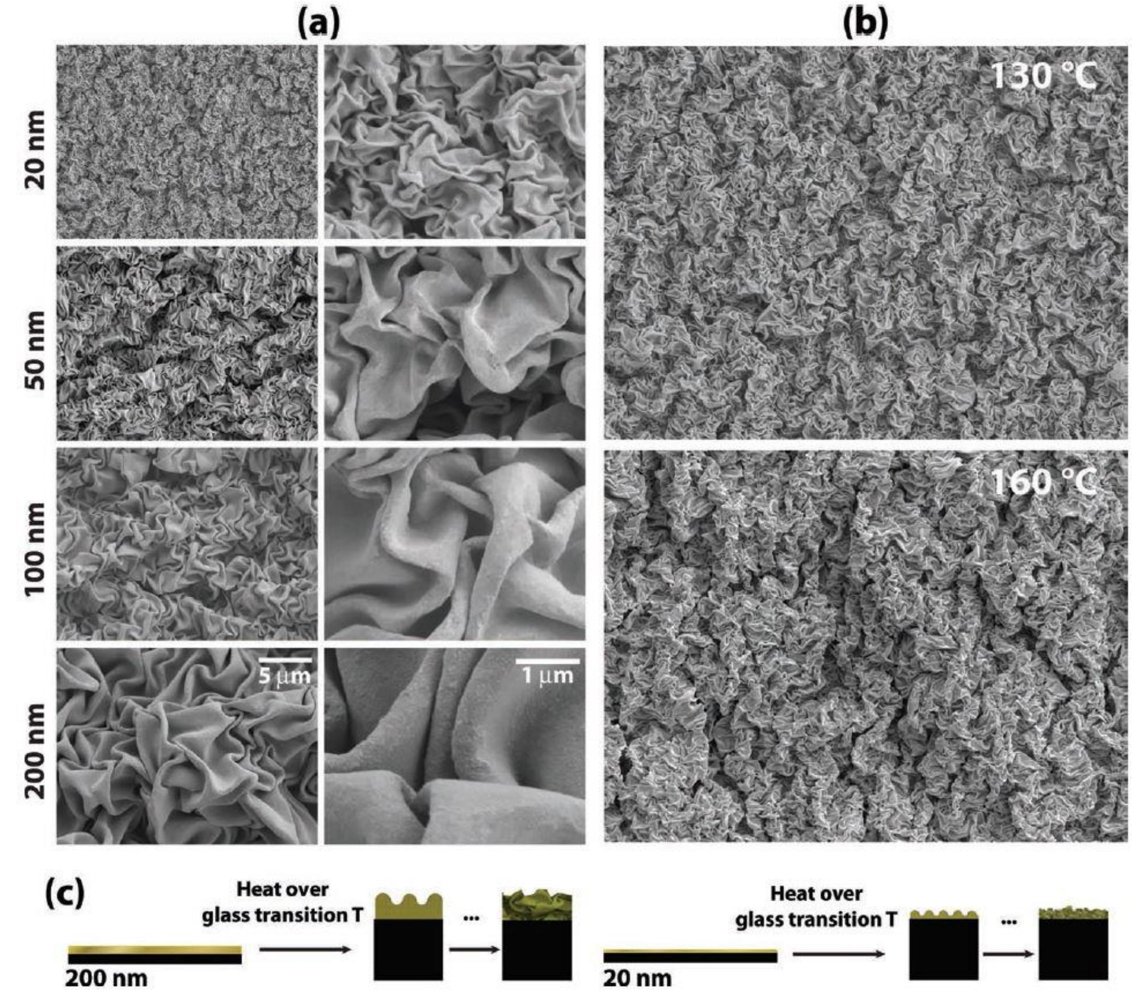

Figure 1.6. SEM images of Au thickness and roughness in response to **(A)** wrinkle size, and **(B)** shrinking at higher temperatures (which leads to rougher surfaces). Image **(C)** is a schematic representation of the thin film structuring process. Adapted from Reference 18.

Since their introduction, NMSEs have found use in many electrochemical biosensors and stretchable electronics applications. Nanostructured microelectrodes (NMEs, an alternative name for NMSEs) have been fabricated using a combination of standard photolithography, chemical vapor deposition (CVD), and electrodeposition, with the last governing electrode topography and size through the manipulation of electrodeposition time, reagent concentration, supporting electrolyte, and most importantly electroplating potential (Figure 1.7). Such nanostructuring significantly increases the EASA, resulting in highly sensitive NMEs suitable for nucleic acid sensors capable of rapid detection (< 30 min).[15,95]

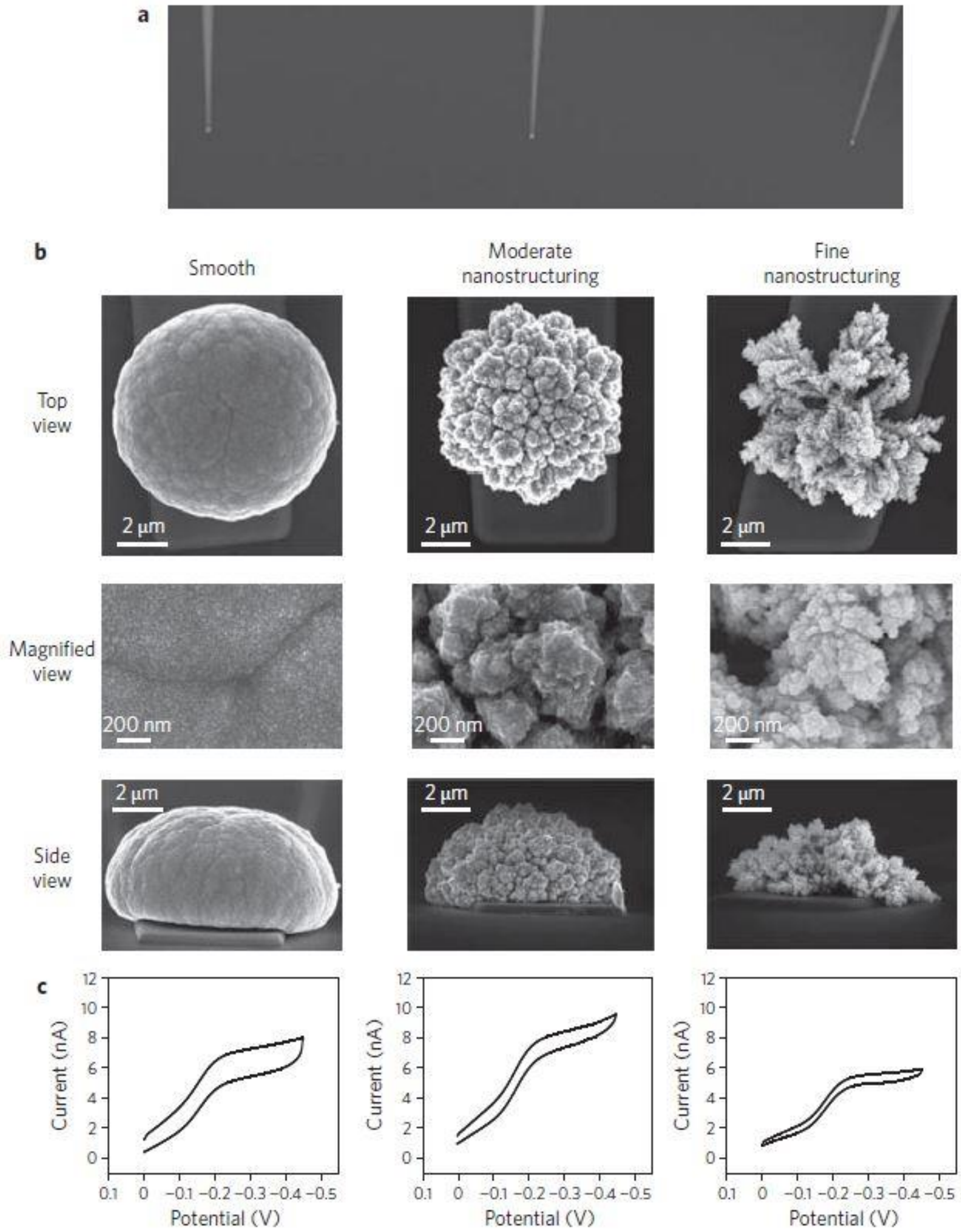

Figure 1.7. Comparison of the Pd NME nanostructuring produced using different electrodeposition conditions. **(A)** Three differently structured electrode tips containing the NMEs. **(B)** SEM images of differently structured NMEs. **(C)** Comparison of the electrochemical profile of NMEs in 3 mM $Ru(NH_3)_6^{3+}$ solution. Adapted from Reference 15.

Fine nanostructuring produces electrodes with improved S:N ratios where the background capacitance signal is much smaller than obtained with smooth electrodes. The improved S:N also produces cyclic voltammograms that exhibit an ultramicroelectrode like profile. The limit of detection (LOD) has been linked to the fineness of the nanostructuring in which finely structured NMEs (20-50 nm feature sizes) produced an LOD of 10 aM, moderately structured NMEs (100-300 nm feature sizes) had an LOD of 10 fM, and smooth structures exhibited an LOD of 100 fM. In DNA-based sensors, fine structures allow higher accessibility of the target molecules to immobilized DNA probes at the tips, which yields significant increases in hybridization efficiency. NMEs have also been adapted to multiplexed, label free immunosensing of ovarian cancer biomarker CA-125.[39] The NME sensors provided the small size needed for portability, while maintaining the LOD as low as 0.1 U/mL in human serum and whole blood.[38]

In addition to biosensing, wrinkled metallic electrodes have been used to make highly stretchable and bendable electrodes for potential applications in stretchable electronics and strain sensing. Wrinkled thin metallic films produced through heat induced polymer shrinking offer a low cost alternative to carbon nanotubes, graphene, and nanoparticle-based flexible conductors.[96] Using a dissolvable sacrificial layer as part of the fabrication step, planar Au films can be shrunken to form wrinkled electrodes that is subsequently transferred from the polystyrene (PS) to a receiving substrate through a solvent-induced lift-off process. This process is shown in Figure 1.8, where wrinkled Au films are transferred onto PDMS elastomer and silicon wafer substrates.

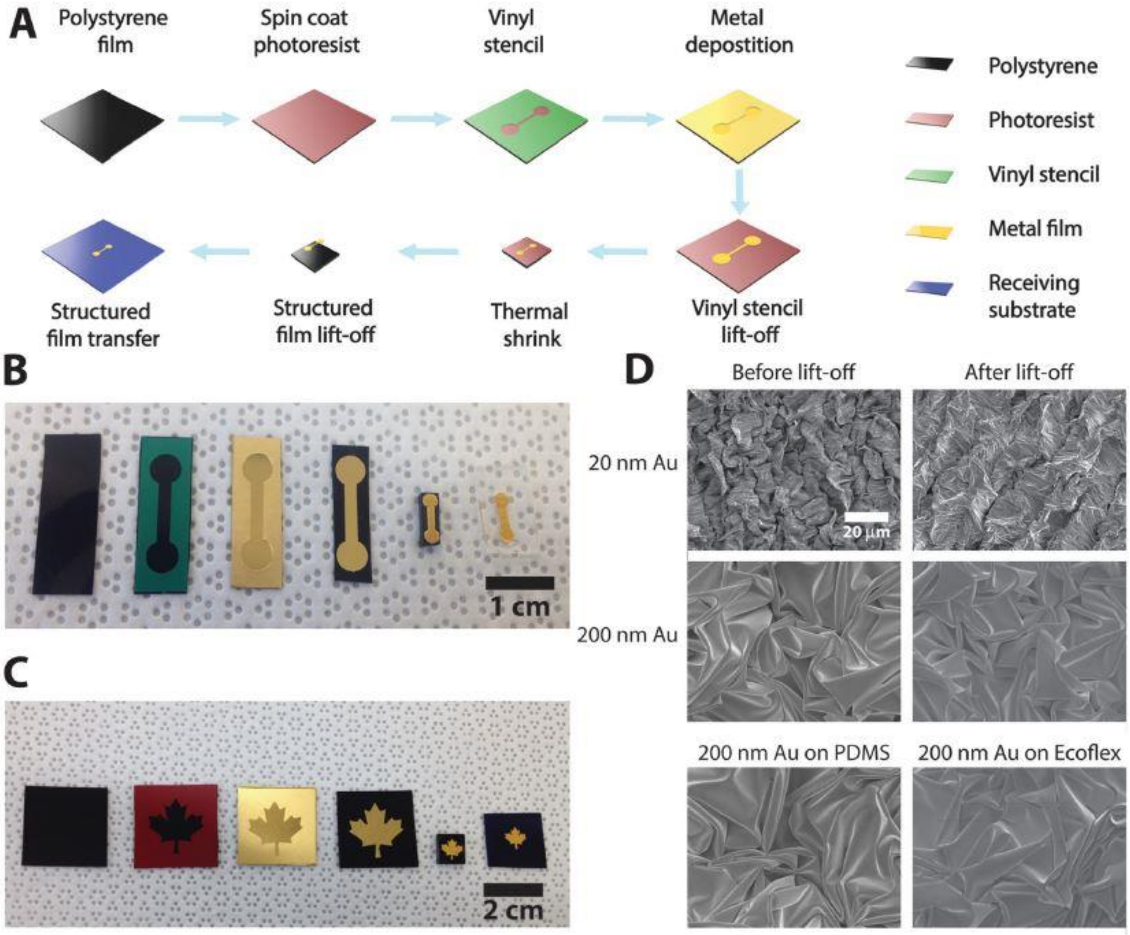

Figure 1.8. (A) Schematic of the fabrication process to make wrinkled metallic electrodes via thermally-induced shrinking. Images showing the intermediate steps in the wrinkled electrode transfer process onto **(B)** PDMS and **(C)** silicon wafer substrates. **(D)** SEM images of wrinkled electrodes made from different thickness Au films before and after lift-off and transfer onto PDMS and Ecoflex. Adapted from Reference 96.

Wrinkling preserves the structural stability of Au films allowing them to be manipulated by tweezers post lift-off without breaking. Wrinkled films transferred onto PDMS could be stretched up to 130% strain while maintaining conductivity, whereas their planar counterparts lost conductivity at < 5% strain. The random orientation of the wrinkles help to prevent crack propagation across the metallic film allowing wrinkled electrodes to withstand higher applied strains than the planar electrodes. Additionally, the PDMS wrinkled electrodes could be used to perform electrochemical sensing even under 30% applied strain, where similar signals were obtained from unstrained and strained devices.

Other studies have combined nanoporous Au films and thermal polymer shrinking techniques to produce highly tunable structured substrates for surface enhanced Raman scattering (SERS).[97] In this work, the silver from leaves made of $Au_{35}Ag_{65}$ alloy was chemically etched using 71% HNO_3, leaving behind a nanoporous gold (NPG) film (Figure 1.9 a-d). Subsequently, the NPG was transferred onto pre-stressed PS and heated to produce wrinkled nanoporous gold (w-NPGs) films (Figure 1.9 e-h). The nanopores in the Au structures served as electromagnetic "hot-spots" that amplified the Raman intensity of crystal violet and Rhodamine 6G a 100-fold compared to flat films. Furthermore, higher SERS signals were observed at the wrinkle ridges than at the valley, suggesting that SERS signals can be further enhanced if the density of ridges is increased. This work presented a simple method to produce highly tunable wrinkled porous substrates that exhibit SERS enhancements. Such large SERS enhancements should allow the production of highly sensitive assays for the detection of small molecules. In addition, the miniaturization of such substrates could allow the integration of other sensing techniques with electrochemistry.

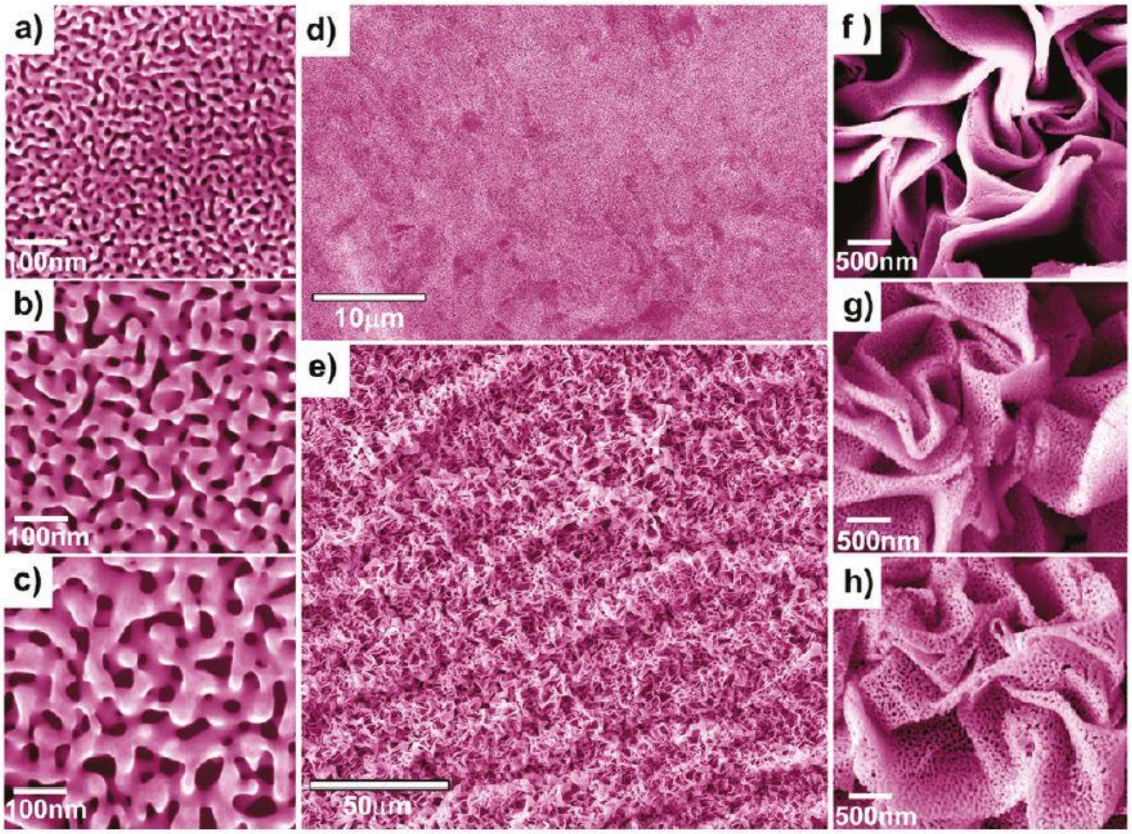

Figure 1.9. False-coloured SEM images of nanoporous gold (NPG) and wrinkled NPG (w-NPG) films. Images of planar NPG films with pore sizes of **(A)** 12, **(B)** 26, and **(C)** 38 nm, respectively. **(D)** A ~38 nm pore size NPG flat film. **(E)** w-NPG films with 38 nm pore sizes. w-NPG films with **(F)** 12, **(G)** 26, and **(H)** 38 nm pore sizes, respectively. Image adapted from Reference 97.

Wrinkled metallic films have also been used as templates to fabricate superhydrophobic antimicrobial surfaces in consumer plastics.[80] Superhydrophobicity is achieved when the contact angle of a water droplet placed on the surface exceeds 150° and the sliding angle is less than 10°. Due to their water resistance, structurally superhydrophobic surfaces prevent bacterial growth without inducing bacterial resistance compared to chemically modified surfaces.[98] Structural superhydrophobic modifications have been performed on polystyrene (PS), polycarbonate (PC), and polyethylene (PE). The antibacterial properties of these surfaces were tested against the gram-negative bacteria *Escherichia coli*. Structured plastics showed a high antibacterial activity when compared to their flat counterparts (Figure 1.10), with the flat plastics presenting significant bacterial growth (white spots) and structured plastics showing minimal to no bacterial growth. Thus, using wrinkled patterns, Freschauf and colleagues were able to produce antibacterial surfaces on consumer plastics without chemical modification.

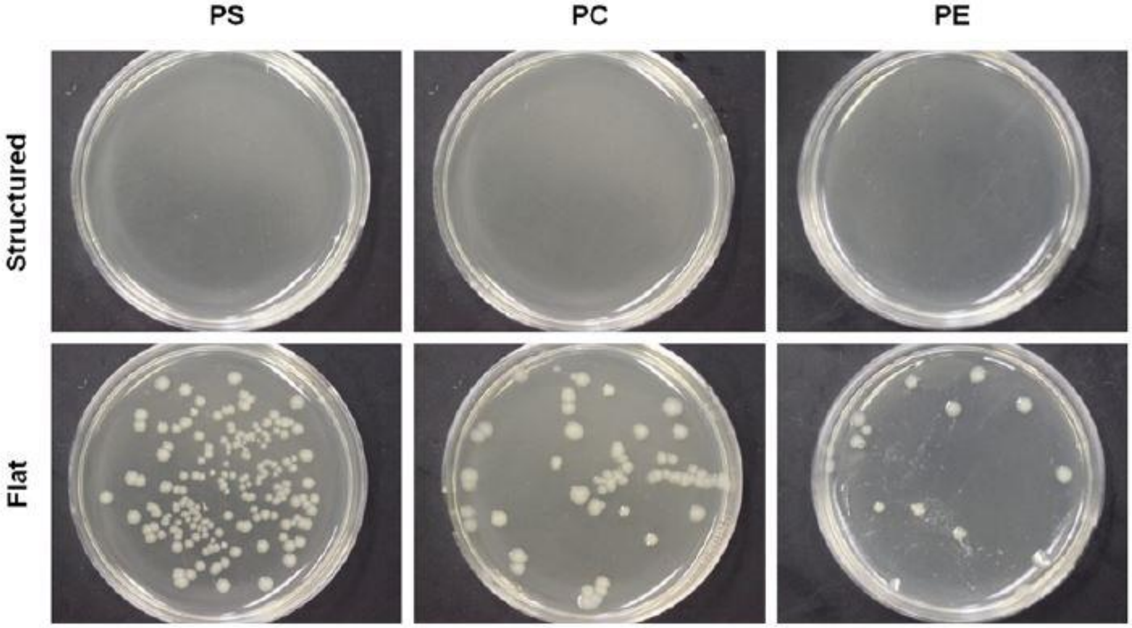

Figure 1.10. Images of E. coli growth on consumer plastics under 24-hour incubation where the structured plastics did not show bacterial growth and flat plastics showed significant bacterial growth seen as cloudy white spots. Adapted from Reference 80.

Some drawbacks of MSEs are linked to their inherent roughness. The roughened topography makes it difficult to accurately model their EASA and to characterize surface bound species, such as supported lipid membranes and immobilized biomolecules, when compared to their flat counterparts. Furthermore, structuring metallic films can result in increased hydrophobicity, a phenomenon that is linked to their nanometer and micrometer sized features.[12,80] In aqueous environments (which are typical of biosensing applications), this could lead to the formation and entrapment of air bubbles in the troughs of each wrinkle, thereby reducing the number of solution accessible regions on the electrode, and ultimately causing a loss in the electrochemical signal.[20] A simple way to eliminate air pockets is to pre-wet the NMSEs with a low surface tension solvent, and then to rinse with water to replace the solvent. However, this might pose an issue for electrodes functionalized with biomolecules, which may denature after exposure to the low surface tension solvent. An alternative solution is to produce super wetting surfaces by coating the structured surfaces with water-soluble polymers, which allow water to penetrate into the crevices and expose the entire electrode surface to the sample. A reported example of this is the use of polyvinyl pyrolidone (PVP) to coat Au NMSEs.[20] Figure 1.11b shows the removal of air pockets from NMSEs following PVP coating. The resulting hydrophilic NMSE showed 2-fold electrochemical signal enhancement for aptamer-based sensing of kanamycin, compared to the bare electrode surface.

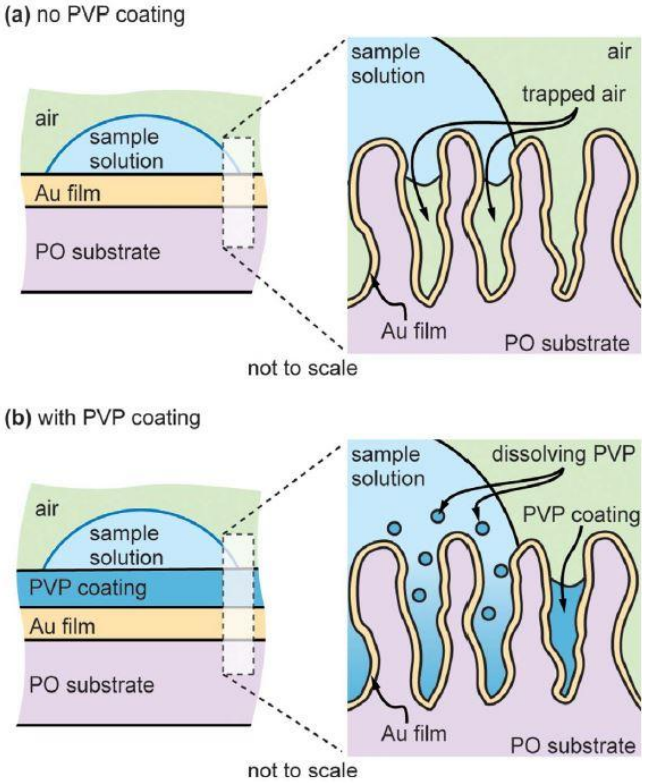

Figure 1.11. Diagram showing **(A)** air bubble formation in aqueous solution on NMSEs and **(B)** the absence of air bubbles post PVP coating. Adapted from reference 20.

The increased knowledge of how stiff materials behave on soft substrates upon the application of a compressive stress, along with understanding of the surface properties of the resulting materials, has enabled researchers to develop NMSEs for an assortment of sensing applications. While NMSEs have been successfully used in stretchable electronics and material templating, the most promising and direct application for NSMEs is in the development of electrochemical biosensing platforms. In ECBs, all of the beneficial attributes provided by the NMSEs, such as electrochemical signal enhancement, size reduction, low-cost, high accessibility, and reproducibility, can be leveraged for the simple and inexpensive production of devices. Nano/microstructured surfaces span across multiple disciplines and cover a broad range of applications from electrochemical biosensing to stretchable electronics and even as templates for polymer structural modification. With their low production cost and ease of fabrication, SMP-induced nano/microstructured metallic thin films offer an excellent platform for the development of novel point-of-care ECBs.

1.4. TYPES OF ELECTROCHEMICAL TECHNIQUES

There are many electrochemical techniques used for biosensing, such as electrochemical impedance spectroscopy (EIS), differential pulse voltammetry (DPV), cyclic voltammetry (CV), chronoamperometry (CA), and chronocoulometry (CC). Some techniques are sophisticated and can be used to study molecular diffusion kinetics and biochemical signal transduction mechanisms, while others are less complex and allow simple electronics to be used and miniaturized for portable biosensing (e.g. the blood glucose sensor). Because these techniques are useful for different applications, their advantages and limitations are discussed in turn below.

1.4.1. Electrochemical Impedance Spectroscopy

Electrochemical impedance spectroscopy (EIS) is a useful technique that can be employed to measure electrical impedance by applying an alternating potential (AC) and measuring the resulting current.[52] To understand how EIS operates and the type of information that can be extracted from EIS experiments, we must first understand the concept of electrical impedance. Like resistance, impedance is a measure of how a circuit resists the flow of electric current. However, impedance is slightly more complex than the Ohms law expression of resistance where the electrical resistance (R) is the ratio of voltage (V) and current (I).

$$R = \frac{V}{I}$$

Impedance is frequency dependent and is represented by a magnitude and a phase shift where a real response is in phase ($0°$) with the excitation wave and an imaginary response is $\pm 90°$

out-of-phase. For example, an inductor element is $+90°$ out-of-phase and a capacitor is $-90°$ out-of-phase. The mathematical representation of this is shown in the equations below.

$$\textbf{Excitation signal: } E_t = E_0 \sin(\omega t)\,;\ \omega = 2\pi f$$

E_t is the potential at time t, E_0 is the amplitude, ω is the radial frequency (radians/second), and f is the frequency (hertz).

$$\textbf{Response signal: } I_t = I_0 \sin(\omega t + \emptyset)$$

I_t is the response signal, I_0 is the amplitude, and $\emptyset$ is the phase shift.

Using Ohms law expressed above for the ideal resistor, the impedance is now be represented as a magnitude, Z_0 and a phase shift, $\emptyset$.

$$Z = \frac{E_t}{I_t} = \frac{E_0 \sin(\omega t)}{I_0 \sin(\omega t + \emptyset)} = Z_0 \frac{\sin(\omega t)}{\sin(\omega t + \emptyset)}$$

Using Euler's relationship in which $\exp(j\emptyset) = cos\emptyset + jsin\emptyset$, where $\emptyset$ is the real and *j* is the imaginary component. We can now represent the above impedance as a complex function.

$$\textbf{Excitation signal: } E_t = E_0 \exp(j\omega t)$$

$$\textbf{Response signal: } I_t = I_0 \exp(j\omega t + \emptyset)$$

$$Z(\omega) = \frac{E}{I} = Z_0 \exp(j\emptyset) = Z_0(cos\emptyset + jsin\emptyset)$$

EIS has many advantages over DC techniques such as the ability to distinguish between two simultaneous electrochemical reactions, identify diffusion limited reactions, and provide information on electron transfer rates. These advantages make EIS a versatile technique used in a wide range of applications such as metal corrosion, label free sensors, batteries, etc… More specifically for electrochemical sensors, EIS is commonly used in early stage device development especially found in antibody based biosensors,[81–83] heavy metal detection,[84] aptasensors,[85–87] and in battery research.[88,89]

Typical EIS experiments are performed by applying a small 1 – 10 mV sinusoidal potential of fixed frequency and measuring the current response. This process is repeated for a wide range of frequency sweeps and the impedance is calculated and plotted in a Nyquist or Bode plot.

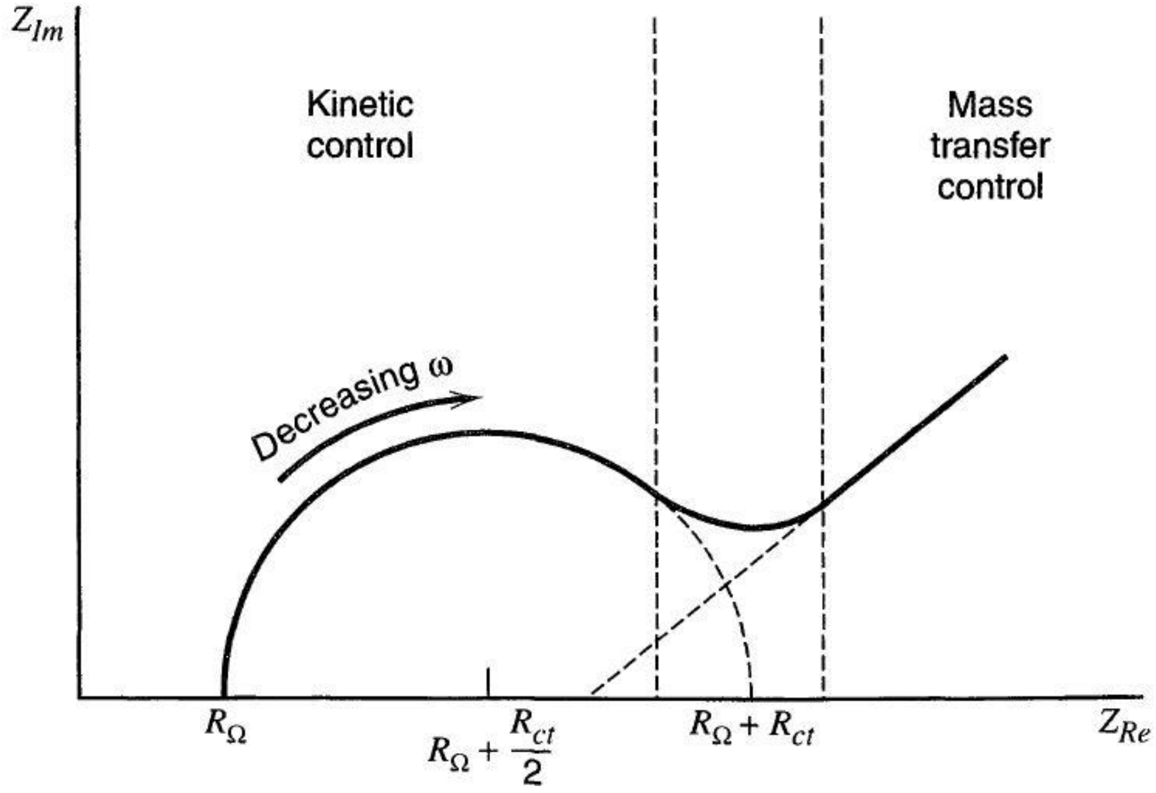

Figure 1.12. An example of a Nyquist plot shows kinetic control regions at high frequencies and mass transfer control regions at low frequencies. Adapted from Reference 52.

Many electroactive compound signals appear at the lower frequency ranges so large frequency sweeps are needed for analysis, which can take many hours to complete and presents a practical challenge when trying to implement into a point-of-care portable device. Additionally, the complexity of components in an electrolytic cell such as the solution resistance and double layer capacitance require data fitting to common circuit models. This presents a challenge in data handling complexity and accuracy, making EIS a difficult electrochemical technique for miniaturized portable biosensors.

1.4.2. Square Wave Voltammetry

Another common type of electrochemical technique is pulsed voltammetry. The primary advantage of pulsed voltammetry is its ability to effectively differentiate Faradaic (reversible redox) currents from capacitive (charging or non-Faradaic) currents. This enables normal pulse voltammetry (NPV), differential pulse voltammetry (DPV), and square wave voltammetry (SWV) to achieve high sensitivity down to the ppb range when used in electrochemical sensing. SWV offer faster experimental run times than NPV and DPV it can operate at high voltage scan rates (1 V/s) where NPV and DPV are limited to 1 – 10 mV/s. This results in experimental times of seconds for SWV over minutes for NPV and DPV. The shape of the potential sweep for SWV is a combination of a square wave and a staircase wave as shown in Figure 1.13. Current is sampled at two points of the oscillating waveform, once at the end of the forward scan (pulse direction is the same as scan direction) and once at the end of the reverse scan. The current signal generated from a redox species is given by:[52]

$$\Delta i_p = \frac{nFAD_0^{1/2}C_0^*}{(\pi t_p)^{1/2}}\Delta\Psi_p$$

where $\Delta \boldsymbol{i_p}$= differential current peak value, **A** = electrode surface area, $\mathbf{C_0}^*$ = concentration of the redox molecule, $\mathbf{D_0}$ = diffusion coefficient of the redox molecule, $\mathbf{t_p}$ = pulse width, and $\Delta \boldsymbol{\Psi_p}$= dimensionless parameter which gauges the peak height relative to the limiting response in normal pulse voltammetry.

By measuring the end pulse currents, the rapidly decaying non-Faradaic current is excluded from the signal current, yielding high signal-to-noise ratio (S:N) measurements.[52,90,91] This feature of SWV makes it an ideal electrochemical technique for rapid, sensitive, and quantitative detection in ECBs, where it typically achieves nanomolar limit of detection for redox active compounds.[92,93] Accordingly, SWV is finding increasing use in electrochemical immunoassays and aptamer-based biosensors.

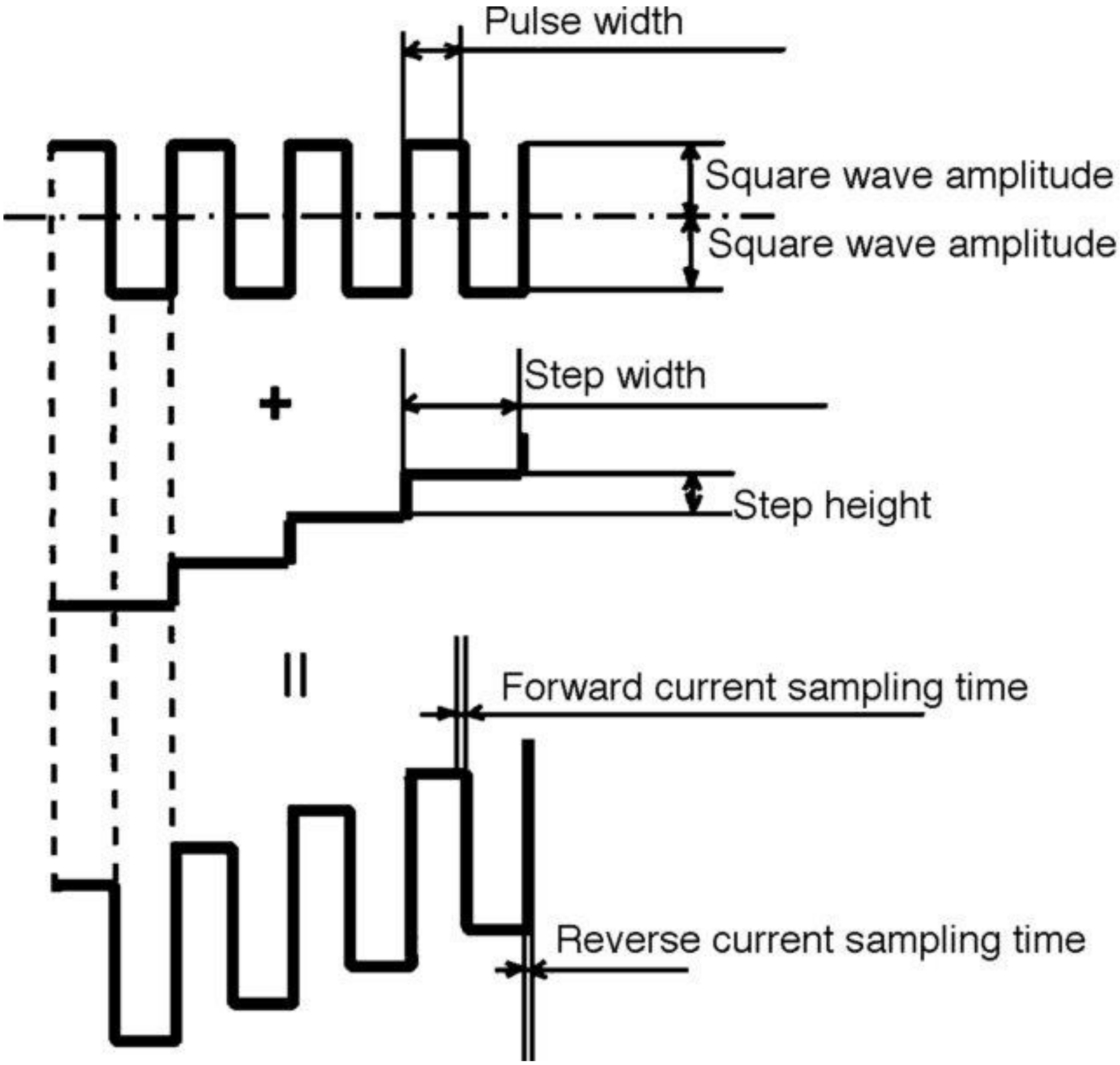

Figure 1.13. The SWV potential waveform combines a square and staircase wave. Adapted from Reference 94.

1.4.3. Cyclic Voltammetry

Cyclic voltammetry (CV) is a voltammetric technique that uses an applied voltage sweep that cycles between two points at a steady scan rate (V/s) while the current is measured. A typical cyclic voltammogram is shown in Figure 1.14.[52]

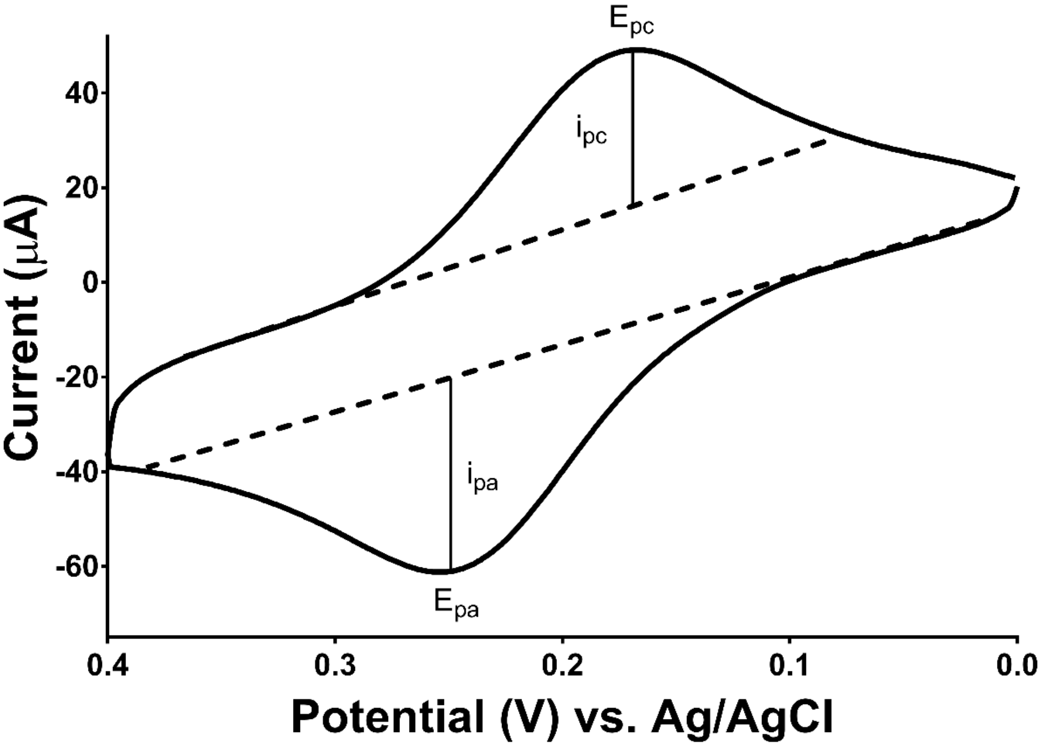

Figure 1.14. A typical cyclic voltammogram of a reversible redox system. E_{pc} = peak cathodic potential, i_{pc} = peak cathodic current, E_{pa} = peak anodic potential, i_{pa} = peak anodic current.

CV is used to study many different properties of the analyte of interest such as diffusion kinetics, electrochemical reversibility, electron transfer kinetics, and chemical intermediate determination.[52] For example, the difference between E_{pa} and E_{pc} can be used to determine the reversibility of the redox species of interest. For a completely reversible system $E_{pa} - E_{pc} = \frac{59\,mV}{n}$ for n electron process. Another indicator of a reversible system is the peak cathodic current and peak anodic current should have the same magnitude. For electrochemical biosensors, the response current is important in quantification of the compound of interest. The response current in a cyclic voltammogram is related to the reactant concentration by the simplified Randles-Sevcik equation. For a system at 25 °C, the response current is expressed as,

$$i_p = 268,600 n^{\frac{3}{2}} A D^{\frac{1}{2}} C v^{\frac{1}{2}}$$

where i_p is the peak current (A), n is the number of electrons transferred in the redox process, A is the electrode area (cm^2), C is the reactant concentration (mol/cm^3), D is the diffusion coefficient of the redox molecule (cm^2/s), and v is scan rate (V/s).[52] This makes CV a powerful electroanalytical technique that is the most common way to: (1) study redox active systems; (2) characterize electrochemical sensors; and (3) benchmark new electrode designs. However, due to the large capacitive current that scales linearly with the scan rate (v), CV experiments are limited to slower scan rates to ensure the background capacitive current does not supersede the Faradaic redox current, and the current must be integrated over the cathodic or anodic peak to accurately quantify the concentration of the redox molecule. Hence, CV is challenging to miniaturize onto handheld medical devices, since it requires data processing to derive reliable quantitative data. Thus, simpler electroanalytical techniques are required and frequently used for such downstream implementation.

1.4.4. Chronoamperometry

Chronoamperometry (CA) is an electroanalytical technique where a potential is stepped from a baseline V_1 to a secondary potential V_2. The response current from this potential step is measured over time and related to the reactant concentration by the Cottrell equation:

$$|i| = \frac{nFAC^0\sqrt{D}}{\sqrt{\pi}\sqrt{t}}$$

where i denotes the current (A), n is the number of electrons exchanged in the redox reaction, F is Faraday's constant (96485 C/mol), A is the electrode area (cm^2), C^0 is the reactant concentration (mol/cm^3), D is the diffusion coefficient (cm^2/s), and t is time (seconds).[52] One major consideration when sampling current for quantification of an electrochemical reaction is the influence of the capacitive current (i_c) caused by the initial potential step. The i_c is only significant in the first few miliseconds of the potential step and is a function of $\frac{1}{t}$. One solution to double layer capacitance, is to perform the experiment in the background electrolyte and subtract the subsequent current from the signal obtained during real experiments. Alternatively, only considering the last 90% step time of the $i - t$ data is a faster and internal technique to remove the double layer capacitance signal.

CA is a rapid and simple electroanalytical technique that has miniaturization potential. It is commonly found in applications such as biosensors, heavy metal detection, glucose sensors, and electrode surface area determination, but it has also been used to electrochemically generate nanostructures on metallic surfaces in an effort to increase the EASA. While advantageous, CA can be limited to situations where the sample matrix is well controlled. This is because the reduction or oxidation of compounds in the matrix by the excess potential applied away from the E^0 will contribute to the total current measured. Therefore, most electroanalytical devices use more sophisticated electrochemical techniques such as EIS and CV to better understand the system under investigation, prior to using CA as the final rapid sensing technique.

1.5. CONCLUSION

Nano/microstructured electrodes (NMSEs) have gained popularity in the past two decades for use as highly sensitive transducers for electrochemical biosensors (ECBs). Here, we define NMSEs and discussed their variants, fabrication methods, and some of their applications. Controllable wrinkle structures are interesting for their potential applications in nanotechnology, cell biology, medical devices, solar cells, and biosensing. One promising method for producing NMSEs was developed in the late 1990's through heat induced expansion of soft silicone elastomers that upon cooling were used to create wrinkled metallic thin films. Since then researchers have used shape-memory polymers (SMPs) with thermo-responsive properties as a low-cost and rapid bench-top approach to producing highly controllable, uniaxially and biaxially wrinkled metallic thin films. The maturation of wrinkling techniques has enabled researchers to develop high surface area electrodes for extremely sensitive and portable ECBs. For biosensing applications, electrochemical techniques offer high sensitivity, rapid detection, low-cost, operational simplicity, and commercial scalability, as demonstrated by the success of blood glucose sensors. Low-cost benchtop fabrication techniques provide a new level of accessibility to the production of wrinkled thin films. The applications of wrinkled films were highlighted in electrochemical biosensors, microfluidic chips, and flexible electronics. The miniaturization of wrinkled electrodes could enable researchers to accelerate the development of portable sensing technologies and bring bedside medical diagnostic tools to the market.

REFERENCES

(1) World Health Organization. *DALY Estimates, 2000-2016*; 2018.

(2) Dorothee, G.; Robert, M.; Janos, V.; Erik, R. Electrochemical Biosensors - Sensor Principles and Architectures. *Sensors* **2008**, *8* (January), 1400–1458. https://doi.org/10.3390/s80314000.

(3) Cho, I. H.; Lee, J.; Kim, J.; Kang, M. S.; Paik, J. K.; Ku, S.; Cho, H. M.; Irudayaraj, J.; Kim, D. H. Current Technologies of Electrochemical Immunosensors: Perspective on Signal Amplification. *Sensors (Switzerland)* **2018**, *18* (1), 1–18. https://doi.org/10.3390/s18010207.

(4) Lowe, C. R. Biosensors. **1984**, No. 3, 59–65.

(5) Putzbach, W.; Ronkainen, N. J. Immobilization Techniques in the Fabrication of Nanomaterial-Based Electrochemical Biosensors: A Review. *Sensors (Switzerland)* **2013**, *13* (4), 4811–4840. https://doi.org/10.3390/s130404811.

(6) Pancrazio, J. J.; Whelan, J. P.; Borkholder, D. A.; Ma, W.; Stenger, D. A. Development and Application of Cell-Based Biosensors. *Ann. Biomed. Eng.* **1999**, *27* (6), 697–711. https://doi.org/10.1114/1.225.

(7) Drummond, T. G.; Hill, M. G.; Barton, J. K. Electrochemical DNA Sensors. *Nat. Biotechnol.* **2003**, *21* (10), 1192–1199. https://doi.org/10.1038/nbt873.

(8) Clark, L. C.; Lyons, C. Electrode Systems for Continuous Monitoring in Cardiovascular Surgery. *Ann. N. Y. Acad. Sci.* **1962**, *102* (1), 29–45. https://doi.org/10.1111/j.1749-6632.1962.tb13623.x.

(9) Bahadir, E. B.; Sezgintürk, M. K. Applications of Commercial Biosensors in Clinical, Food, Environmental, and Biothreat/Biowarfare Analyses. *Anal. Biochem.* **2015**, *478*, 107–120. https://doi.org/10.1016/j.ab.2015.03.011.

(10) Kwakye, S.; Goral, V. N.; Baeumner, A. J. Electrochemical Microfluidic Biosensor for Nucleic Acid Detection with Integrated Minipotentiostat. *Biosens. Bioelectron.* **2006**, *21* (12), 2217–2223. https://doi.org/10.1016/j.bios.2005.11.017.

(11) Bunyakul, N.; Baeumner, A. Combining Electrochemical Sensors with Miniaturized Sample Preparation for Rapid Detection in Clinical Samples. *Sensors* **2014**, *15* (1), 547–564. https://doi.org/10.3390/s150100547.

(12) Fu, C. C.; Grimes, A.; Long, M.; Ferri, C. G. L.; Rich, B. D.; Ghosh, S.; Ghosh, S.; Lee, L. P.; Gopinathan, A.; Khine, M. Tunable Nanowrinkles on Shape Memory Polymer Sheets. *Adv. Mater.* **2009**, *21* (44), 4472–4476. https://doi.org/10.1002/adma.200902294.

(13) Arroyo-Currás, N.; Scida, K.; Ploense, K. L.; Kippin, T. E.; Plaxco, K. W. High Surface Area Electrodes Generated via Electrochemical Roughening Improve the Signaling of Electrochemical Aptamer-Based Biosensors. *Anal. Chem.* **2017**, *89* (22), 12185–12191.

https://doi.org/10.1021/acs.analchem.7b02830.

(14) Gabardo, C. M.; Yang, J.; Smith, N. J.; Adams-McGavin, R. C.; Soleymani, L. Programmable Wrinkling of Self-Assembled Nanoparticle Films on Shape Memory Polymers. *ACS Nano* **2016**, *10* (9), 8829–8836. https://doi.org/10.1021/acsnano.6b04584.

(15) Soleymani, L.; Fang, Z.; Sargent, E. H.; Kelley, S. O. Programming the Detection Limits of Biosensors through Controlled Nanostructuring. *Nat. Nanotechnol.* **2009**, *4* (12), 844–848. https://doi.org/10.1038/nnano.2009.276.

(16) Zhang, R.; Olin, H. Porous Gold Films-a Short Review on Recent Progress. *Materials (Basel).* **2014**, *7* (5), 3834–3854. https://doi.org/10.3390/ma7053834.

(17) Orozco, J.; Fernández-Sánchez, C.; Jiménez-Jorquera, C. Underpotential Deposition - Anodic Stripping Voltammetric Detection of Copper at Gold Nanoparticle-Modified Ultramicroelectrode Arrays. *Environ. Sci. Technol.* **2008**, *42* (13), 4877–4882. https://doi.org/10.1021/es8005964.

(18) Gabardo, C. M.; Zhu, Y.; Soleymani, L.; Moran-Mirabal, J. M. Bench-Top Fabrication of Hierarchically Structured High-Surface-Area Electrodes. *Adv. Funct. Mater.* **2013**, *23* (24), 3030–3039. https://doi.org/10.1002/adfm.201203220.

(19) Saem, S.; Zhu, Y.; Luu, H.; Moran-Mirabal, J. Bench-Top Fabrication of an All-PDMS Microfluidic Electrochemical Cell Sensor Integrating Micro/Nanostructured Electrodes. *Sensors (Switzerland)* **2017**, *17* (4). https://doi.org/10.3390/s17040732.

(20) Hauke, A.; Kumar, L. S. S.; Kim, M. Y.; Pegan, J.; Khine, M.; Li, H.; Plaxco, K. W.; Heikenfeld, J. Superwetting and Aptamer Functionalized Shrink-Induced High Surface Area Electrochemical Sensors. *Biosens. Bioelectron.* **2017**, *94* (March), 438–442. https://doi.org/10.1016/j.bios.2017.03.024.

(21) Zhang, L.; Lang, X.; Hirata, A.; Chen, M. Wrinkled Nanoporous Gold Films with Ultrahigh Surface-Enhanced Raman Scattering Enhancement. *ACS Nano* **2011**, *5* (6), 4407–4413. https://doi.org/10.1021/nn201443p.

(22) Patel, J.; Radhakrishnan, L.; Zhao, B.; Uppalapati, B.; Daniels, R. C.; Ward, K. R.; Collinson, M. M. Electrochemical Properties of Nanostructured Porous Gold Electrodes in Biofouling Solutions. *Anal. Chem.* **2013**, *85* (23), 11610–11618. https://doi.org/10.1021/ac403013r.

(23) Orozco, J.; Jiménez-Jorquera, C.; Fernández-Sánchez, C. Gold Nanoparticle-Modified Ultramicroelectrode Arrays for Biosensing: A Comparative Assessment. *Bioelectrochemistry* **2009**, *75* (2), 176–181. https://doi.org/10.1016/j.bioelechem.2009.03.013.

(24) Orozco, J.; Fernández-Sánchez, C.; Jiménez-Jorquera, C. Ultramicroelectrode Array Based Sensors: A Promising Analytical Tool for Environmental Monitoring. *Sensors* **2010**, *10* (1), 475–490. https://doi.org/10.3390/s100100475.

(25) Ross, B.; Cammann, K.; Mokwa, W.; Rospert, M. Ultramicroelectrode Arrays as Transducers for New Amperometric Oxygen Sensors. *Sensors Actuators B. Chem.* **1992**, *7* (1–3), 758–762. https://doi.org/10.1016/0925-4005(92)80399-I.

(26) Feeney, R.; Kounaves, S. P. Microfabricated Ultramicroelectrode Arrays: Developments, Advances, and Applications in Environmental Analysis. *Electroanalysis* **2000**, *12* (9), 677–684. https://doi.org/10.1002/1521-4109(200005)12:9<677::AID-ELAN677>3.0.CO;2-4.

(27) Min, J.; Baeumner, A. J. Characterization and Optimization of Interdigitated Ultramicroelectrode Arrays as Electrochemical Biosensor Transducers. *Electroanalysis* **2004**, *16* (9), 724–729. https://doi.org/10.1002/elan.200302872.

(28) Pacios, M.; Valle, M. Del; Bertran, E.; Bartrolí, J.; Esplandiu, M. J. Ultramicroelectrode Arrays (UMAS) Based on Carbon Nanotube as Amperometric (Bio) Sensor Transducers. 18–22.

(29) Ross, B. Biosensor on the Base of Polypyrrole Modified. *Micro* **1994**, *41* (6).

(30) Woo, S. M.; Gabardo, C. M.; Soleymani, L. Prototyping of Wrinkled Nano-/Microstructured Electrodes for Electrochemical DNA Detection. *Anal. Chem.* **2014**, *86* (24), 12341–12347. https://doi.org/10.1021/ac5036296.

(31) Ding, Y.; Kim, Y. J.; Erlebacher, J. Nanoporous Gold Leaf: "Ancient Technology "/Advanced Material. *Adv. Mater.* **2004**, *16* (21), 1897–1900. https://doi.org/10.1002/adma.200400792.

(32) Orozco, J.; Fernández-Sánchez, C.; Jiménez-Jorquera, C. Ultramicroelectrode Array Based Sensors: A Promising Analytical Tool for Environmental Monitoring. *Sensors* **2010**, *10* (1), 475–490. https://doi.org/10.3390/s100100475.

(33) Zoski, C. G. Ultramicroelectrodes : Design , Fabrication , and Characterization. **2002**, 1041–1051.

(34) Perre, E.; Nyholm, L.; Gustafsson, T.; Taberna, P. L.; Simon, P.; Edström, K. Direct Electrodeposition of Aluminium Nano-Rods. *Electrochem. commun.* **2008**, *10* (10), 1467–1470. https://doi.org/10.1016/j.elecom.2008.07.032.

(35) Shaijumon, M. M.; Perre, E.; Daffos, B.; Taberna, P. L.; Tarascon, J. M.; Simon, P. Nanoarchitectured 3D Cathodes for Li-Ion Microbatteries. *Adv. Mater.* **2010**, *22* (44), 4978–4981. https://doi.org/10.1002/adma.201001922.

(36) Mosca, M. Spontaneous Formation of Ordered Structures in Thin. *Nature* **1998**, *393* (May), 0–3. https://doi.org/10.1038/30193.

(37) Sonney, S.; Shek, N.; Moran-Mirabal, J. M. Rapid Bench-Top Fabrication of Poly(Dimethylsiloxane)/Polystyrene Microfluidic Devices Incorporating High-Surface-Area Sensing Electrodes. *Biomicrofluidics* **2015**, *9* (2). https://doi.org/10.1063/1.4918596.

(38) Sage, A. T.; Besant, J. D.; Lam, B.; Sargent, E. H.; Kelley, S. O. Ultrasensitive

Electrochemical Biomolecular Detection Using Nanostructured Microelectrodes. *Acc. Chem. Res.* **2014**, *47* (8), 2417–2425. https://doi.org/10.1021/ar500130m.

(39) Das, J.; Kelley, S. O. Protein Detection Using Arrayed Microsensor Chips: Tuning Sensor Footprint to Achieve Ultrasensitive Readout of CA-125 in Serum and Whole Blood. *Anal. Chem.* **2011**, *83* (4), 1167–1172. https://doi.org/10.1021/ac102917f.

(40) Shulga, O. V.; Jefferson, K.; Khan, A. R.; D'Souza, V. T.; Liu, J.; Demchenko, A. V.; Stine, K. J. Preparation and Characterization of Porous Gold and Its Application as a Platform for Immobilization of Acetylcholine Esterase. *Chem. Mater.* **2007**, *19* (16), 3902–3911. https://doi.org/10.1021/cm070238n.

(41) Seker, E.; Reed, M. L.; Begley, M. R. Nanoporous Gold: Fabrication, Characterization, and Applications. *Materials (Basel).* **2009**, *2* (4), 2188–2215. https://doi.org/10.3390/ma2042188.

(42) Jiang, J.; Wang, X. Fabrication of High-Surface Nanoporous Gold Microelectrode. *Electrochem. commun.* **2012**, *20* (1), 157–159. https://doi.org/10.1016/j.elecom.2012.04.028.

(43) Jia, F.; Yu, C.; Ai, Z.; Zhang, L. Fabrication of Nanoporous Gold Film Electrodes with Ultrahigh Surface Area and Electrochemical Activity. *Chem. Mater.* **2007**, *19* (15), 3648–3653. https://doi.org/10.1021/cm070425l.

(44) Dixon, M. C.; Daniel, T. A.; Hieda, M.; Smilgies, D. M.; Chan, M. H. W.; Allara, D. L. Preparation, Structure, and Optical Properties of Nanoporous Gold Thin Films. *Langmuir* **2007**, *23* (5), 2414–2422. https://doi.org/10.1021/la062313z.

(45) Betz, G. Alloy Sputtering. *Surf. Sci.* **1980**, *92* (1), 283–309. https://doi.org/10.1016/0039-6028(80)90258-7.

(46) Iwasita, T. Electrocatalysis of Methanol Oxidation. *Electrochim. Acta* **2002**, *47* (22–23), 3663–3674. https://doi.org/10.1016/S0013-4686(02)00336-5.

(47) Perez, J.; Gonzalez, E. R.; Ticianelli, E. A. Oxygen Electrocatalysis on Thin Porous Coating Rotating Platinum Electrodes. *Electrochim. Acta* **1998**, *44* (8–9), 1329–1339. https://doi.org/10.1016/S0013-4686(98)00255-2.

(48) Su, W.; Cho, M. S.; Nam, J. Do; Choe, W. S.; Lee, Y. Highly Sensitive Electrochemical Lead Ion Sensor Harnessing Peptide Probe Molecules on Porous Gold Electrodes. *Biosens. Bioelectron.* **2013**, *48*, 263–269. https://doi.org/10.1016/j.bios.2013.04.031.

(49) Lin, Y.; Peng, Y.; Di, J. Electrochemical Detection of Hg(II) Ions Based on Nanoporous Gold Nanoparticles Modified Indium Tin Oxide Electrode. *Sensors Actuators, B Chem.* **2015**, *220*, 1086–1090. https://doi.org/10.1016/j.snb.2015.06.064.

(50) Patel, J.; Radhakrishnan, L.; Zhao, B.; Uppalapati, B.; Daniels, R. C.; Ward, K. R.; Collinson, M. M. Electrochemical Properties of Nanostructured Porous Gold Electrodes in Biofouling Solutions. *Anal. Chem.* **2013**, *85* (23), 11610–11618. https://doi.org/10.1021/ac403013r.

(51) Tschuncky, P.; Heinze, J. A Method for the Construction of Ultramicroelectrodes. *Anal. Chem.* **1995**, *67* (21), 4020–4023. https://doi.org/10.1021/ac00117a032.

(52) Bard, A. J.; Faulkner, L. R. *Electrochemical Methods: Fundamentals and Applications*, 2nd ed.; Harris, D., Swain, E., Eds.; 1980.

(53) Szamocki, R.; Velichko, A.; Holzapfel, C.; Mücklich, F.; Ravaine, S.; Garrigue, P.; Sojic, N.; Hempelmann, R.; Kuhn, A. Macroporous Ultramicroelectrodes for Improved Electroanalytical Measurements. *Anal. Chem.* **2007**, *79* (2), 533–539. https://doi.org/10.1021/ac0615854.

(54) Xia, Y.; Whitesides, G. M. Soft Lithography. *Annu. Rev. Mater. Sci.* **1998**, *28* (1), 153–184. https://doi.org/10.1146/annurev.matsci.28.1.153.

(55) Zhao, X. M. Soft Lithographic Methods for Nano-Fabrication. *J. Mater. Chem.* **1997**, *7* (7), 1069–1074. https://doi.org/10.1039/a700145b.

(56) Chung, S.; Lee, J. H.; Moon, M.-W.; Han, J.; Kamm, R. D. Non-Lithographic Wrinkle Nanochannels for Protein Preconcentration. *Adv. Mater.* **2008**, *20* (16), 3011–3016. https://doi.org/10.1002/adma.200701715.

(57) Pegan, J. D.; Ho, A. Y.; Bachman, M.; Khine, M. Flexible Shrink-Induced High Surface Area Electrodes for Electrochemiluminescent Sensing. *Lab Chip* **2013**, *13* (21), 4205–4209. https://doi.org/10.1039/c3lc50588j.

(58) Grimes, A.; Breslauer, D. N.; Long, M.; Pegan, J.; Lee, L. P.; Khine, M. Shrinky-Dink Microfluidics: Rapid Generation of Deep and Rounded Patterns. *Lab Chip* **2007**, *8* (1), 170–172. https://doi.org/10.1039/b711622e.

(59) Kuemin, C.; Nowack, L.; Bozano, L.; Spencer, N. D.; Wolf, H. Oriented Assembly of Gold Nanorods on the Single-Particle Level. *Adv. Funct. Mater.* **2012**, *22* (4), 702–708. https://doi.org/10.1002/adfm.201101760.

(60) Kong, J.; Chapline, M. G.; Dai, H. Capillary Force Lithography. *Adv. Mater.* **2001**, *13* (18), 1386–1389. https://doi.org/10.1002/1521-4095(200109)13:18<1386::AID-ADMA1386>3.0.CO;2-X.

(61) Kraus, T.; Malaquin, L.; Schmid, H.; Riess, W.; Spencer, N. D.; Wolf, H. Nanoparticle Printing with Single-Particle Resolution. *Nat. Nanotechnol.* **2007**, *2* (9), 570–576. https://doi.org/10.1038/nnano.2007.262.

(62) Bowden, N.; Brittain, S.; Evans, A. G.; Hutchinson, J. W.; Whitesides, G. M. Spontaneous Formation of Ordered Structures in Thin Films of Metals Supported on an Elastomeric Polymer. *Nature* **1998**, *393* (May), 146–149. https://doi.org/10.1038/30193.

(63) Genzer, J.; Groenewold, J. Soft Matter with Hard Skin: From Skin Wrinkles to Templating and Material Characterization. *Soft Matter* **2006**, *2* (4), 310–323. https://doi.org/10.1039/b516741h.

(64) Hollenberg, B. A.; Richards, C. D.; Richards, R.; Bahr, D. F.; Rector, D. M. A MEMS Fabricated Flexible Electrode Array for Recording Surface Field Potentials. *J. Neurosci. Methods* **2006**, *153* (1), 147–153. https://doi.org/10.1016/j.jneumeth.2005.10.016.

(65) Kjeang, E.; Djilali, N.; Sinton, D. Microfluidic Fuel Cells: A Review. *J. Power Sources* **2009**, *186* (2), 353–369. https://doi.org/10.1016/j.jpowsour.2008.10.011.

(66) Vetter, R. J.; Williams, J. C.; Kipke, D. R.; Rousche, P. J.; Pellinen, D. S.; Pivin, D. P. Flexible Polyimide-Based Intracortical Electrode Arrays with Bioactive Capability. *IEEE Trans. Biomed. Eng.* **2001**, *48* (3), 361–371. https://doi.org/10.1109/10.914800.

(67) Mijatovic, D.; Eijkel, J. C. T.; Van Den Berg, A. Technologies for Nanofluidic Systems: Top-down vs. Bottom-up - A Review. *Lab Chip* **2005**, *5* (5), 492–500. https://doi.org/10.1039/b416951d.

(68) Seisyan, R. P. Nanolithography in Microelectronics: A Review. *Tech. Phys.* **2011**, *56* (8), 1061–1073. https://doi.org/10.1134/s1063784211080214.

(69) Winky, L. W. H.; Dieter, W. T.; Nikolaus, J. S.; Man, W.; Yitshak, Z. Surface-Chemistry Technology for Microfluidics. *J. Micromechanics Microengineering* **2003**, *13* (2), 272.

(70) Yue, W.; Wang, Z.; Yang, Y.; Chen, L.; Syed, A.; Wong, K.; Wang, X. Electron-Beam Lithography of Gold Nanostructures for Surface-Enhanced Raman Scattering. *J. Micromechanics Microengineering* **2012**, *22* (12). https://doi.org/10.1088/0960-1317/22/12/125007.

(71) Green, T. A. Gold Electrodeposition for Microelectronic, Optoelectronic and Microsystem Applications. *Gold Bull.* **2007**, *40* (2), 105–114. https://doi.org/10.1007/BF03215566.

(72) Christie, I. R.; Cameron, B. P. Gold Electrodeposition within the Electronics Industry. *Gold Bull.* **1994**, *27* (1), 12–20. https://doi.org/10.1007/BF03214728.

(73) Chen, C. M.; Yang, S. Wrinkling Instabilities in Polymer Films and Their Applications. *Polym. Int.* **2012**, *61* (7), 1041–1047. https://doi.org/10.1002/pi.4223.

(74) Yu, C.; Jiang, H. Forming Wrinkled Stiff Films on Polymeric Substrates at Room Temperature for Stretchable Interconnects Applications. *Thin Solid Films* **2010**, *519* (2), 818–822. https://doi.org/10.1016/j.tsf.2010.08.106.

(75) Chung, J. Y.; Nolte, A. J.; Stafford, C. M. Surface Wrinkling: A Versatile Platform for Measuring Thin-Film Properties. *Adv. Mater.* **2011**, *23* (3), 349–368. https://doi.org/10.1002/adma.201001759.

(76) Groenewold, J. Wrinkling of Plates Coupled with Soft Elastic Media. *Phys. A Stat. Mech. its Appl.* **2001**, *298* (1–2), 32–45. https://doi.org/10.1016/S0378-4371(01)00209-6.

(77) Zhao, J. H.; Kiene, M.; Hu, C.; Ho, P. S. Thermal Stress and Glass Transition of Ultrathin Polystyrene Films. *Appl. Phys. Lett.* **2000**, *77* (18), 2843–2845. https://doi.org/10.1063/1.1322049.

(78) Wu, B.; Heidelberg, A.; Boland, J. J. Mechanical Properties of Ultrahigh-Strength Gold Nanowires. *Nat. Mater.* **2005**, *4* (7), 525–529. https://doi.org/10.1038/nmat1403.

(79) Saem, S.; Abbaszadeh Amirdehi, M.; Greener, J.; Zarabadi, M. P.; Moran-Mirabal, J. M. Microstructured Anodes by Surface Wrinkling for Studies of Direct Electron Transfer Biofilms in Microbial Fuel Cells. *Adv. Mater. Interfaces* **2018**, *5* (13), 1800290. https://doi.org/10.1002/admi.201800290.

(80) Soleymani, L.; Fang, Z.; Lam, B.; Bin, X.; Vasilyeva, E.; Ross, A. J.; Sargent, E. H.; Kelley, S. O. Hierarchical Nanotextured Microelectrodes Overcome the Molecular Transport Barrier to Achieve Rapid, Direct Bacterial Detection. *ACS Nano* **2011**, *5* (4), 3360–3366. https://doi.org/10.1021/nn200586s.

(81) Zhu, Y.; Moran-Mirabal, J. Highly Bendable and Stretchable Electrodes Based on Micro/Nanostructured Gold Films for Flexible Sensors and Electronics. *Adv. Electron. Mater.* **2016**, *2*, 1500345. https://doi.org/10.1002/aelm.201500345.

(82) Zhang, L.; Lang, X.; Hirata, A.; Chen, M. Wrinkled Nanoporous Gold Films with Ultrahigh Surface-Enhanced Raman Scattering Enhancement. *ACS Nano* **2011**, *5* (6), 4407–4413. https://doi.org/10.1021/nn201443p.

(83) Freschauf, L. R.; McLane, J.; Sharma, H.; Khine, M. Shrink-Induced Superhydrophobic and Antibacterial Surfaces in Consumer Plastics. *PLoS One* **2012**, *7* (8), 1–7. https://doi.org/10.1371/journal.pone.0040987.

(84) Andersson, D. I.; Hughes, D. Antibiotic Resistance and Its Cost: Is It Possible to Reverse Resistance? *Nat. Rev. Microbiol.* **2010**, *8* (4), 260–271. https://doi.org/10.1038/nrmicro2319.

(85) Tsekenis, G.; Garifallou, G. Z.; Davis, F.; Millner, P. A.; Gibson, T. D.; Higson, S. P. J. Label-Less Immunosensor Assay for Myelin Basic Protein Based upon an Ac Impedance Protocol. *Anal. Chem.* **2008**, *80* (6), 2058–2062. https://doi.org/10.1021/ac702070e.

(86) Wan, J.; Ai, J.; Zhang, Y.; Geng, X.; Gao, Q.; Cheng, Z. Signal-off Impedimetric Immunosensor for the Detection of Escherichia Coli O157:H7. *Sci. Rep.* **2016**, *6*, 2–7. https://doi.org/10.1038/srep19806.

(87) Hong, B.; Sun, A.; Pang, L.; Venkatesh, A. G.; Hall, D.; Fainman, Y. Integration of Faradaic Electrochemical Impedance Spectroscopy into a Scalable Surface Plasmon Biosensor for in Tandem Detection. *Opt. Express* **2015**, *23* (23), 30237. https://doi.org/10.1364/OE.23.030237.

(88) Kazemi, S. H.; Shanehsaz, M.; Ghaemmaghami, M. Non-Faradaic Electrochemical Impedance Spectroscopy as a Reliable and Facile Method: Determination of the Potassium Ion Concentration Using a Guanine Rich Aptasensor. *Mater. Sci. Eng. C* **2015**, *52*, 151–154. https://doi.org/10.1016/j.msec.2015.03.058.

(89) Sassolas, A.; Blum, L. J.; Béatrice, D. L. B. Electrochemical Aptasensors. *Electroanalysis*

2009, *21* (11), 1237–1250. https://doi.org/10.1002/elan.200804554.

(90) Wang, L.; Zhu, C.; Han, L.; Jin, L.; Zhou, M.; Dong, S. Label-Free, Regenerative and Sensitive Surface Plasmon Resonance and Electrochemical Aptasensors Based on Graphene. *Chem. Commun.* **2011**, *47* (27), 7794–7796. https://doi.org/10.1039/c1cc11373a.

(91) Wang, Y.; Feng, J.; Tan, Z.; Wang, H. Electrochemical Impedance Spectroscopy Aptasensor for Ultrasensitive Detection of Adenosine with Dual Backfillers. *Biosens. Bioelectron.* **2014**, *60*, 218–223. https://doi.org/10.1016/j.bios.2014.04.022.

(92) Zhang, S. S.; Xu, K.; Jow, T. R. EIS Study on the Formation of Solid Electrolyte Interface in Li-Ion Battery. *Electrochim. Acta* **2006**, *51* (8–9), 1636–1640. https://doi.org/10.1016/j.electacta.2005.02.137.

(93) Bouchet, R.; Lascaud, S.; Rosso, M. An EIS Study of the Anode Li/PEO-LiTFSI of a Li Polymer Battery. *J. Electrochem. Soc.* **2003**, *150* (10), A1385. https://doi.org/10.1149/1.1609997.

(94) Osteryoung, J., O´Dea, J. . Square Wave Voltammetry. *Electroanal. Chem. Bard, A.J* **1987**, *57* (1), 1100. https://doi.org/10.1021/ac00279a004.

(95) Ramaley, L.; Krause, M. S. Theory of Square Wave Voltammetry. *Anal. Chem.* **1969**, *41* (11), 1362–1365. https://doi.org/10.1021/ac60280a005.

(96) Liu, Y.; Tuleouva, N.; Ramanculov, E.; Revzin, A. Aptamer-Based Electrochemical Biosensor for Interferon Gamma Detection. **2010**, *82* (19), 8131–8136.

(97) Viswanathan, S.; Radecka, H.; Radecki, J. Biosensors and Bioelectronics Electrochemical Biosensor for Pesticides Based on Acetylcholinesterase Immobilized on Polyaniline Deposited on Vertically Assembled Carbon Nanotubes Wrapped with SsDNA. **2009**, *24*, 2772–2777. https://doi.org/10.1016/j.bios.2009.01.044.

(98) Xu, K.; Dexter, S. C.; Luther, G. W. Voltammetric Microelectrodes for Biocorrosion Studies. *Corrosion* **1998**, *54* (10), 814–823. https://doi.org/10.5006/1.3284801.

Chapter 2: Bench-Top Fabrication of an All-PDMS Microfluidic Electrochemical Cell Sensor Integrating Micro/Nanostructured Electrodes

This chapter was originally published as:

Sokunthearath Saem, Yujie Zhu, Helen Luu and Jose Moran-Mirabal.* (2017) Bench-top fabrication of an all-PDMS microfluidic electrochemical biosensor integrating micro/nanostructured electrodes. *Sensors*. **17**: 732.

and has been reprinted with permission from MDPI – Sensors.

Author Contributions: SS and JMM planned the study, analyzed the data and wrote the manuscript, SS fabricated all sensing device components, characterized electrode with fluorescence microscopy, SEM, and electrochemistry. YZ provided technical expertise in the electrode lift-off method. HL cultured 3T3 fibroblasts.

Article

Bench-Top Fabrication of an All-PDMS Microfluidic Electrochemical Cell Sensor Integrating Micro/Nanostructured Electrodes

Sokunthearath Saem, Yujie Zhu, Helen Luu and Jose Moran-Mirabal *

Department of Chemistry and Chemical Biology, McMaster University, 1280 Main Street West, Hamilton, ON L8S 4M1, Canada; saems@mcmaster.ca (S.S.); zhuy8@mcmaster.ca (Y.Z.); luuh2@mcmaster.ca (H.L.)

* Correspondence: mirabj@mcmaster.ca; Tel.: +1-905-525-9140

Academic Editors: Amine Miled and Jesse Greener

Received: 11 January 2017; Accepted: 27 March 2017; Published: date

ABSTRACT

In recent years, efforts in the development of lab-on-a-chip (LoC) devices for point-of-care (PoC) applications have increased to bring affordable, portable, and sensitive diagnostics to the patients' bedside. To reach this goal, research has shifted from using traditional microfabrication methods to more versatile, rapid, and low-cost options. This work focuses on the benchtop fabrication of a highly sensitive, fully transparent, and flexible poly (dimethylsiloxane) (PDMS) microfluidic (µF) electrochemical cell sensor. The µF device encapsulates 3D structured gold and platinum electrodes, fabricated using a shape-memory polymer shrinking method, which are used to set up an on-chip electrochemical cell. The PDMS to PDMS-structured electrode bonding protocol to fabricate the µF chip was optimized and found to have sufficient bond strength to withstand up to 100 mL/min flow rates. The sensing capabilities of the on-chip electrochemical cell were demonstrated by using cyclic voltammetry to monitor the adhesion of murine 3T3 fibroblasts in the presence of a redox reporter. The charge transfer across the working electrode was reduced upon cell adhesion, which was used as the detection mechanism, and allowed the detection of as few as 24 cells. The effective utilization of simple

and low cost bench-top fabrication methods could accelerate the prototyping and development of LoC technologies and bring PoC diagnostics and personalized medicine to the patients' bedside.

Keywords: fibroblast; shape memory polymer; flexible biosensor; cyclic voltammetry; cell sensor; xurography; stencil lift-off; on-chip electrochemical sensor

2.1. INTRODUCTION

Sustainable global healthcare is a long sought-after idea [1]. Innovation in modern health care diagnostic techniques continues to improve patient outcomes, but the cost of bringing the technology to patients worldwide increases concomitantly. Ever since the inception of the portable glucose meter, scientists and engineers have been interested in lab-on-a-chip (LoC) devices for point-of-care (PoC) detection as low-cost and portable solutions to health screening, diagnostics, and personalized medicine [2,3]. To fabricate such devices on a mobile platform, LoC technology requires an all-in-one solution comprised of sensing and conducting elements within a microfluidic channel of sub-millimeter dimension [4].

Microfabricated on-chip microfluidic electrochemical biosensors have the advantage of being label-free, and offer high sensitivity and quantitative detection of analytes over a much broader concentration range than their fluorescence or colorimetric counterparts [4–9]. Most traditional microfabrication techniques are inherited from the semiconductor industry, where lithography [10–12], thin film deposition [12,13], and etching are routinely employed [12,14]. These techniques are very effective at producing high-resolution patterns at the micro- to nanoscale on a wide variety of materials. Yet, traditional microfabrication approaches can require expensive equipment, access to cleanroom facilities, multistep processes, and often limit themselves to rigid and non-transparent substrates. Some alternatives to making on-chip μF biosensors take advantage of soft silicone elastomers (e.g., poly (dimethylsiloxane)—PDMS) bonded to glass, silicon wafers, or polystyrene sheets through bonding techniques such as plasma oxidation and surface chemical grafting [13,15–18]. These methods offer a cost-effective bench-top alternative for the fabrication of μF devices without the use of expensive cleanroom facilities. Furthermore, μF devices for applications such as conformal pressure sensors, and flexible and transparent electronics, need to be implemented on soft and flexible materials, which sometimes cannot be processed through traditional methods. To overcome the limitations of cost, time, material properties, and processing, non-traditional techniques are being explored, including xurography [13,15,18], adhesive stencil lift off [15,18–20], shape-memory polymers (SMP) [13,15,20–22], ink jet printing [23,24], paper-based microfluidic devices [5,7,25–27], and 3D printing [28,29]. Despite the reduced resolution when compared to traditional microfabrication, these modern techniques offer lower costs and shorter turnaround time, two important factors for rapid prototype development and commercial scalability.

Recently, SMPs have gained significant traction in the microfabrication community for their ability to produce 3D micro/nanostructured surfaces on a variety of thin films (e.g., Au, Pt, CNT, SiO_2, and TiO_2) [13,20,30–35]. The structured surfaces are produced through a compressive stress applied by the SMP during shrinking once it is heated over its glass transition temperature [21,36]. This technique has been shown to successfully structure gold films for use as electrodes for electrochemical sensing [13,15,20,37] and as substrates for surface-enhanced Raman scattering [13,38–40]. The micro/nanostructures described in the literature showed increased electroactive surface area for working electrodes, ideal for sensing within µF devices. This simple bench-top fabrication approach presents an attractive route for the integration of highly sensitive electrochemical techniques into flexible LoC microfluidic devices.

This work presents a benchtop, low-cost, and rapid method for fabricating a highly sensitive, all-PDMS, µF electrochemical sensor, and demonstrates its sensing capabilities through the detection of the adhesion of murine 3T3 fibroblast cells—the most abundant cells in connective tissue and critical components in wound healing—onto the surface of the electrode. Commercial PDMS elastomer and pre-stressed polystyrene were used as the bulk substrates for the µF device and to fabricate the 3D micro/nanostructured electrodes, respectively. A salt-bridge-free three-electrode electrochemical µF device was fabricated to encapsulate the structured gold working, auxiliary, and platinum reference electrodes for an all-PDMS µF sensor. Cyclic voltammetry was employed to study the flow rate effects on charge transfer efficiency of the structured electrodes. Finally, fibroblasts were incubated and adhered onto the structured electrode and sensed using a redox reporter. This work demonstrates proof-of-concept for a novel rapid prototyping method to fabricate a transparent flexible sensor possessing high sensitivity and reproducibility. We anticipate that further surface functionalization of the structured electrodes will lead to inexpensive devices for the label-free detection of specific cell types, DNA-aptamer binding, and electrochemical or fluorescence sensing for applications in personalized precision medicine and PoC diagnostics.

2.2. MATERIALS AND METHODS

2.2.1. Electrode Fabrication

The structured electrodes used within the microfluidic device were fabricated using a vinyl stencil lift-off and pre-stressed polystyrene (PS) shrinking method previously described (Figure 2.1) [20]. Briefly, the PS sheets (Shrink Film, Graphix, Maple Heights, OH, USA) were cut to the desired shape using a blade cutter (ROBOPro CE5000-40-CRP, Graphtec America Inc., Irvine, CA, USA) followed by a 3-step wash with isopropyl alcohol, ethanol, and 18.2 MΩ water under constant agitation at 60 rpm, and dried under a nitrogen (N_2) stream. The clean PS sheets were spin-coated with a positive-tone photoresist (PR, Shipley 1818, Marlborough, MA, USA) layer with a 1.8 μm nominal thickness. The PR-coated PS sheets were then baked on a hot plate at 90 °C for 3 min to remove residual solvent. The self-adhesive vinyl (FDC-4300, FDC graphics films, South Bend, IN, USA) shadow masks were also patterned using the blade cutter to the specific electrode dimensions for the working (WE) auxiliary (AE) and reference electrodes (RE), which were set to 10.8 mm × 1.6 mm × 4.8 mm, 10.8 mm × 3.0 mm × 4.8 mm, and 10.8 mm × 3.0 mm × 4.8 mm (length × width × pad diameter), respectively (Figure 2.S1). The adhesive vinyl masks were then transferred onto the clean PS and served as stencils during the metal deposition process. Gold (99.999% purity, LTS Chemical Inc., Chestnut Ridge, NY, USA) and platinum were deposited using a Torr Compact Research Coater CRC-600 manual planar magnetron sputtering system (Torr International, New Windsor, NY, USA) at deposition rates of ~1 Å/s (100 nm) and ~0.1 Å/s (150 nm), respectively. Following this step, the vinyl stencils were lifted off and the PS sheets were placed in an oven heated at 160 °C, which shrunk the PS substrates to ~16% of their original size by area [15,20]. The structured metal films were lifted off from the PS by dissolving the PR in an acetone bath under constant agitation at 80 rpm for 30 min. Once the electrodes were lifted off from the PS, they were stored in acetone until further use.

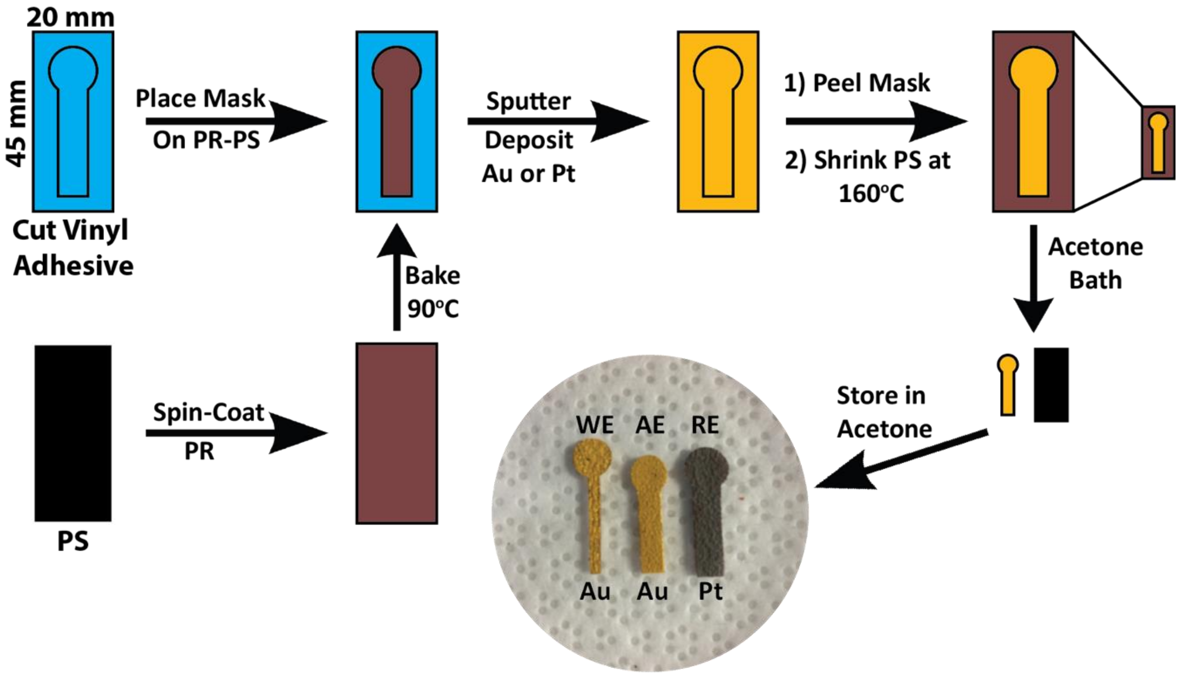

Figure 2.1. Schematic of the bench-top fabrication method for the patterning, structuring and lift-off of the working, auxiliary, and reference electrodes (WE, AE, RE). Electrodes were patterned by cutting vinyl adhesive stencils (blue) to the desired shape and placing them on photoresist (PR, maroon) coated pre-stressed polystyrene (PS, black). Gold (100 nm) and platinum (150 nm) were sputtered onto the masked substrates followed by removal of the vinyl stencils. The sputtered flat electrodes were then subjected to heat at 160 °C to shrink the PS substrate down to 16% of its original area. The shrinking process resulted in Au and Pt micro/nanostructured electrodes, which were then lifted off by dissolving the PR in an acetone bath.

2.2.2. All PDMS µF Device Fabrication

The µF channel mold was patterned using the blade cutter into a Bytac® PTFE surface protection laminate (Sigma-Aldrich, St. Louis, MO, USA) adhesive film with 125 µm nominal thickness. The patterned mold dimensions are shown in Figure 2.2a. 3D printed corrals defining the size of the PDMS µF layers (white, Figure 2.2a) were fabricated out of acrylonitrile butadiene styrene polymer using a Replicator 2X Experimental 3D Printer (MakerBot Industries, Brooklyn, NY, USA). The PTFE adhesive channel mold and 3D printed corral were placed on top of a 3-inch Si wafer and silicone tubing (Masterflex, Gelsenkirchen, Germany) was placed on top of the inlet and outlet reservoirs of the PTFE mold. A Sylgard-184 (Dow Corning, Midland, MI, USA) elastomer and hardener were mixed in a 10:1 ratio, degassed for 20 min, and poured into the 3D printed corrals. The top PDMS layer (2, Figure 2.2a) was placed first in an oven at 60 °C for 20 min followed by the bottom layer (1, Figure 2.2a) for the remaining 20 min before both halves were taken out of the oven and allowed to cool to room temperature. The structured Au [working (WE) and auxiliary (AE)] and Pt [reference (RE)] electrodes were placed on top of PDMS Layer 1. PDMS Layer 2 was removed from the 3D mold, and both layers were treated with air plasma for 30 s (30 sccm air inlet flow and 600 mTorr pressure) at a high-power setting (30 W) in a PDC expanded plasma cleaner (Harrick, Ithaca, NY, USA). The two layers were then bonded and left to fully cure at 60 °C for 1 h (Figure 2.2b).

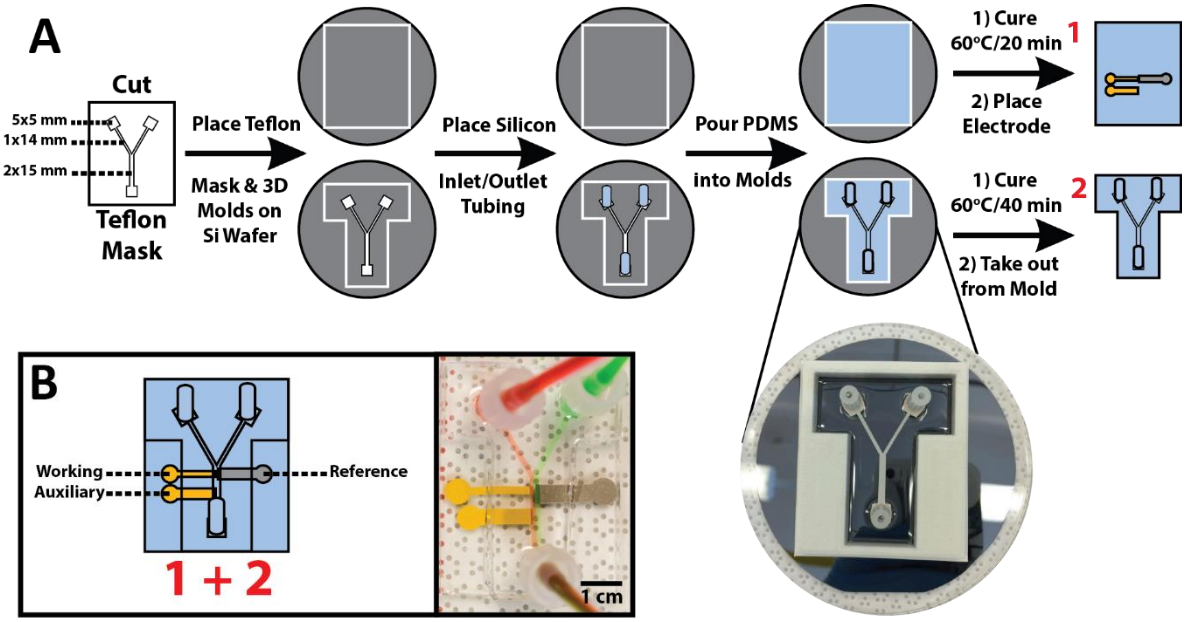

Figure 2.2. Bench-top microfabrication process for making the all-PDMS on-chip μF electrochemical biosensors. **(A)** A Teflon adhesive μF channel mold was cut and placed inside a 3D printed device mold on top of a Si-wafer to ensure surface flatness. Silicon tubing was placed at the inlet/outlet positions, and PDMS was poured into the mold until full. The bottom layer (1) was partially cured at 60 °C for 20 min followed by placement of the three electrodes.

The top layer (2) was cured at 60 °C for 40 min and removed from its mold. **(B)** PDMS Layers (1) and (2) were plasma treated for 30 s, bonded, and allowed to fully cure at 60 °C for 1 h.

2.2.3. Dead-End Pressure Test of PDMS Bond Strength

All dead-end pressure tests were performed in triplicate for each bonding condition. A dead-end chamber with dimensions of 7 mm × 7 mm × 0.125 mm was made using patterned square PTFE molds as described above. The dead-end devices were attached to a N_2 (g) source with an inline pressure gauge and placed in a beaker filled with water. The N_2 (g) flow was increased until the water began to bubble, indicating that the device had burst through delamination or mechanical failure (Video S1 and Figure 2.S2).

2.2.4. Murine 3T3 Fibroblast Cell Culture

Murine 3T3 fibroblast cells were prepared through standard cell culturing procedures. Briefly, Dulbecco's modified eagle's medium (DMEM, supplemented with 10% FBS, 1% L-glutamine, 1% penicillin/streptomycin (Invitrogen, Life Technologies, Burlington, ON, Canada)) was heated to 37 °C and 30 mL were pipetted into a 50 mL conical tube kept at 37 °C. A Frozen cryovial of murine 3T3 fibroblasts (ATCC, Manassas, VA, USA) was rapidly thawed by swirling the contents in a 37 °C water bath. To remove DMSO (Caledon Laboratory Chemicals, Georgetown, ON, Canada) from the cryovial contents, the contents were poured into the media kept at 37 °C and centrifuged at 500g for 5 min. The supernatant was discarded, and the cell pellet was re-suspended in 15 mL of supplemented DMEM and incubated overnight in a T25 tissue culture flask (Sigma-Aldrich, Oakville, ON, Canada). Once the cells had grown to the desired confluency, they were detached from the culture flask by adding a trypsin solution (TrypLE, Thermo Fisher, Waltham, MA, USA) at 37 °C for 3–5 min. To neutralize the trypsin, an equal amount of DMEM was added (supplemented with 10% Fetal Bovine Serum and 1% Penicillin—both from Thermo Fisher, Waltham, MA, USA). The cell solution was then pipetted into a centrifuge tube and centrifuged at 500g for 5 min followed by extraction of the supernatant. The cells were re-suspended with the desired amount of DMEM and counted using a hemocytometer cell counter and a light microscope. Finally, the cell solution was diluted to 2×10^6 cells/mL using DMEM and stored at 37 °C and 5% CO_2(g) until use in the μF cell incubation step.

2.2.5. CFSE Fibroblast Cell Staining

A solution containing 50 μM CFSE (5(6)-carboxyfluorescein diacetate N-succinimidyl ester, Sigma-Aldrich, Oakville, ON, Canada) was prepared from a 1 mM stock and 0.1% FBS in 1× PBS (phosphate buffer saline, 100 mM, pH = 7.4). Following this, 2×10^6 fibroblast cells were added to 200 μL of the CFSE solution, gently mixed and incubated at 37 °C in the dark for 1 h. After the incubation period, 200 μL of 100% FBS was added to the mixture and incubated at 37 °C for 10 min in the dark. The mixture was then centrifuged at 500g for 5 min with the resulting pellet being washed 3 times with 10% FBS in 1× PBS solution. Finally, the pellet was re-suspended to the desired concentration in DMEM.

2.2.6. Cell Viability Assay

The viability assay for Au-PDMS substrates was carried out with PrestoBlue (Invitrogen, San Diego, CA, USA) in a 48-well plate. To start, 10^4 fibroblasts in 1 mL of DMEM were plated in each of the 12 wells and incubated at 37 °C/5% CO_2 for 24 h to ensure optimal cell adhesion. Among these, 4 wells contained Au-PDMS substrates, 4 were used to test 1 h 1× PBS incubation, and the last 4 were used for the DMEM control. For the viability assay, the media in all 12 wells was substituted with 180 μL of 1× PBS and 20 μL of 10x PrestoBlue solution. After 30 min of cell incubation at 37 °C and 5% CO_2, the change in the fluorescence of the samples was measured using a Cytation multi-well plate reader (Biotek Instruments Inc., Montreal, QC, Canada) with the excitation/emission wavelengths set at 535/615 nm.

2.2.7. Murine 3T3 Fibroblast Cell Sensing

The Au electrodes (WE and AE) in the PDMS μF device were preconditioned and baselined through cyclic voltammetry (CV). A 100 mM H_2SO_4 working solution and a 1× PBS reference solution were pumped through the μF device in separate laminar streams at 0.1 mL/min using a PHD ULTRA™ Syringe Pump (Harvard Apparatus, Holliston, MA, USA). The devices were preconditioned through 30 CV scans for the working electrode performed from 0.0 to 1.4 V at a scan rate of 0.10 V/s using a CHI600E electrochemical workstation (CH Instruments, Austin, TX, USA). Following the preconditioning step, the entire μF channel was washed with 1× PBS for 5 min at 0.10 mL/min. Prior to cell incubation, a baseline CV scan was performed on each μF device, yielding the total current for the clean WE. A sensing solution of 5 mM $K_4[Fe(CN)_6]$ in DMEM was continuously pumped through the device at 0.1

mL/min, and a 10 segment CV scan was performed from −0.4 to 0.2 V (with respect to the RE) at a scan rate of 0.10 V/s. Once again, the device was washed by flowing 1× PBS for 5 min at 0.1 mL/min. Finally, a fibroblast solution containing 2×10^6 cells/mL in DMEM was pumped through the μF stream flowing over the WE at 0.1 mL/min for 1 min and then stopped to allow for fibroblast attachment onto the WE for 1 h at 37 °C and 5% CO_2(g). After cell adhesion, the μF device was flushed with the sensing solution, and CV scans were performed as described above. Experiments were performed on three replicate devices to assess reproducibility and the statistical significance of the results.

2.2.8. Fluorescent Microscopy Image Acquisition

The murine 3T3 fibroblast cells inside the μF channel were imaged using a Nikon Eclipse LV100N POL epifluorescence microscope (Nikon Instruments, Mississauga, ON, Canada) equipped with excitation and emission filters for FITC dye, and a Nikon MRP50102 10×/0.25 NA Pol objective. Images were acquired with a Retiga 2000R cooled CCD camera (QImaging, Surrey, BC, Canada) and recorded with NIS-Elements AR software (Nikon Instruments, Mississauga, ON, Canada). The images were taken at 200 ms exposure time, 2 × 2 binning, and a hardware gain of 10.

2.3. RESULTS AND DISCUSSION

2.3.1. Optimization of PDMS Device Bond Strength for μF Device Fabrication

A viable flexible μF sensing platform must match or surpass current μF solutions in reproducibility, sensitivity, and reliability. The challenge in having a flexible all-PDMS μF sensor is that its intrinsic mechanical flexibility can introduce delamination at the bonding interface between the two PDMS layers of the μF device as it is being handled. In particular, the PDMS device should be strong enough to withstand the pressures generated from pressurized flow through the microfluidic channel. Therefore, the characterization and optimization of the bond strength between the two layers of a silicone-based μF device is crucial for the production of a reliable and flexible μF sensing platform. The bond strength of various bonding conditions was quantified using a dead-end chamber pressure test. To perform such a test, triplicate devices with dead-end chamber dimensions of 7 mm × 7 mm × 0.125 mm were made as described in the Materials and Methods section, and the bond strength was measured by pressurizing gas into the dead-end device until either the device delaminated or the PDMS layer/inlet tubing burst. The burst pressure was actively monitored using an inline pressure gauge. Performing the burst pressure test with the devices submerged in water provided an immediate indication of the device failure, as the escaping pressurized gas produced vigorous bubbling in the solution (Figure 2.3a, Video S1). Figure 2.3b shows a comparison of the burst pressure for different PDMS–PDMS bonding conditions benchmarked against the standard PDMS–glass interface, and a comparison of a device integrating a structured electrode 5 mm in width with and without PDMS sealing at the electrode–PDMS interface.

The bonding conditions depicted in Figure 2.3b for PDMS devices without a structured electrode differ only in the combination of PDMS curing time (partially cured–PC vs. fully cured–FC), with every treatment subjected to 30 s air plasma treatment prior to device bonding. PC PDMS was made by subjecting the PDMS to 60 °C for 20 min and fully cured FC PDMS was subjected to 60 °C for 40 min prior to bonding followed by a final curing step at 60 °C for 1 h. The devices were allowed to form stable bonds at room temperature for 24 h after the initial bonding. FC–FC PDMS bonding exhibited an average burst pressure of 170 ± 40 kPa, which was ~50% lower than the FC–glass benchmark of 330 ± 10 kPa. The FC–PC and PC–PC combination produced statistically equivalent dead-end burst pressures to the benchmark, failing at 350 ± 20 and 310 ± 50 kPa, respectively. The increased bond strength observed in the FC–PC and PC–PC compared to the FC–FC devices can be attributed to having both hydrosilylation and dehydration reactions occurring at the interface. The hydrosilylation reaction is facilitated by a Pt catalyst found in the Sylgard-184 cross-linker and occurs when free silicon hydride (SiR_3-H) groups found in the Sylgard-184 elastomer base crosslinks with the vinyl-terminated polysiloxanes found in the Sylgard-184 cross-linker. Hydrosilylation can only occur with the partially cured PDMS mixture, where silicone chains are relatively mobile, while the condensation reaction occurs between two adjacent silanol (SiR_3–OH) groups, which will react to form Si–O–Si bonds and eliminate H_2O as a by-product. By exposing the two PDMS surfaces to plasma oxidation, we can generate surface SiR_3–OH, which will contribute to strengthening the PDMS–PDMS bonding interface over time. In addition, using the PC PDMS, the surface roughness effects on bonding are minimized, since the PC surface is still moldable and can conform to the complementary bonding layer. In view of the bonding strength test results for all-PDMS layers, we chose to use the FC–PC combination for the fabrication of devices incorporating structured electrodes, since it has a comparable failure pressure to the FC PDMS–glass benchmark, is relatively easy to handle, and has higher reproducibility than the FC–FC combination. Optimization of the bonding with layers containing structured electrodes was done using the same dead-end layout, but with the integration of a structured electrode that covered ~70% of one of the side walls (inset, Figure 2.3c). This setup was chosen to test the disruption in bonding strength with an extreme case of electrode-to-sidewall ratio. As anticipated, once a structured electrode was in place, the bonding strength was much weaker (0.9 ± 0.1 kPa, Figure 2.3c) than that observed with the all-PDMS FC–PC combination. To overcome such weak bonding, we resorted to sealing the device edges with freshly mixed PDMS after the initial bonding, with the intent to reinforce the device bond at the site of the electrode. By sealing the device with the PDMS mix and then curing, the device burst pressure increased >36-fold (33.0 ± 0.4 kPa, Figure 2.3c) when compared to the devices without sealing. This technique was then used on the μF device, and the burst flow rate was determined. With the PDMS sealing, the burst flow rate was determined to be >100 mL/min (maximum capability of the syringe pump). Thus, the bond strength with the optimized fabrication procedure is more than suitable for experimentation, where flow rates >4 mL/min have been shown to detach murine 3T3 fibroblast cells incubated within μF devices of similar dimensions without the use of fibronectin as an adhesion promoter [41].

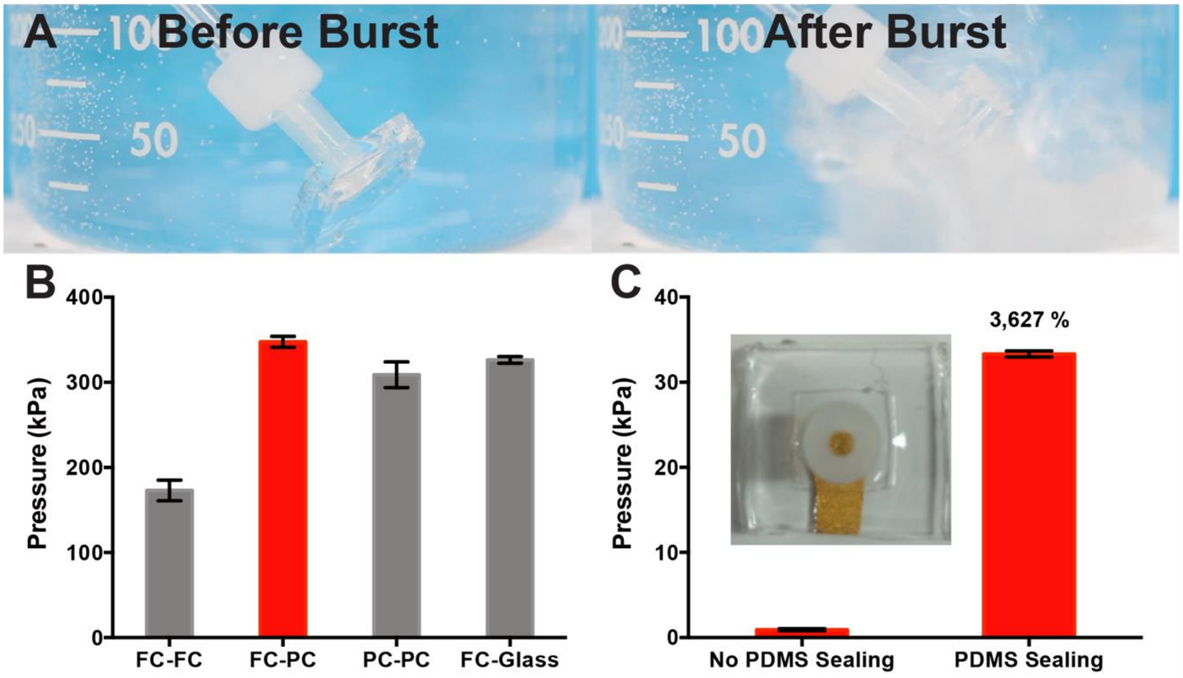

Figure 2.3. PDMS bonding strength characterization All PDMS curing was done in a 60 °C oven with the following curing times as follows: fully cured (FC)—40 min; partially cured (PC)—20 min. **(A)** Image of the burst pressure test with the intact dead-end µF device (left) and the broken device (right). **(B)** Quantification of the burst pressure for different bonding combinations of FC–FC PDMS layers, PC–FC PDMS layers, PC–PC PDMS layers, and FC PDMS layer-glass. **(C)** Quantification of the burst pressure for a dead-end µF device with a 5 mm Au electrode in place. Graph compares devices without PDMS sealing around the device vs. with PDMS sealing after bonding. The inset shows a sample image of the dead-end burst pressure device with the Au electrode in place as would be seen in the µF device. All error bars represent the standard error of the mean, *n* = 3.

Using FC–PC bonding and sealing procedure, all the subsequent PDMS µF devices were made in accordance to the process depicted in Figure 2.2a. The challenges in fabricating such devices with high reproducibility were in the careful placement of the three electrodes in the appropriate configuration, and the successful bonding over the structured electrode surfaces. It was found that following the 20 min curing step for the bottom half of the µF device, the three electrodes had to be immediately transferred from the acetone storage solution to the PDMS to take full advantage of the tackiness of the PC–PDMS for maximal electrode-to-PDMS adhesion. Once the electrodes had made contact with the PC–PDMS, the adhesion became too strong to remove the electrodes without destroying them. Since the transfer must be done successfully in one attempt, placing the electrodes one by one would require very high dexterity and precision to fabricate µF devices with acceptable reproducibility. To overcome this challenge, a Teflon filter membrane was used as a base support for the configuration and transfer of the electrodes in a single step. To ensure that the electrodes adhered to the Teflon membrane and that the membrane did not stick to the PC–PDMS, the membrane was pre-wet with a small amount of acetone (this also afforded transparency through the Teflon membrane for optimal electrode configuration). The electrodes were then removed from the storage solution using flat tweezers and placed on the membrane. At this stage, the electrodes could be easily positioned into the appropriate configuration without damaging them. Once in position, the electrodes were picked up by the Teflon membrane and placed on top of the PC–PDMS. Upon electrode to PC–PDMS contact, the membrane was then quickly removed. The final steps in the assembly and bonding of the µF devices were performed as described in the Materials and Methods section and depicted in Figure 2.2a.

2.3.2. Impact of Flow Rate on Electrochemical Sensing

Once the fabrication protocol for the µF devices was optimized, we turned our attention to the electrochemical sensing stability within the devices. Throughout this study, we utilized cyclic voltammetry (CV), a simple electrochemical technique that is commonly used to quantify redox processes and can be leveraged to implement cell-sensing strategies. CV is a diffusion-limited technique when the sensing of the redox process is performed in an unstirred solution, such that the analytes are not disturbed as they are undergoing reduction-oxidation cycles. Performing CV measurements in a flow cell, such as a µF channel, with variable flow rates could mimic a stirred cell condition resulting in limitations to charge transfer efficiencies across the working electrode, thus reducing the overall device sensitivity.

To perform on-chip electrochemical sensing and assess the impact of the flow rate on electrochemical sensing, a salt-bridge-free three electrode system was fabricated to incorporate Au WE and AE, and Pt RE in a Y-shaped bench-top fabricated PDMS µF device (cf. Figure 2.2b). The salt-bridge-free µF design exploits the laminar flow within the microfluidic channel to isolate the RE from the working sample solution, while still allowing the diffusion of the supporting electrolyte across the laminar flow interface. The separation between the working solution and the reference solution is critical in the stability of the potential output during sensing through CV. Given that the structured Pt film is used as a hydrogen pseudo-reference electrode, its half-cell potential is dependent on the concentration of hydronium ions (i.e., pH). To prevent fluctuations in pH, a buffer solution (1xPBS, pH = 7.4) was pumped through the reference inlet to be in constant contact with the RE, thus maintaining a constant reference electrode potential.

To assess the impact of the working flow rates used for sensing on charge transfer, we performed a series of CV measurements in the µF devices at flow rates from 0–0.5 mL/min. The CV for each flow rate was obtained in a 5 mM $K_4[Fe(CN)_6]$ in 1× PBS working solution and a 1× PBS reference solution utilizing the laminar flow inside the µF channel to separate the working and reference solutions (demonstrated in Video S2 using coloured solutions). Figure 2.4a shows an overlay of the cyclic voltammograms for the different flow rate conditions, with cathodic peaks shifting from −0.22 to −0.18 V with respect to stopped flow (blue curve, 0 mL/min). To perform the stopped flow sensing, the solution was pumped into the µF device, then the flow was stopped, and CV scans were then performed. The voltammogram shows a change in CV curve shape from a classic "duck" shape to a sigmoidal shape from low to high flow rates. The change in shape indicates that at higher flow rates we begin to reach a limit at which the convection introduced by the laminar flow is much greater than the redox kinetics of $K_4[Fe(CN)_6]$. The result is non-uniform anodic peak current to cathodic peak current and ultimately a change from a completely reversible process to a quasi-reversible process. Despite the signal shifts, the integration of the reduction peaks (Figure 2.4b) provides a quantification of the charge transfer, showing that there is an initial reduction in total charge to ~73% compared to the stopped flow. Between the flow rates of 0.1 and 0.5 mL/min, there is no statistical difference in charge transfer efficiencies. After confirming that the working flow rates (0.1–0.5 mL/min) did not negatively impact the electrochemical sensing capabilities of the PDMS µF device, we chose the lowest working flow rate tested of 0.10 mL/min for the murine 3T3 fibroblast cell sensing. This minimized the risk of cell detachment, while maintaining a continuous flow within the μF device. Minimizing cell detachment during the sensing period is essential during the acquisition of the voltammograms, since any such event would cause a significant increase in charge transfer efficiency at the working electrode.

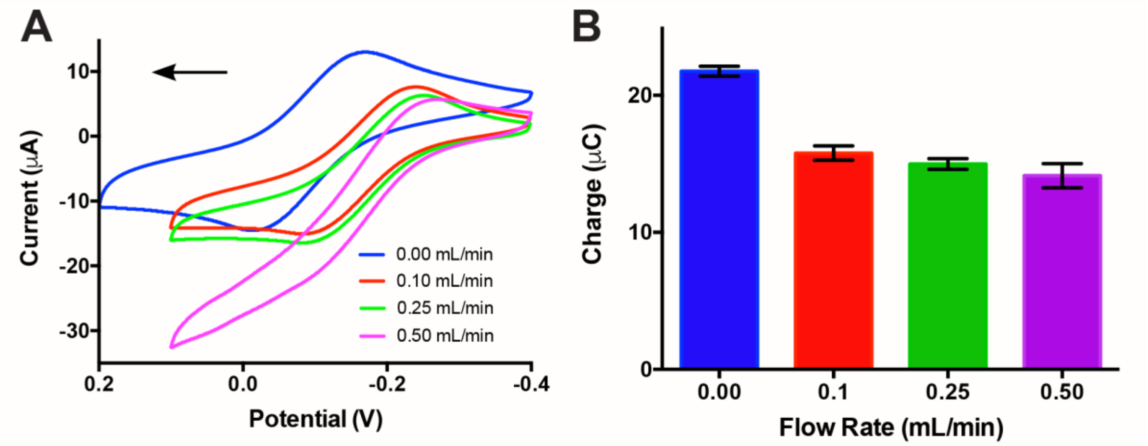

Figure 2.4. Assessment of the impact of flow rate on charge transfer efficiency. The cyclic voltammetry experiments were performed using a 5 mM $K_4[Fe(CN)_6]$ working solution at a 0.10 V/s scan rate. **(A)** Cyclic voltammograms showing changes in reduction and oxidation peaks and down-right shifting of the voltammograms as flow rate increased from 0 to 0.5 mL/min with a positive initial scan direction as indicated by the arrow. **(B)** Quantification of the total charge transfer in the cathodic peak for the different flow rates. Between flow rates of 0.1 and 0.5 mL/min, there is no statistical difference in charge transfer efficiency.

2.3.3. On-Chip Cell Detection

To evaluate the impact of DMEM on electrochemical sensing over the incubation time, CV was performed immediately after being exposed to DMEM, and in DMEM after incubation for 1 h. We observed no statistical difference between the voltammograms obtained in DMEM immediately after exposure and those obtained after 1 h of incubation (Figure 2.S4). Prior to on-chip cell detection, the murine 3T3 fibroblast cells were introduced into the μF channel by pumping through a solution containing 2 × 10^6 cells/mL in DMEM at 0.1 mL/min for 1 min, stopping the flow, and allowing the cells to attach to the WE by incubating them in the device for 1 h at 37 °C. The total volume of the device was ~2 µL, which translates into ~4000 fibroblast cells within the device at any given time. The experiment was performed on triplicate devices on the same day within a 4 h timeframe to minimize variability in cell adhesion and sensing due to ageing of the cells. After cell incubation, the µF was washed by pumping it through DMEM at 0.1 mL/min for 2 min to remove any weakly bound or unbound cells from the electrode surface. Using the minimal flow rate of 0.1 mL/min, the adhered murine 3T3 fibroblast cells were sensed in a DMEM working solution supplemented with 5 mM $K_4[Fe(CN)_6]$. During cell sensing, the redox-reporter was monitored through CV, where Figure 2.5a presents a typical voltammogram showing the cathodic peaks for a device before (blue) and after 3T3 cell incubation (red). The cells inside the µF device were monitored throughout the adhesion steps with fluorescence microscopy and a live CFSE cell stain, which can be seen in Figure 2.S3. The figure shows images comparing the number of cells located on the Au–WE before incubation, after incubation (washed), and after sensing vs. control plain Au–WE. After sensing, the average number of cells counted on the WE (0.8 × 1.6 mm geometric area) was ~24 cells.

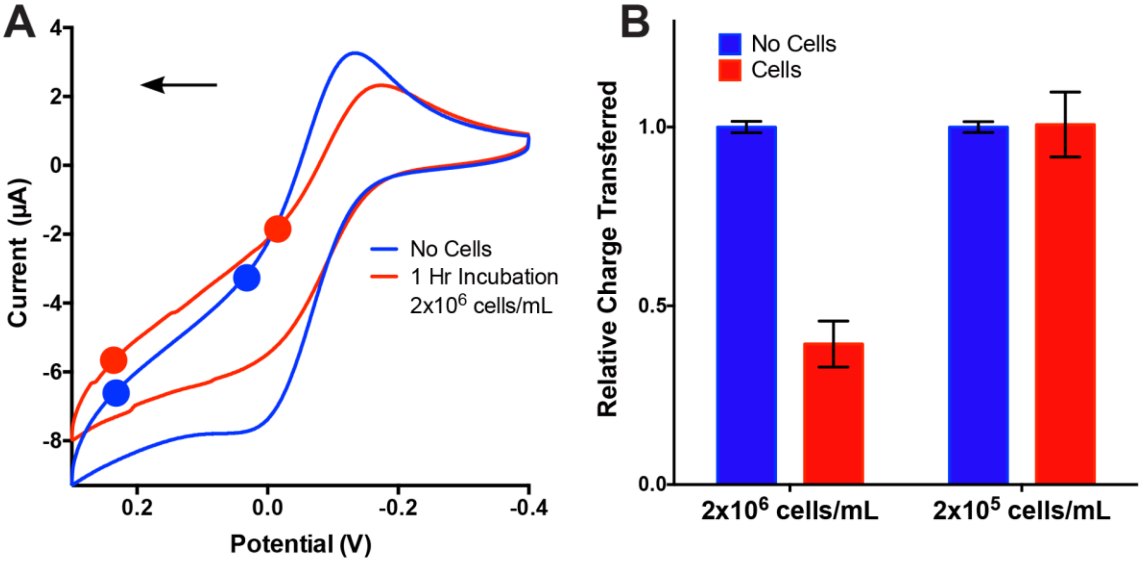

Figure 2.5. Fibroblast sensing in 5 mM $K_4[Fe(CN)_6]$ solution at a 0.1 mL/min flow rate. **(A)** Cyclic voltammogram of the detection of murine 3T3 fibroblast cells vs. control electrode. **(B)**

Relative charge transferred by the working electrode during the detection of murine 3T3 fibroblast cell vs. the control electrode. All error bars represent the standard error of the mean, *n* = 3.

To quantify the adhesion of cells to the electrode, the cathodic peaks of the CVs were integrated and the total charge transferred calculated. For the cathodic peak integration, the baseline correction was done through a linear regression using two points seen on each cyclic voltammogram (Figure 2.5a). To avoid any integration bias, the first point was placed at the initial leveling during the reduction sweep and the second point was placed at the base of the reduction peak. Upon integrating the cathodic peaks (Figure 2.5b), a 61% loss of charge transfer was recorded after incubation for the 2×10^6 cell/mL solution. When the cell concentration was reduced by an order of magnitude, the electrochemical signal did not change. We attribute this to the low cell concentration in the seeding solution, where in the absence of adhesion proteins like fibronectin, we would expect one or two cells to adhere to the electrode area. This number of cells might be too low to produce a significant change in the electrochemical signal. The CV results show that the PDMS μF sensors were successful in detecting cell adhesion from murine 3T3 fibroblast cells at a relatively low number of cells (~24) and in a low sample volume. The sensitivity of the all-PDMS μF biosensor can be attributed to the use of structured working electrodes. Micro/nanostructuring of deposited thin metal films electrodes through the use of shape-memory-polymers has previously been shown to increase the electroactive surface area per geometric area by ~600% when compared to their flat counterparts [30]. Thus, the area blocked by any individual adhered cell is 6-fold higher than it would be for a traditional flat electrode. While we have demonstrated the capability of detecting murine 3T3 fibroblast cells, the described proof-of-concept detection approach is not specific. Our current efforts are directed towards the functionalization of the structured electrodes with capturing agents that selectively bind targeted cells. This will lead to a reduction in sensing time, improved sensitivity, and reproducibility.

2.4. CONCLUSION

This work demonstrates a novel, rapid, and cost-effective method for the integration of 3D structured high surface area electrodes into all-PDMS μF devices. The use of xurography on vinyl, PTFE, and PS and 3D printing offers a simple approach for the rapid and inexpensive prototyping and mold fabrication for μF devices. The optimized PDMS–PDMS bonding and sealing conditions offer bond strengths that allow the operation of the microfluidic devices under high flow rates and offer long-lasting encapsulation of the high surface area structured electrochemical sensors. In addition, the μF devices showed sustained charge transfer that was minimally disturbed by relatively low flow rates, as shown through cyclic voltammetry. The on-chip electrochemical sensing capabilities of bench-top fabricated μF devices were demonstrated by sensing the adhesion of model murine 3T3 fibroblast cells, where the signal decreased ~61% after the adhesion of an average of 24 cells over the working electrode. This highlights the excellent sensitivity of the structured Au electrodes. The bench-top fabrication method presented in this work offers a rapid, reproducible, and highly sensitive prototyping method that shows promise for the future prototyping of flexible devices for portable point-of-care diagnostics and personalized medicine.

Supplementary Materials: The following materials are available online at www.mdpi.com/link: Figure 2.S1, Table 2.S1, Video 2.S1 and Video 2.S2.

Acknowledgments: This work was supported through the Natural Sciences and Engineering Research Council and a Canada Foundation for Innovation Leaders Opportunity Fund. Jose Moran-Mirabal is the recipient of an Early Researcher Award through the Ontario Ministry of Research and Innovation. We thank Fei Xu and Todd Hoare for kindly providing the murine 3T3 fibroblast cells used in this study.

Author Contributions: K.S. and J.M.-M. conceived and designed the experiments; K.S., Y.Z., and H.L. performed the experiments; K.S. and J.M.-M. analyzed the data; K.S. and J.M.-M. wrote the paper.

Conflicts of Interest:

The authors declare no conflicts of interest.

REFERENCES

1. Cordell, G.A. Sustainable medicines and global health care. *Planta Med.* **2011**, *77*, 1129–1138.

2. Chin, C.D.; Linder, V.; Sia, S.K.; Daar, A.S.; Thorsteinsdottir, H.; Martin, D.K. Lab-on-a-chip devices for global health: Past studies and future opportunities. *Lab Chip* **2007**, *7*, 41–57.

3. Yager, P.; Domingo, G.J.; Gerdes, J. Point-of-care diagnostics for global health. *Annu. Rev. Biomed. Eng.* **2008**, *10*, 107–44.

4. Zhang, S.; Wright, G.; Yang, Y. Materials and techniques for electrochemical biosensor design and construction. *Biosens. Bioelectron.* **2000**, *15*, 273–282.

5. Dungchai, W.; Chailapakul, O.; Henry, C.S. Use of multiple colorimetric indicators for paper-based microfluidic devices. *Anal. Chim. Acta* **2010**, *674*, 227–233.

6. Chabinyc, M.L.; Chiu, D.T.; McDonald, J.C.; Stroock, A.D.; Christian, J.F.; Karger, A.M.; Whitesides, G.M. An integrated fluorescence detection system in poly (dimethylsiloxane) for microfluidic applications. *Anal. Chem.* **2001**, *73*, 4491–4498.

7. Nie, Z.; Nijhuis, C.A.; Gong, J.; Chen, X.; Kumachev, A.; Martinez, A.W.; Narovlyansky, M.; Whitesides, G.M. Electrochemical sensing in paper-based microfluidic devices. *Lab Chip* **2010**, *10*, 477–83.

8. Kwakye, S.; Goral, V.N.; Baeumner, A.J. Electrochemical microfluidic biosensor for nucleic acid detection with integrated minipotentiostat. *Biosens. Bioelectron.* **2006**, *21*, 2217–2223.

9. Dhahi, T.H.S.; Bin Hashim, U.D.A.; Ahmed, N.M.; Mat Taib, A. A review on the electrochemical sensors and biosensors composed of nanogaps as sensing material. *J. Optoelectron. Adv. Mater.* **2010**, *12*, 1857–1862.

10. Bhattacharyya, A.; Klapperich, C.M. Design and testing of a disposable microfluidic chemiluminescent immunoassay for disease biomarkers in human serum samples. *Biomed. Microdevices* **2007**, *9*, 245–251.

11. Khine, M.; Ionescu-Zanetti, C.; Blatz, A.; Wang, L.-P.; Lee, L.P. Single-cell electroporation arrays with real-time monitoring and feedback control. *Lab Chip* **2007**, *7*, 457–462.
12. Ziaie, B.; Baldi, A.; Lei, M.; Gu, Y.; Siegel, R.A. Hard and soft micromachining for BioMEMS: Review of techniques and examples of applications in microfluidics and drug delivery. *Adv. Drug Deliv. Rev.* **2004**, *56*, 145–172.
13. Sharma, H.; Nguyen, D.; Chen, A.; Lew, V.; Khine, M. Unconventional low-cost fabrication and patterning techniques for point of care diagnostics. *Ann. Biomed. Eng.* **2011**, *39*, 1313–1327.
14. Waits, C.M.; Morgan, B.; Kastantin, M.; Ghodssi, R. Microfabrication of 3D silicon MEMS structures using gray-scale lithography and deep reactive ion etching. *Sens. Actuators A Phys.* **2005**, *119*, 245–253.
15. Sonney, S.; Shek, N.; Moran-Mirabal, J.M. Rapid bench-top fabrication of poly(dimethylsiloxane)/polystyrene microfluidic devices incorporating high-surface-area sensing electrodes. *Biomicrofluidics* **2015**, *9*, 026501, doi:10.1063/1.4918596.
16. Dittrich, P.S.; Manz, A. Lab-on-a-chip: Microfluidics in drug discovery. *Nat. Rev. Drug Discov.* **2006**, *5*, 210–218.
17. Eddings, M.A.; Johnson, M.A.; Gale, B.K. Determining the optimal PDMS–PDMS bonding technique for microfluidic devices. *J. Micromech. Microeng.* **2008**, *18*, 67001.
18. Faustino, V.; Catarino, S.O.; Lima, R.; Minas, G. Biomedical microfluidic devices by using low-cost fabrication techniques: A review. *J. Biomech.* **2016**, *49*, 2280–2292.
19. Pal, R.; Sung, K.E.; Burns, M.A. Microstencils for the patterning of nontraditional materials. *Langmuir* **2006**, *22*, 5392–5397.
20. Zhu, Y.; Moran-Mirabal, J. Highly bendable and stretchable electrodes based on micro/nanostructured gold films for flexible sensors and electronics. *Adv. Electron. Mater.* **2016**, *2*, 1500345.

21. Behl, M.; Lendlein, A. Shape-memory polymers. *Mater. Today* **2007**, *10*, 20–28.

22. Liu, C.; Qin, H.; Mather, P.T. Review of progress in shape-memory polymers. *J. Mater. Chem.* **2007**, *17*, 1543.

23. Cummins, G.; Desmulliez, M.P.Y. Inkjet printing of conductive materials: A review. *Circuit World* **2012**, *38*, 193–213.

24. Derby, B. Inkjet Printing of Functional and Structural Materials: Fluid Property Requirements, Feature Stability, and Resolution. *Annu. Rev. Mater. Res.* **2010**, *40*, 395–414.

25. Carrilho, E.; Martinez, A.W.; Whitesides, G.M. Understanding wax printing: A simple micropatterning process for paper-based microfluidics. *Anal. Chem.* **2009**, *81*, 7091–7095.

26. Martinez, A.W.; Phillips, S.T.; Whitesides, G.M.; Carrilho, E. Diagnostics for the developing world: Microfluidic paper-based analytical devices. *Anal. Chem.* **2010**, *82*, 3–10.

27. Dungchai, W.; Chailapakul, O.; Henry, C.S. Electrochemical detection for paper-based microfluidics. **2009**, *81*, 5821–5826.

28. Kitson, P.J.; Rosnes, M.H.; Sans, V.; Dragone, V.; Cronin, L. Configurable 3D-Printed millifluidic and microfluidic "lab on a chip" reactionware devices. *Lab Chip* **2012**, *12*, 3267.

29. Gross, B.C.; Erkal, J.L.; Lockwood, S.Y.; Chen, C.; Spence, D.M. Evaluation of 3D printing and its potential impact on biotechnology and the chemical sciences. *Anal. Chem.* **2014**, *86*, 3240–3253.

30. Gabardo, C.M.; Zhu, Y.; Soleymani, L.; Moran-Mirabal, J.M. Bench-top fabrication of hierarchically structured high-surface-area electrodes. *Adv. Funct. Mater.* **2013**, *23*, 3030–3039.

31. Fu, C.C.; Grimes, A.; Long, M.; Ferri, C.G.L.; Rich, B.D.; Ghosh, S.; Ghosh, S.; Lee, L.P.; Gopinathan, A.; Khine, M. Tunable nanowrinkles on shape memory polymer sheets. *Adv. Mater.* **2009**, *21*, 4472–4476.

32. Pegan, J.D.; Ho, A.Y.; Bachman, M.; Khine, M. Flexible shrink-induced high surface area electrodes for electrochemiluminescent sensing. *Lab Chip* **2013**, *13*, 4205–9.

33. Gabardo, C.M.; Yang, J.; Smith, N.J.; Adams-McGavin, R.C.; Soleymani, L. Programmable Wrinkling of Self-Assembled Nanoparticle Films on Shape Memory Polymers. *ACS Nano* **2016**, *10*, 8829–8836.

34. Bowden, N.; Brittain, S.; Evans, A.G.; Hutchinson, J.W.; Whitesides, G.M. Spontaneous formation of ordered structures in thin films of metals supported on an elastomeric polymer. *Nature* **1998**, *393*, 146–149.

35. Lacour, S.P.; Wagner, S.; Huang, Z.; Suo, Z. Stretchable gold conductors on elastomeric substrates. *Appl. Phys. Lett.* **2003**, *82*, 2404–2406.

36. Meng, Q.; Hu, J. A review of shape memory polymer composites and blends. *Compos. Part A Appl. Sci. Manuf.* **2009**, *40*, 1661–1672.

37. Woo, S.M.; Gabardo, C.M.; Soleymani, L. Prototyping of wrinkled nano-/microstructured electrodes for electrochemical DNA detection. *Anal. Chem.* **2014**, *86*, 12341–12347.

38. Gautam, M.; Jayatissa, A.H. Detection of organic vapors by graphene films functionalized with metallic nanoparticles. *J. Appl. Phys.* **2012**, *112*, doi:10.1063/1.4768724.

39. Steuwe, C.; Kaminski, C.F.; Baumberg, J.J.; Mahajan, S. Surface enhanced coherent anti-stokes Raman scattering on nanostructured gold surfaces. *Nano Lett.* **2011**, *11*, 5339–5343.

40. Zhang, L.; Lang, X.; Hirata, A.; Chen, M. Wrinkled nanoporous gold films with ultrahigh surface-enhanced raman scattering enhancement. *ACS Nano* **2011**, *5*, 4407–4413.

41. Lu, H.; Koo, L.Y.; Wang, W.M.; Lauffenburger, D.A.; Griffith, L.G.; Jensen, K.F. Microfluidic Shear Device for Quantitative Analysis of Cell Adhesion. *Anal. Chem.* **2004**, *76*, 5257–5264.

SUPPLEMENTARY INFORMATION

Bench-top fabrication of an all-PDMS microfluidic electrochemical cell sensor integrating micro/nanostructured electrodes

Sokunthearath Saem, Yujie Zhu, Helen Luu, and Jose M. Moran-Mirabal*

Department of Chemistry and Chemical Biology, McMaster University, 1280 Main Street West, Hamilton, ON, L8S 4M1, Canada

* Correspondence: mirabj@mcmaster.ca; Tel.: +1-905-525-9140

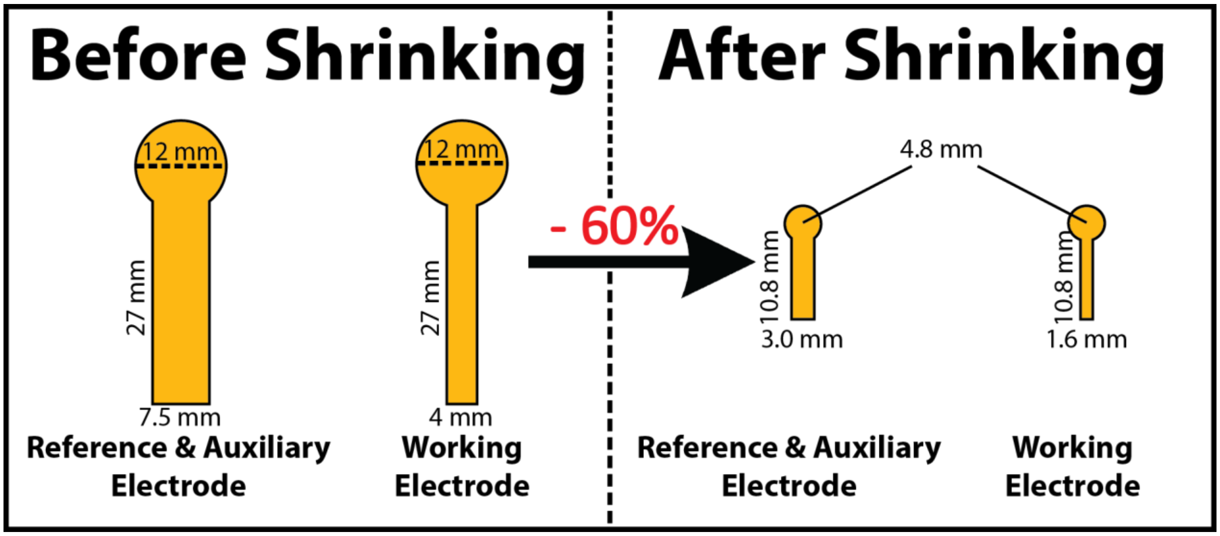

Figure 2.S1. Schematic of the dimension of the electrodes used in the microfluidic device. On the left shows the relative size comparison of the electrodes prior to shrinking to after shrinking (right).

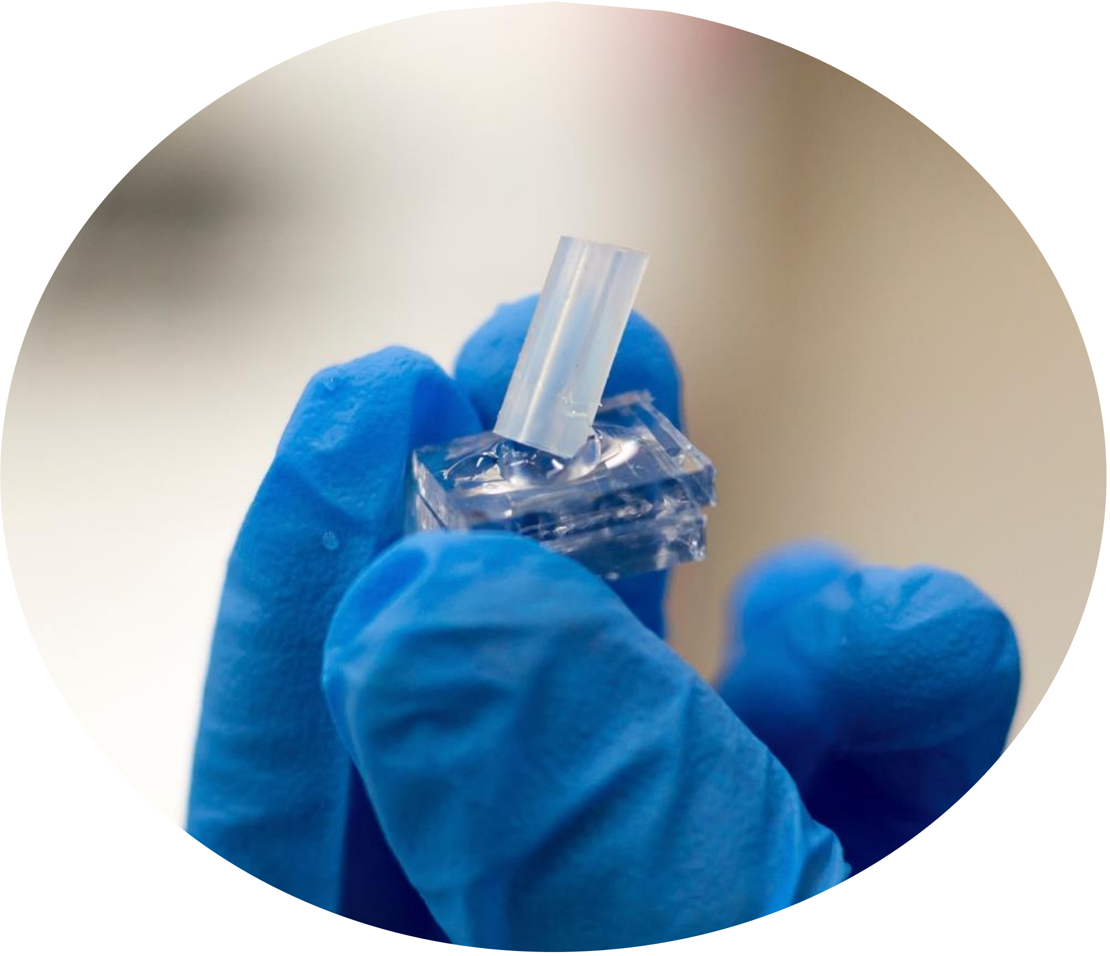

Figure 2.S2. Image of a broken dead-end μF device following the burst pressure test.

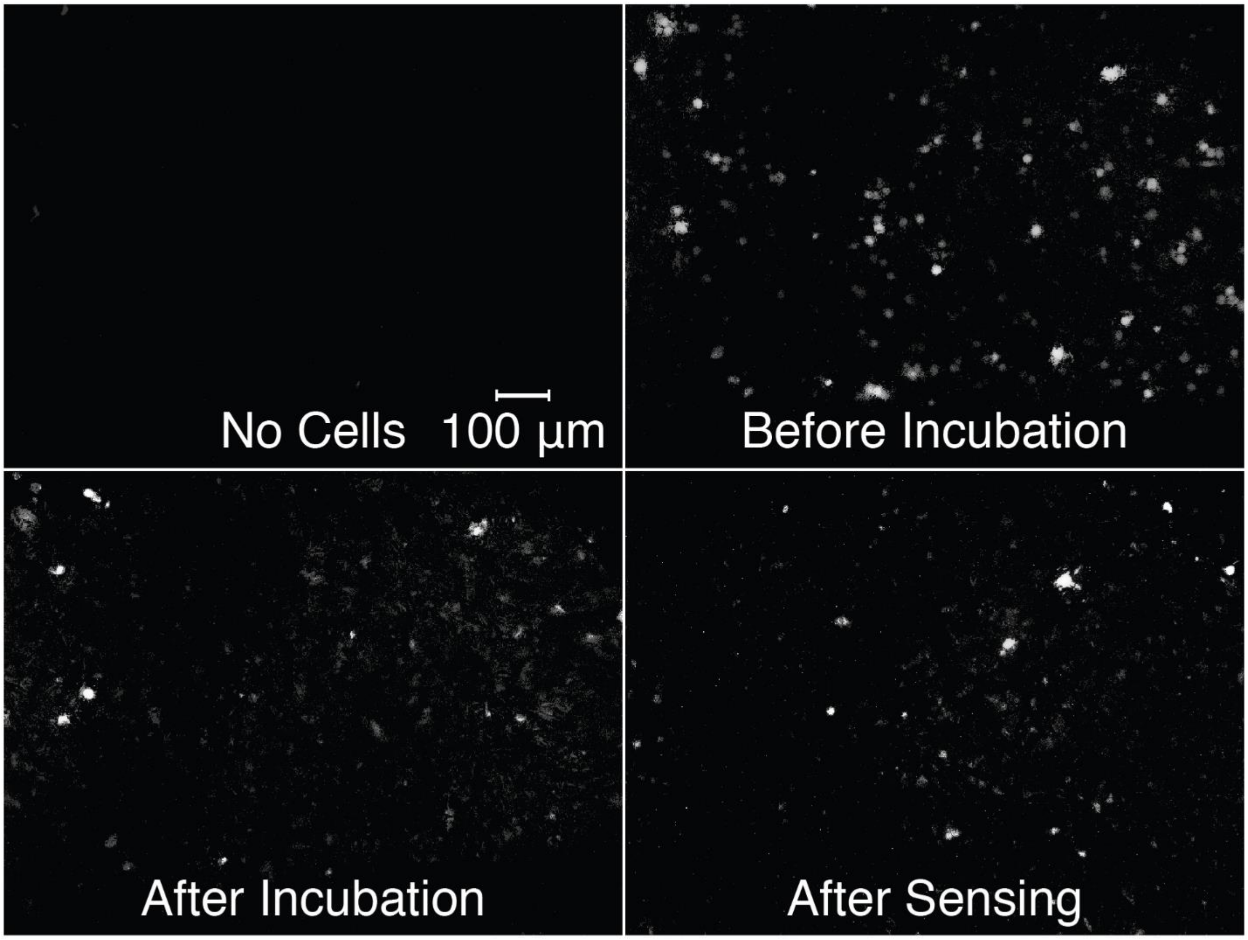

Figure 2.S3. Fluorescence microscope images of the working electrode inside the μF device at different stages of the cell adhesion process compared to the blank electrode (top left). Images were taken of different areas of the electrode. All images were taken at 10x magnification and with identical illumination and acquisition conditions. Bright circular areas represent CFSE labelled cells.

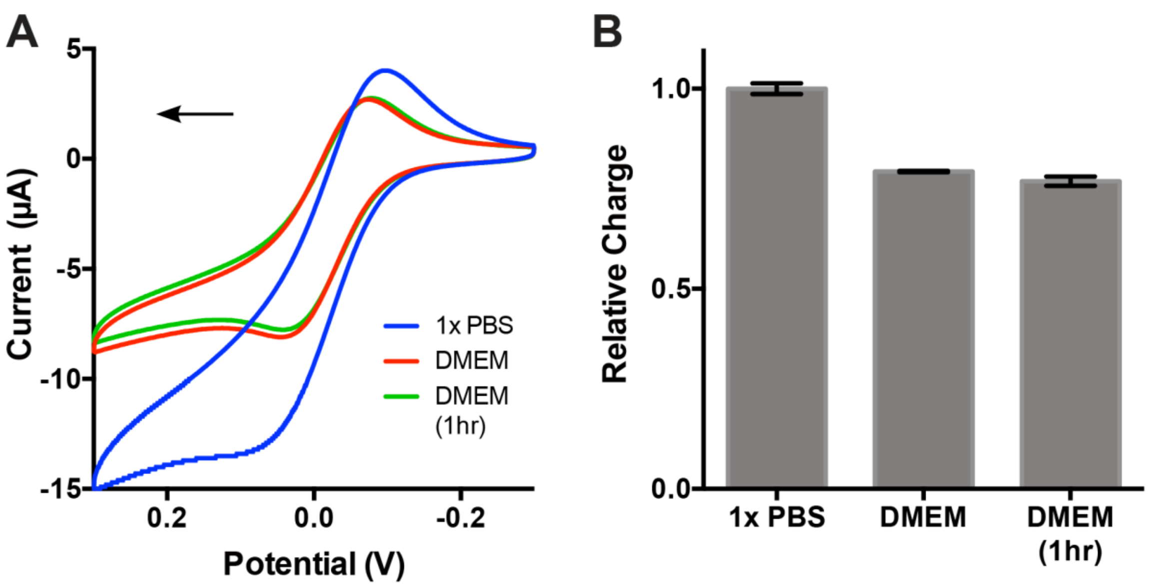

Figure 2.S4. Cyclic voltammogram and relative charge plot comparing electrochemical signals during sensing in 5 mM $K_4[Fe(CN)_6]$ solutions of 1x PBS, DMEM, and DMEM after 1 hour incubation at cell adhesion conditions (37°C and 5% CO_2). **(A)** Overlaid cyclic voltammograms of different control conditions with a positive initial sweep direction as indicated by the arrow. **(B)** Plot comparing relative charge transferred in each condition (normalized to PBS) showing that there is no influence of DMEM on the electrochemical signal before and after 1-hour of incubation. Thus, all electrochemical changes observed during sensing can be attributed to fibroblast cell adhesion.

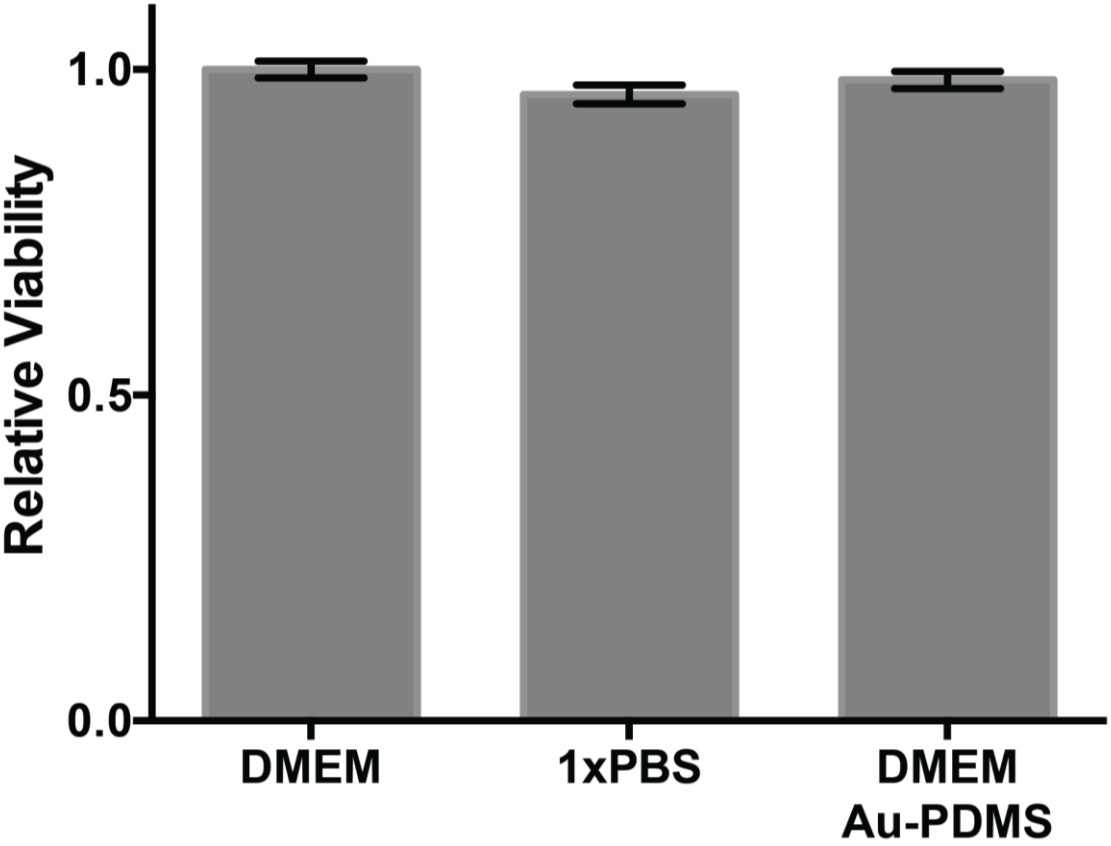

Figure 2.S5. Plot of 3T3 murine fibroblast cells relative viability in 1xPBS, DMEM, and with the Au-PDMS electrode in DMEM. The results show no quantitative difference to cell viability between the different storage conditions.

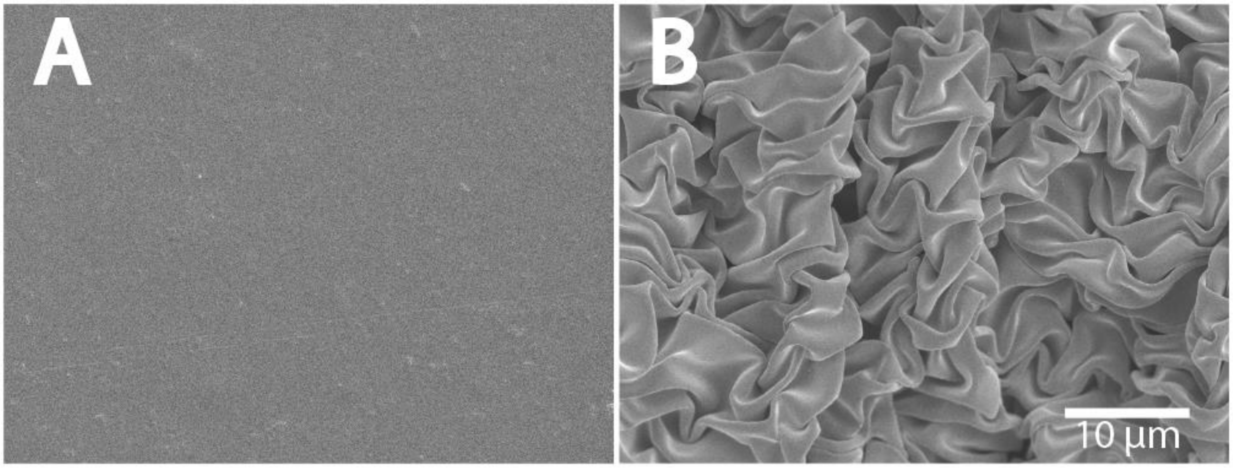

Figure 2.S6. SEM image of gold films before **(A)** and after **(B)** shrinking.

Video S1. Video of how the dead-end burst pressure test was performed inside a beaker of water. The dead-end channel was pressurized by N_2 gas and the pressure was monitored until the point of failure.

Video S2. Video demonstrating the laminar flow capability of the µF device in separating the working (red) and reference (green) solutions with food colouring. In this video, the solutions were pumped through the µF device at a flow rate of 0.20 mL/min.

Chapter 3: Microstructured Anodes by Surface Wrinkling for Studies of Direct Electron Transfer Biofilms in Microbial Fuel Cells

This chapter was originally published as:

Mehran Abbaszadeh Amirdehi,[ξ] Sokunthearath Saem,[ξ] Mir Pouyan Zarabadi, Jose M. Moran-Mirabal,* and Jesse Greener.* (2018) Microstructured anodes by surface wrinkling for studies of direct electron transfer biofilms in microbial fuel cells. *Advanced Materials Interfaces*. **5**: 1800290.

[ξ]Sokunthearath Saem and Mehran Abbaszadeh Amirdehi contributed equally to the work.

and has been reprinted with permission from Advanced Materials Interfaces.

Author Contributions: SS, JMM, and JG planned the study. SS fabricated the electrode chips, performed electrochemical characterization, thickness measurement, and SEM. MAA and MPZ cultured the bacteria and performed the microbial fuel cell characterization.

Microstructured Anodes by Surface Wrinkling for Studies of Direct Electron Transfer Biofilms in Microbial Fuel Cells

Mehran Abbaszadeh Amirdehi, Sokunthearath Saem, Mir Pouyan Zarabadi, Jose M. Moran-Mirabal, and Jesse Greener**

M. Abbaszadeh Amirdehi, M. P. Zarabadi, Prof. J. Greener

Département de Chimie Université Laval Québec, QC G1V 0A6, Canada

E-mail: jesse.greener@chm.ulaval.ca

S. Saem, Prof. J. M. Moran-Mirabal

Department of Chemistry and Chemical Biology McMaster University 1280 Main Street West, Hamilton, ON L8S 4M1, Canada

E-mail: moran-mirabal@mcmaster.ca

Prof. J. Greener CHU de Québec Centre de recherche Centre Université Laval

10 rue de l'Espinay, Québec, QC G1L 3L5, Canada

ABSTRACT

A method for producing hierarchical wrinkled gold surfaces is used to continuously change characteristic microstructure dimensions of a bioanode in a microbial fuel cell, while conserving the total electroactive surface area and material chemistry. Using this approach, the effect of anode topography on power outputs from direct electron transfer from Geobacter sulfurreducens biofilms can be isolated and studied without the competing effects associated with additive manufacturing. Despite having the same electroactive surface area for all structured anodes, tall and well-spaced features perform best. Anodes with the shortest, most closely packed structures, on the other hand, do not perform any better than planar surfaces with the same footprint and lower electroactive surface area. It is postulated that large interfold spacing provides better electrical contact between the biofilm and the electrode via improved

bacterial packing density at the electrode surface. Rigorous attention to structural dimensions rather than total electroactive surface area is proposed as an important direction for future bioanode optimization in microbial fuel cells containing direct electron transfer electroactive biofilms.

3.1. INTRODUCTION

A microbial fuel cell (MFC) is a bioelectrochemical device in which the oxidation of organic molecules produces a usable electric current. MFCs are promising as next generation clean energy technologies because they can produce electricity while achieving bioremediation.[1–5] In addition, they show potential as autonomous power sources for remote environmental sensing applications[6] and even for implanted devices.[7] The electroactive biofilms (EABs), which catalyze the oxidation reaction, are composed of microorganisms that can transfer electrons to extracellular acceptors.[8] In a MFC, EABs are cultured directly on the anode so that electron transfer to an external circuit is efficient. Common bacteria used as EABs include *Geobacter sulfurreducens,*[9] *Shewanella putrefaciens*,[10] *Desulfovibrio desulfuricans,*[11] and *Rhodopseudomonas palustris.*[12] Biofilms from these bacteria benefit from the ability to directly transfer electrons through a bioconductive network of bacterial appendages and embedded electroactive proteins, via physical contact with the anode.[13–15] To enhance MFC performance, high-surface-area anodes have been introduced based on nanoconductive textiles,[16] graphene sponges,[17] and brushes.[18] In other approaches, additive fabrication methods been used to decorate existing anode surfaces with conductive polymers[19] and nanoparticles of different materials, sizes, and shapes.[20–23] Generally, structured anodes are designed to increase the total surface area, but little effort has been made to isolate and rigorously study the role of surface topography. This is likely because it is difficult to vary feature geometries in a controlled manner, without introducing competing effects such as changes in total surface area, exposed materials or surface chemistry.

Gold is an excellent anode material because it is highly conductive, biocompatible, and electrochemically stable over a wide potential window.[14,24–27] Recently, a benchtop process has been developed for the controlled buckling of thin gold films on top of shape-memory polymer sheets, with demonstrated applications in point-of-care diagnostic systems.[28–31] As opposed to other approaches, this method produces chemically homogeneous surface structures (wrinkles) with continuous control over average peak-to-valley heights and distances between folds, based on the initial gold film thickness. The method also conserves the total surface area, making it ideal for investigating the effect of anode topography on MFC performance, without introducing side-effects. In this work, we have used these surfaces as anodes for *G. sulfurreducens* biofilms in an H-type dual chamber MFC setup. Variations in wrinkle morphologies were achieved using Au layers with thicknesses between 50 and 400 nm, the largest range reported to date. Despite all wrinkled surfaces having the same enhancements to total exposed surface per geometrical area compared to control planar anodes, power density strongly depended on wrinkled surface morphology. Tall, widely spaced structures generated nearly twice the power output compared to planar anodes. However, no performance improvements were observed for wrinkled surfaces with small closely spaced structures. These results were likely due to improved bacterial packing efficiencies at the gold surface for widely spaced, or "open," wrinkle morphologies. We propose that these findings can guide the optimization of MFCs and other bioelectrochemical systems using direct electron transfer EABs by focusing on their physical access to the anode surface, in addition to increased electroactive surface area relative to the electrode geometrical footprint.

3.2. RESULTS AND DISCUSSION

3.2.1. Fabrication and Evaluation of Anode Surface

The structured anodes were fabricated using a benchtop method, in which gold electrodes were patterned through a self-adhesive stencil followed by shrinking of the pre-stressed polystyrene substrate (Figure 3.1). Pre-stressed polystyrene disks and the stencils were patterned using xurography.[31] The stencils were adhered to the pre-stressed polystyrene (PS) substrate and used to define the electrode shapes during the gold film sputtering. Individual square masks were used to selectively shield some of the sensing pads during the successive gold deposition cycles. This allowed us to produce sensing pads with final thicknesses of 50, 100, 200, and 400 nm (Figure 3.1, shades of orange) on a single chip. Then, the stencil was peeled from the substrate, revealing 4 sets of 4 patterned electrodes with the targeted film thicknesses. The substrates were subsequently heated at 165 °C, which caused the polystyrene substrate to shrink and introduced the compressive stress that resulted in wrinkling of the gold film. The different electrode film thicknesses were used to tune the wrinkled electrode topography from the nanometer to the micrometer range. Using these simple and inexpensive methods, devices were fabricated containing sets of sensing electrode pads with identical surface (≈0.8 cm2, corresponding to the flat gold film) and geometrical area (≈0.13 cm2 after shrinking), but different surface topographies that could be assayed in a single parallel experiment.

The surface topography of the shrunken Au films was quantified by optical profilometry (for surface roughness) and scanning electron microscopy (SEM) (for wrinkle spacing). First, it was noted that the polystyrene before and after shrinking (Figure 3.2A) and the unshrunken gold films (Figure 3.2B) showed smooth surfaces. By contrast, wrinkles formed upon shrinking polystyrene substrates with Au films. Wrinkle dimensions of interest included the root mean square (RMS) roughness (calculated as the root mean square of the peak and valley amplitudes, A, of the structured surfaces), and wrinkle spacing (approximated by the persistence length L), and their relation to Au film thickness (t). The relevant dimensions are shown schematically (Figure 3.2C), and by SEM imaging of a cross-section of a wrinkled surface after focused ion beam milling (FIB) milling (Figure 3.2D). Qualitative analysis of the electron micrographs showed a progression of wrinkle spacing from sub-micrometer for 50 nm thick Au films, to tens of micrometers for 400 nm thick films (Figure 3.2E–H), with a concomitant increase in wrinkle amplitude. Our observations are consistent with reported trends,[31] and demonstrate that the structured surfaces are a direct result of the compressive stress generated by the polystyrene during shrinking, where the elastic modulus mismatch between the substrate and the gold film causes the latter to buckle and wrinkle.

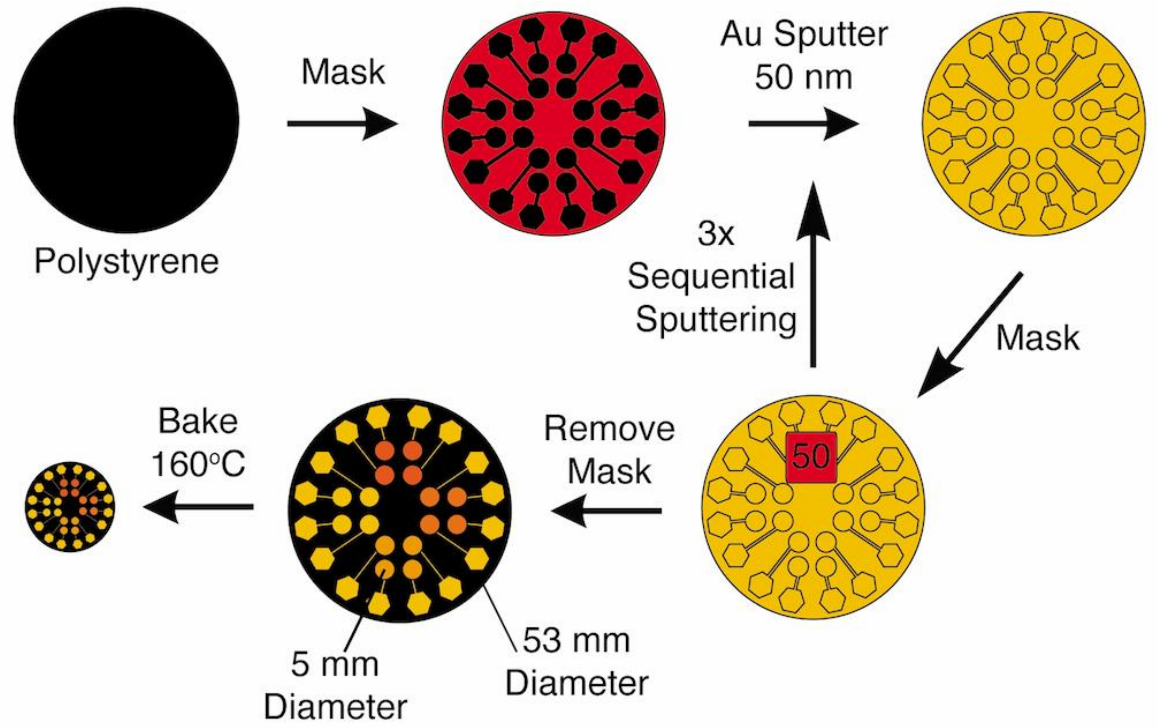

Figure 3.1. Schematic of fabrication process for generating 2 mm diameter wrinkled electrodes. Prestressed polystyrene disks (black) were cut from commercially available sheets. An adhesive vinyl stencil mask (red) was designed, patterned, and adhered to the polystyrene substrates. The sensing electrode pads were masked during the sequential sputtering of gold films, which resulted in sensing electrodes with thicknesses of 50, 100, 200, and 400 nm (shades of orange). The adhesive vinyl mask was removed and the substrates were shrunk at 165 °C. The final area of the substrate was 16% of the original area, and the final diameter of each sensing electrode pad was 2.0 mm (60% reduction in *x* and *y* dimensions).

Topographical maps obtained using optical profilometry allowed us to quantify the RMS roughness as a representative measurement of the surface topography. Figure 3.3A compares the measured RMS roughness for films before (cyan) and after (red) shrinking for the different thicknesses tested. While the RMS roughness for all gold film thicknesses tested was similar (≈15 nm) before shrinking, after shrinking the amplitude and roughness of the films increased with increasing film thickness. In addition, from a 2D fast Fourier transform analysis of the SEM surfaces, the persistence length (~*L*) was calculated.[32] Figure 3.3B shows that the persistence length varied linearly with initial Au film thickness. The RMS roughness and persistence length are relevant parameters for the growth of EABs since the topographical features can directly impact the bacteria's ability to access the anode surface, especially in the valleys formed between wrinkles, which could affect the efficiency with which charge transferred to the electrode.

Finally, the electroactive surface area of the structured electrodes was assessed through cyclic voltammetry. Figure 3.3C shows a side-by-side comparison of the voltammograms produced by flat and structured electrodes with a 2 mm diameter footprint. As anticipated, the structured electrode presented a higher charge transfer profile than the flat electrode. Integration of the area under the cathodic peak of the voltammogram yielded the total charge transferred during the voltage sweep, which could be used to calculate the electroactive surface area (cf. Experimental Section). A comparison of the electroactive surface area (Figure 3.3D) showed that, within measurement error, all the structured electrodes, regardless of topographical feature dimensions, exhibited a similar increase to electroactive surface area (>600%) compared to a flat electrode with a similar geometrical footprint. Thus, by using this benchtop fabrication method, we could tune the anode surface topography without changing overall footprint or introducing changes to the electroactive surface area or material homogeneity. In this way, efficiencies in the total current collected from an EAB could be studied as a function of topography without incurring common side-effects of other additive fabrication techniques that could obscure these effects.

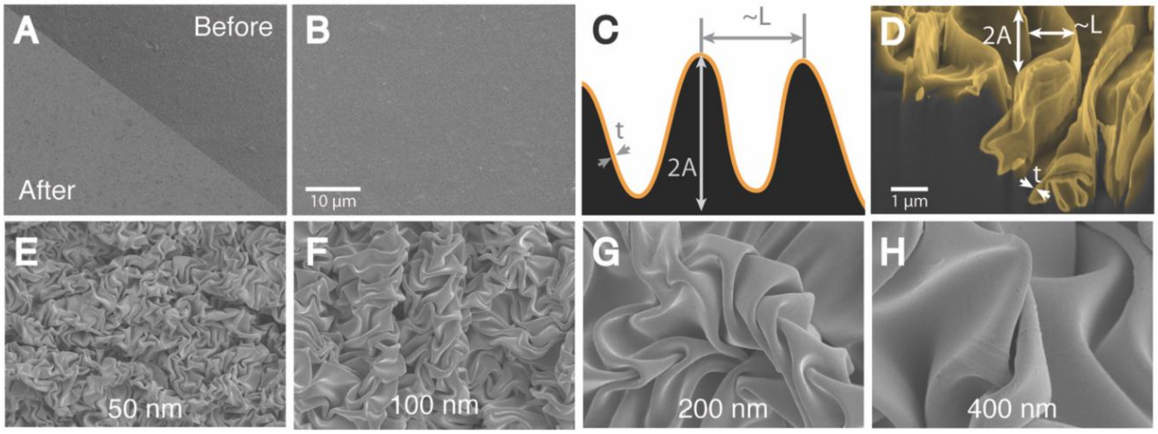

Figure 3.2. Characterization of structured Au electrodes through electron microscopy. SEM images of **(A)** polystyrene before and after shrinking, **(B)** flat Au sputtered on polystyrene. **(C)** Cross-section schematic of the electrode surface after structuring, showing the PS substrate (black) coated by a gold film (yellow) with thickness *t*. The wrinkles are characterized by an amplitude *A* and a periodicity that is approximated by the persistence length *L*. **(D)** SEM image of the cross-section of a 50 nm thick structured film, after focused ion beam milling. Representative amplitude, periodicity and thickness of the wrinkled film are highlighted in the image. The image has been false colored to aid in the identification of the gold film (yellow) and the polymer substrate (gray). Top-down SEM images for wrinkled Au electrode surfaces for film thicknesses of **(E)** 50, **(F)** 100, **(G)** 200, and **(H)** 400 nm. Images **(A)**, **(B)**, and **(E)–(H)** are all presented at the same scale.

3.2.2. Measurements in Microbial Fuel Cells

Next, we examined the performance of wrinkled gold electrodes as anodes for MFC applications using the setup shown in Figure 3.4A. We conducted parallel experiments using five separate glass MFCs, which were all inoculated simultaneously with *G. sulfurreducens* bacteria from the same preculture. Each parallel experiment was repeated three times. In four of the MFCs, the anode consisted of a 2 × 2 wrinkled anode array based on an initial Au layer thicknesses: 50, 100, 200, and 400 nm. The last MFC contained the planar Au anode array as a control. In all cases, a graphite cathode measuring 25 × 25 × 3 mm was immersed in a phosphate buffer saline (PBS) solution containing potassium ferricyanide (30 × 10−3 m).

First, we confirmed EAB growth on wrinkled and planar Au anodes by SEM and resonance Raman spectroscopy. Results presented in Figure 3.4 were obtained from 400 nm thick wrinkled gold anodes, but similar results were observed for all thicknesses. Wrinkled and planar Au surfaces were immersed in the anolyte, but not electrically connected to the external circuit. After careful analysis of the SEM images similar to Figure 3.4B, we observed no evidence of bacterial attachment or biofilm production. This was because electrically isolated wrinkled Au surfaces could not serve as electron sinks, thereby preventing electrode respiration of the EAB. After use as electrically connected anodes, SEM images similar to Figure 3.4C revealed that dense biofilm layers blanketed the anodes, hiding the wrinkled surface, and demonstrating good biocompatibility and biofilm growth. We also verified the growth of *G. sulfurreducens* biofilms via resonance Raman spectroscopy which produced cytochrome fingerprints at 1316, 1367, 1589, and 1640 cm^{-1} (Figure 3.4D).[33] In comparison, a broad featureless background was observed before Au surfaces were connected as MFC anodes through an external resistor even if they had been previously immersed in the anolyte.

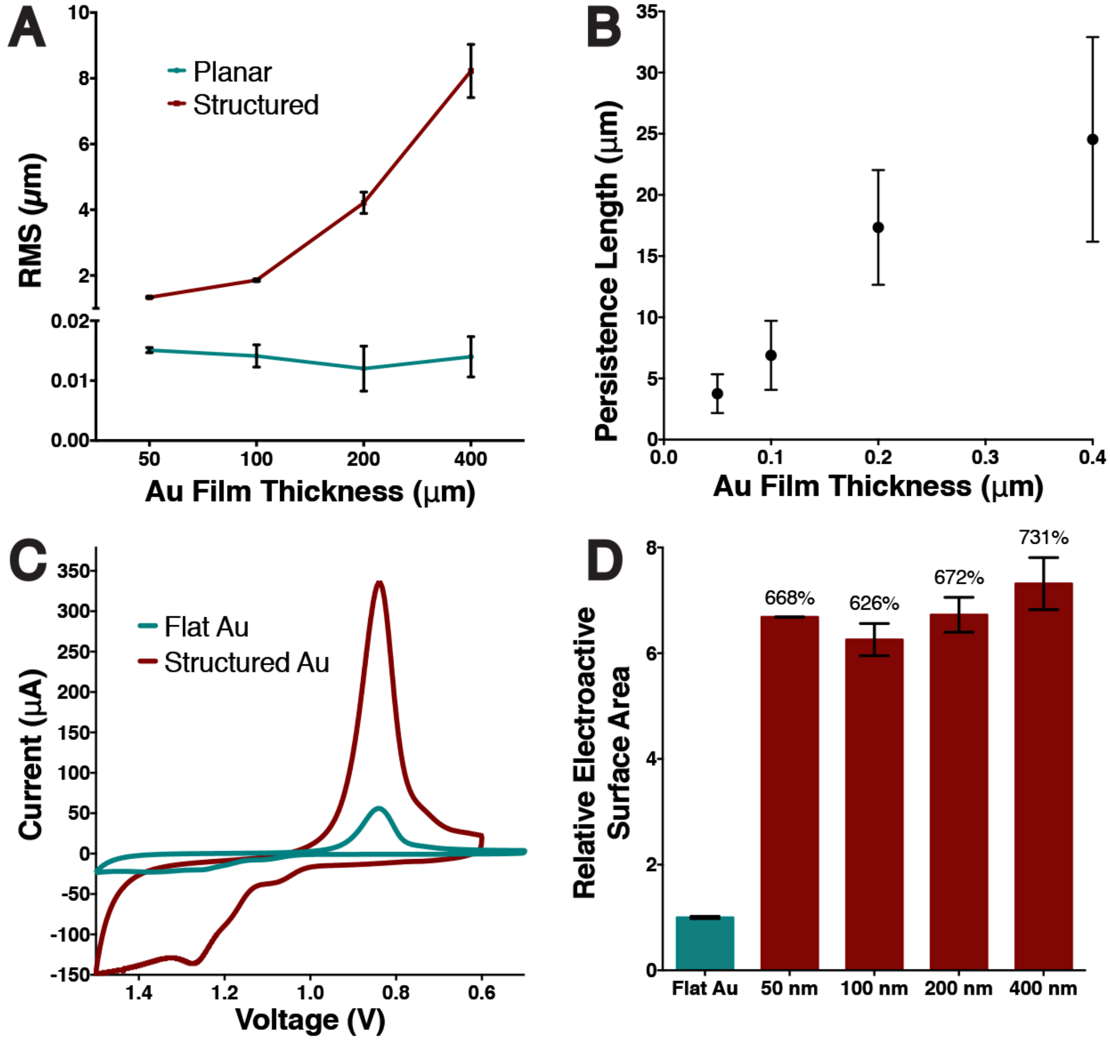

Figure 3.3. Topographical and electrochemical characterization of the structured electrodes. **(A)** RMS surface roughness measurements obtained by optical profilometry for Au films of different thicknesses before (cyan) and after (red) wrinkling. **(B)** Persistence length for the wrinkled surfaces as a function of gold film thickness. **(C)** Typical cyclic voltammogram obtained in a 100 × 10−3 m H2SO4 redox solution using a gold working electrode with a 2 mm diameter footprint before (cyan) and after (red) wrinkling, show the enhanced charge transfer due to the increased surface area. **(D)** The relative electroactive surface area (normalized to that of a flat electrode with a 2 mm diameter footprint) for planar (cyan) and wrinkled (red) electrodes. All error bars represent the standard deviation of measurements made on $n > 3$ replicate electrodes.

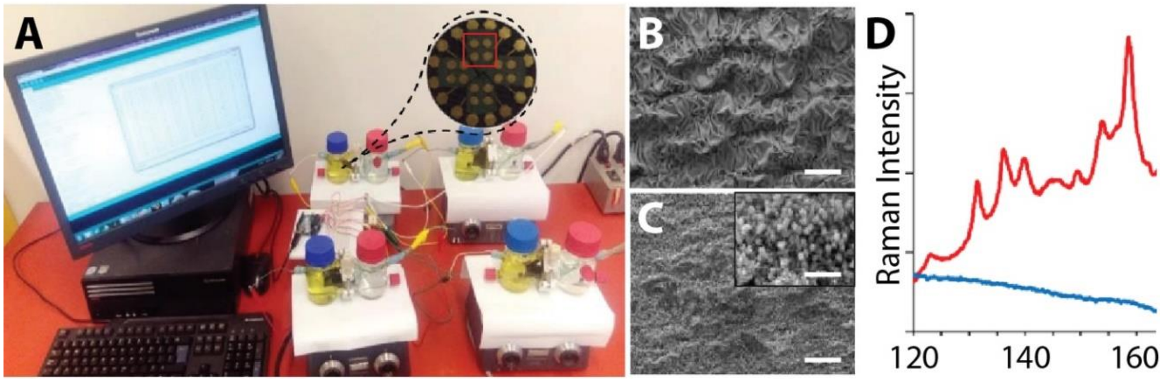

Figure 3.4. (A) A picture of 4 two-chamber microbial fuel cells with catholyte (yellow) and anolyte (colourless) reservoirs on stir plates. The fifth control MFC is not shown. Inset shows an active 2 × 2 anode array (highlighted). Not shown in the inset are the protected connections made to each active anode array. All MFCs were connected to a breadboard across *R*ext. A microcontroller measured *V* across *R*ext and stored data on a computer. SEM images of **(B)** a clean wrinkled anode before cathode connection through *R*ext and **(C)** a biofilm covered anode after cathode connection through *R*ext. The inset shows magnified region in (ii) showing individual bacteria and EPS. Scale bars are 100 μm (i and ii) and 15 μm (inset). **(D)** Spectra from resonance Raman spectroscopy of wrinkled anodes formed from Au layers of 400 nm thickness, before (blue) and after experiment was complete (red).

To compare the effect of anode topography on MFC startup, we monitored voltage outputs in time during the initial growth phase. Starting immediately after inoculation, the voltages were measured across *R*ext at 10 min intervals for all MFCs and current was calculated via directly from Ohm's law. For all MFCs, voltage (and current) increased rapidly during the first 35 h. Figure 3.5 shows average growth curves from three replicate MFC start cycles for control and all wrinkled anode arrays used here. Lower lag time, slightly higher average currents and voltages (*V*ave) were observed for wrinkled anodes compared to the control surfaces. However, based on their standard deviations (*V*STD), they were not statistically different. Therefore, we concluded that the degree of anode wrinkling did not have a significant effect on the rate of bacterial colonization and initial growth. After 35 h, MFC voltage outputs began to plateau for all experiments in the range of 0.3–0.6 V. Based on the calculated coefficient of variance (CV) for voltage (CV = *V*STD/*V*Ave) for all like anodes, MFC outputs with like anodes also began to stabilize as the biofilm entered maturity.

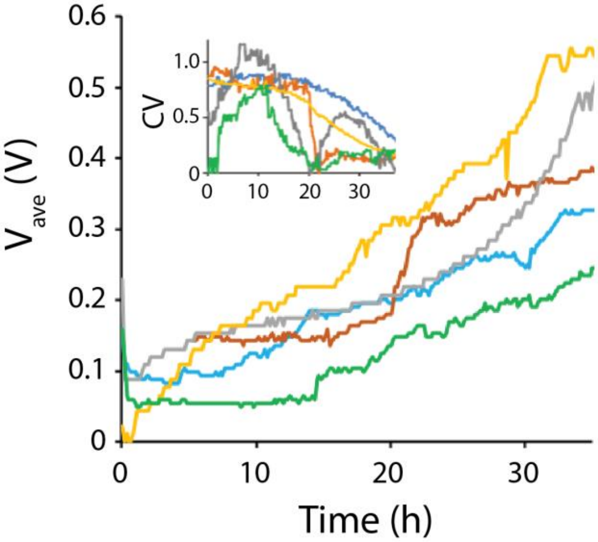

Figure 3.5. The average voltage and current versus time during start up for anodes used in this study. All measurements were conducted across a 100 kΩ external resistor. Current and voltage resolution were 100 nA and 10 mV, respectively. Inset shows the coefficient of variance (CV) based on average voltage (*V*ave) and their standard deviations (*V*STD). In all cases color coding follows: 50 nm (blue), 100 nm (orange), 200 nm (gray), 400 nm (yellow), and planar (control) anodes (green).

Power density curves were acquired from polarization measurements after ≈3 d, when MFCs had reached stable operating conditions. Stability was determined by CV < 0.2 in *V*ave. Following other published approaches to observe the impact of electrode structuration on MFC power outputs, we obtained power density measurements during operation.[21,34–36] As an example, three data sets showing power density and polarization curves are given in Figure 3.6A for MFCs containing wrinkled anodes made from 400 and 50 nm Au layers and from planar control anodes (with resulting RMS roughness and persistence lengths given in Figure 3.3). It can be seen that both *P*max and the maximum current density were largest for wrinkled anodes made from 400 nm Au layers (>400 mW m−2 and 1 A m−2, respectively).

On the other hand, these values were both smaller and statistically equal for the control and the 50 nm wrinkled anodes.

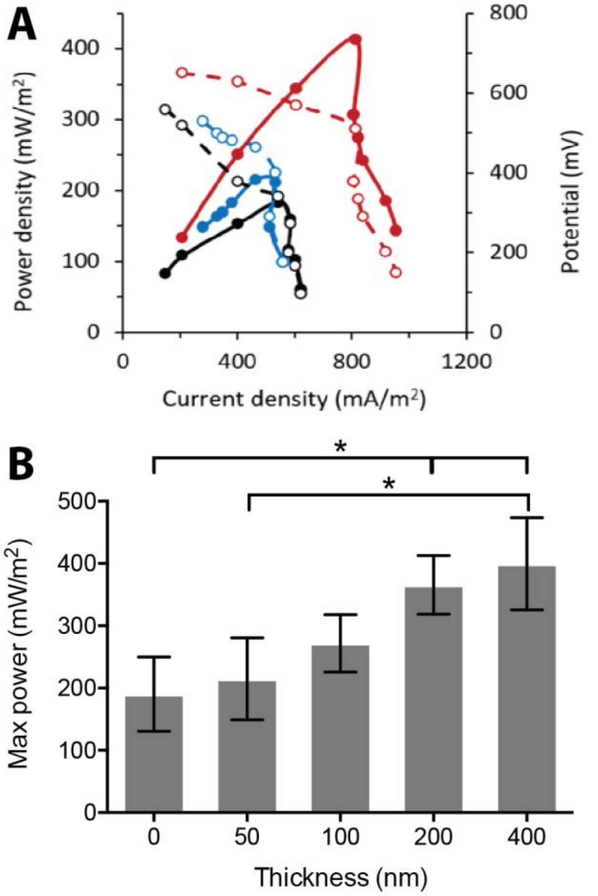

Figure 3.6. (A) Example of individual polarization (dashed) and power density (solid) curves acquired from separate samples grown on control (black), 200 (blue), and 400 (red) nm wrinkled electrodes. **(B)** Average of maximum power density as read from at least three separate power density curves for each electrode type. All power density curves were obtained from separate samples after 60 h of growth. The voltage V, the current I, and the power $P = VI$ are obtained by varying the resistance R.

Figure 3.6B shows the average Pmax from three independent measurements for each anode type. It was seen that Pmax increased for wrinkled anodes made from thicker Au layers. The wrinkled surfaces formed from 400 nm thick Au films had values of Pmax more than twice as large compared to unstructured gold anodes. A pairwise one-way ANOVA comparison showed statistical differences (95% confidence) between unstructured from 200 and 400 nm thick Au films. A significant difference of *P*max between wrinkled anodes made from 400 and 50 nm thick Au films was also observed. This was somewhat surprising since the total electroactive surface area was the same for both wrinkled anodes. Moreover, there were no significant differences in *P*max between the wrinkled anodes made from 50 nm thick Au films and the flat controls. Clearly, the enhanced anode electroactive surface area, which was ≈6 times larger than control for all wrinkled surfaces, did not benefit power outputs to the same degree.

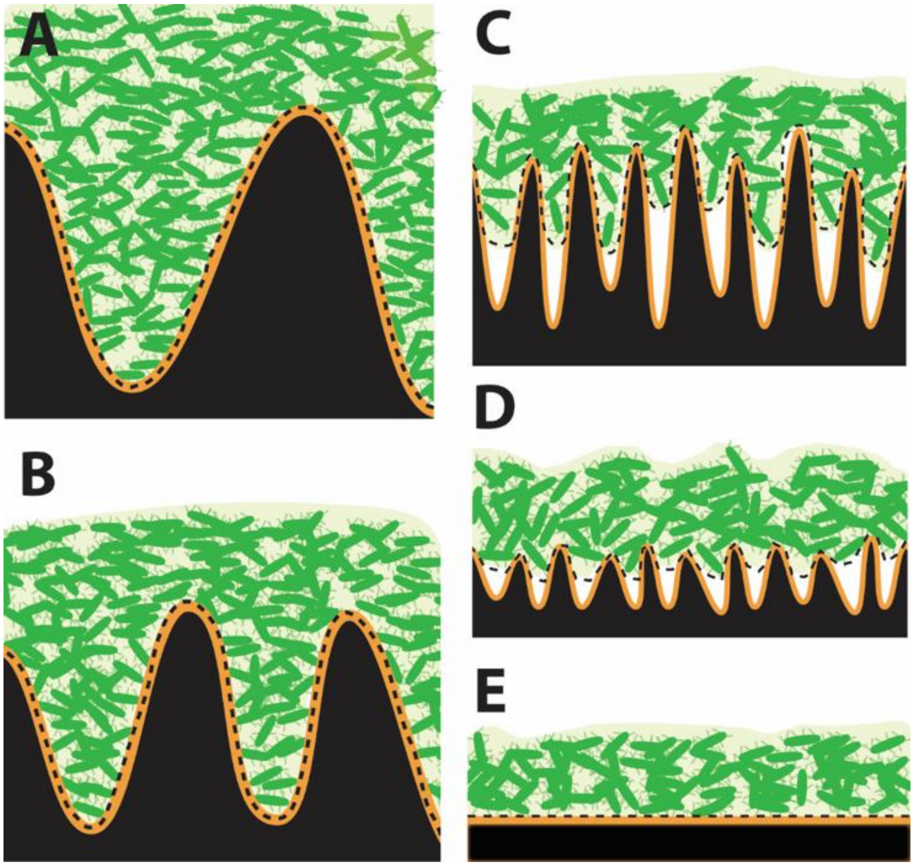

Figure 3.7. Conceptual model of the *G. sulfurreducens* biofilm (green) at a wrinkled anode surfaces (gold) used in this study. The anode surfaces were generated by Au films of **(A)** 400, **(B)** 200, **(C)** 100, **(D)** 50 nm thickness, and **(E)** unshrunken films. Upper bacterial layers are not shown.

In evaluating the origin of microstructure-based enhancements to *P*max, we assumed that the thickness of the Au layers were not specifically responsible. Therefore, the key to exploiting enhanced electroactive surface area for microstructured anodes for direct electron transfer EABs should be related to their morphology. Since the Au layer thickness had a deterministic effect on both the RMS roughness (feature height) and persistence length (interstitial distance between features), as seen in Figure 3.3A,D, the changes in performance were assumed to be related to these parameters. Figure 3.7 shows nearly to scale renderings vis-à-vis bacteria size and the wrinkle dimensions. As the persistence length was reduced for thinner Au layers, randomly oriented bacteria could jam between the folds. This resulted in inaccessible domains within the valley portions, thereby reducing direct bacterial access to portions of the anode surface. A dashed line highlights the biointerface boundary where bacteria at the lowest biofilm layer could directly touch some portion of the anode surface. It shows the development of a progressive mismatch between the biointerface and the anode surface as persistence length was decreased. For wrinkled surfaces formed from 50 nm thick Au films, the biointerface became nearly flat, which would explain the similar *P*max compared to the control anodes. On the other hand, Biointerfaces nearly conformed to the entirety of the wrinkled surface area for those anodes formed from 200 and 400 nm thick Au films. In practical terms, a larger biointerface area means more bacteria in contact with the anode. Considering bacteria as parallel resistors, this can be understood to decrease charge transfer resistance.[37–40] In this context, it can be seen that maximizing microfeature density as a route to increasing electroactive surface area, may actually reduce MFC performance due to reductions in interfeature spacing.

To our knowledge, this is the first literature example of wrinkled Au surfaces fabricated from films with thicknesses >200 nm. However, future experiments may be designed to further extend the thickness of the initial Au layers. This could result in differential effects in terms of persistence length and height because, increases to the former should not result in further improvements to bacterial surface density after complete surface coverage is achieved. Thus, changes to performance beyond this point could be to be correlated to height only. In addition, follow up work can investigate the long-term behavior of the wrinkled bioanodes in terms of their voltage and power generation.[41,42]

3.3. CONCLUSIONS

Wrinkled gold films were used for the first time as structured anodes for microbial fuel cells. The approach of structuring gold films by the thermal shrinking of a prestressed polymer support substrate produced structures with tunable wrinkle height and spacing in range of the <1–8 μm, and 4–25 μm, respectively. Because the exposed surface area and material homogeneity were maintained between the samples, the effect of surface topography on MFC power could be investigated without interference from competing effects introduced by additive anode fabrication techniques. It was determined that the anodes with tall, well-spaced features performed best. It is proposed that large interfold spacing resulted in better bacterial packing efficiencies at the biointerface, resulting in enhanced current collection efficiencies. This work opens the way for future experiments that focus on the effect of anode structure dimensionality, rather than on total electroactive surface area. The approach can be beneficial for applications involving any direct electron transfer systems, including, but not limited to microbial fuel cells.

3.4. EXPERIMENTAL SECTION

Structured Anode Fabrication: PS sheets (Graphix Shrink Film, Graphix, Maple Heights, OH, USA) were cleaned in successive baths of isopropyl alcohol, ethanol, and water, and cut into 53 mm diameter disks using a computer-driven blade cutter (Robo Pro CE5000-40-CRP, Graphtec America Inc., Irvine, CA, USA). Self-adhesive vinyl sheets (FDC-4300, FDC graphic films, South Bend, IN, USA) were patterned using the blade cutter into stencils describing the shape of the electrodes and adhered to the polystyrene substrates. Gold was then deposited from a 99.999% purity gold target (LTS Chemical Inc., Chestnut Ridge, NY, USA) using a Torr Compact Research Coater CRC-600 manual planar magnetron sputtering system (New Windsor, NY, USA) onto the masked polystyrene surface. Successive sputtering depositions were performed, with certain electrodes being masked with adhesive vinyl to produce sensing pads consisting of gold films of 50, 100, 200, and 400 nm thickness. After removing the vinyl masks, the polystyrene films containing the patterned gold electrodes were shrunk at 165 °C in a temperature controlled vacuum oven (Isotemp, Fisher Scientific, Ottawa, ON, Canada), on aluminum weighing dishes lined with parchment paper. The final diameter of the individual electrodes after shrinking was ≈2 mm.

MFC Construction and Operation: Dual-chamber glass MFCs with 150 mL capacity were used in this study (MFC 100.25.2, Adams & Chittenden Scientific Glass, NY, USA). Each chamber was joined by a 31 mm diameter glass bridge using a clamp. A cation exchange membrane (CEM) (CMI-7000S, Membrane International Inc., NJ, USA) was immobilized between the two glass bridges. The CEM was pretreated by successive exposure to deionized (DI) water with 5 wt% NaCl (Caledon Lab Ltd., ON, Canada) for 12–18 h, followed by thorough washing with DI water. Each compartment had two feedthrough ports, one with a large (22 mm) diameter, for inserting the electrode, and a second with a small (8 mm) diameter used as a feedthrough for electrical connections. The cathode was made from standard graphite plate electrode (GraphiteStore, Northbrook, IL, USA) with a size of 25 × 25 × 3 mm. Cathode electrodes were polished and reused in the same MFCs for all experiments. Electrical connections to both electrodes were protected with epoxy. Electrodes were placed at a distance 5 mm from each side of the CEM to minimize variations in internal resistance for all MFCs. Ports were sealed with supplied gas-tight cap, except for the wire feedthrough port which was sealed with epoxy.

Bacterial Culture and Nutrients: G. sulfurreducens (wild type, strain PCA, ATCC 51573), aliquots were stored in a −80 °C biological freezer (Thermo Scientific Revco EXF, Burlington, ON, Canada). All preparatory steps were conducted in an oxygen-free environment in a glovebox (10% H2, 10% CO2, and 80% N2). *G. sulfurreducens* was subcultured in nutrient medium supplemented with 40 × 10−3 m sodium fumarate (Na2C4H2O4) as a soluble electron acceptor to support bacterial growth in solution. The nutrient medium consisted of sodium acetate carbon source (CH3COONa, 10 × 10−3 m), NaH2PHO4 (3.8 × 10−3 m), NaHCO3 (30 × 10−3 m), KCl (1.3 × 10−3 m), NH4Cl (28 × 10−3 m) (all from Sigma-Aldrich, Oakville, ON, Canada), a trace mineral supplement (ATCC MD-TMS, 10 mL L−1), and a vitamin supplement (ATCC MD-VS, 10 mL L−1). The medium was sterilized before use by autoclaving at 110 °C at 20 psi for 20 min. Sodium fumarate was added through a sterilized filter in the glovebox.

MFC Preparation: Inoculation and Start-Up: The MFC anode chamber was inoculated with 125 mL of liquid, consisting of 4 mL of *G. sulfurreducens* subculture and the rest being nutrient medium. No fumarate was added to the anolyte solution in order to support growth at the anode only. The catholyte and anolyte solutions, and their ionic strength, were matched to those previously reported.[9] Briefly, the cathode compartment was filled with 125 mL of a PBS (10 × 10−3 m, pH = 7.4); containing 30 × 10−3 m ferricyanide (as an electron acceptor). All operations were conducted inside an anaerobic glovebox. Next, the MFC liquid ports were sealed and the anode and cathode were connected through a resistor, Rext = 100 kΩ. This was chosen based on measurements of average internal resistances from previous experiments using the same setup and from literature reports with MFCs featuring small gold anodes.[43] All reactors were operated at 24 ± 0.5 °C with gentle stirring in an oxygen-free environment.

Characterization: Optical Profilometry: Optical profilometry measurements were made using a Zygo NewView 5000 white light interferometer (Zygo Corporation, Middlefield, CT, USA). Data were obtained for the gold films on PS substrates, before and after shrinking. Five different areas on each substrate were imaged onto a charge coupled device camera using a 50× objective with 2× additional optical zoom, resulting in fields of view of 70 × 50 μm, and a pixel size of 112 nm. The topographical maps obtained through optical profilometry were used to calculate the RMS roughness of each of the surveyed areas, from which an average RMS roughness was calculated. For all images, a fast Fourier transform (FFT) bandpass filter was applied to remove noise with cut-off frequencies of 183.35 and 558.79 mm−1. Image analysis was conducted by MetroPro software (Zygo Corporation).

Scanning Electron Microscopy: SEM images of the gold electrodes were acquired with a JSM-7000S system (JEOL USA Inc., Peabody, MA, USA) operating with an accelerating voltage of 2.5 kV, working distance of 6 mm, and low probe current of 30 μA. The SEM images of gold electrodes were obtained before introduction to MFC anode compartment as well as after exposure to anode compartment for both electrically connected and unconnected gold surfaces. For SEM imaging of wrinkled gold surfaces after exposure to anode chamber, the anodes were exposed to a fixation solution overnight (2.5% glutaraldehyde in PBS buffer). The anode was then transferred to a solution with 1% osmium tetroxide for 1.5 h and rinsed in phosphate buffer. Samples were then dehydrated in 50%, 75%, 95%, and 100% aqueous ethanol solutions for 15 min each, followed by room temperature drying overnight. Before taking images, a thin gold layer was sputtered onto the biofilms and electrodes (Nanotech Ltd., SEM-PREP 2 Sputter Coater, Sandy, UK). *Focused Ion Beam Milling*: FIB milling was used to obtain a crosssectional view of the structured surfaces. A Helios NanoLab 600i DualBeam microscope (FEI, Hillsboro, OR, USA) combining an electronic column (SEM) and an ionic column (FIB) was used to etch the sample using Ga ions. Initial large-scale milling was done at 30 kV/21 nA, to create an opening in the bulk of the material, and a fine-scale finishing milling was done at 30 kV/2.5 nA, to clean the crosssection for imaging with SEM.

Persistence Length Calculation: The persistence length, defined as the distance over which a wrinkle maintained its original orientation, is a good approximation of the distance between wrinkle features. Persistence lengths corresponding to the different film thicknesses were calculated from the 2D FFT power spectra of the corresponding SEM images as previously described.[32] Briefly, SEM images were cropped into 900 × 900 pixel images and analyzed individually. Each image was adjusted for its brightness and contrast, after which the Canny threshold method in MATLAB was used to determine the edges of the wrinkled structures, which were rendered as a binary image. A MATLAB program was used to run a 2D FFT of the binary image, from which the power spectrum and probability versus length scale (μm) plots were generated. The probability values were normalized to the maximum probability, averaged for all SEM images, and analyzed for each data point. A probability versus log (length scale) plot was used to identify the values corresponding to the highest probability, which were used to determine the persistence length of the structured films.

Cyclic Voltammetry: Cyclic voltammetry was performed using an electrochemical workstation (CHI 660D, CH Instruments, Austin, TX, USA) and a standard three-electrode set-up. The electrochemical cell included a Ag/AgCl reference electrode, a Pt auxiliary electrode, and sputtered gold films on polystyrene as working electrodes. To ensure that the planar geometric surface area of the working electrode was consistent between samples before and after shrinking, an adhesive vinyl mask was placed over the gold electrode with a 2 mm diameter circle cutout to expose the active surface of the electrode. To determine the total electroactive surface area of the samples, 10 voltammograms were acquired in a 100 × 10−3 m H2SO4 solution at a scan rate of 0.1 V s−1 and a voltage sweep range of 0.5–1.5 V. The cathodic peaks from the resulting voltammograms were integrated using OriginPro software to determine the total charge transferred. The electroactive surface area was then calculated by dividing the total charge by the surface charge density of a monolayer of gold (386 μC cm−2).

Electroactive Biofilm Analyses and Calculations: Parallel electrical measurements of the voltage drop across an external resistor (*R*ext) were conducted for all five MFCs using a microcontroller board (Arduino UNO, Digikey Electronics, Thief River Falls, MN). Measurements were acquired at intervals of 10 min and the time-varying current was calculated using Ohm's law $I = V/R\text{ext}$, where V was the time-varying voltage drop across *R*ext. Polarization curves were obtained with a commercial potentiostat (VersaSTAT 4, Princeton Applied Research, Oak Ridge, TN) with automatic changes to *R*ext in the range of 25 to 250 k**Ω** after a settling time of 10 min. The power (*P*) of the MFCs was calculated using $P = V2/R\text{ext}$ and power density curves were generated showing *P* versus *I* for different values of *R*ext.

Resonance Raman Spectroscopy: Analysis by resonance Raman spectroscopy was used to verify the existence of c-type cytochromes within *G. sulfurreducens* biofilms on gold after the experiments. Preparation included removal from the MFC anode chamber, washing with acetate-free medium and exposure to filtered air from a laminar flow hood for drying. Raman spectra were recorded (LABRAM 800HR, Horiba JobinYvon, Villeneuve d'Ascq, France) with a 100×/0.75NA long working distance objective in backscattering mode with excitation provided by an argon-ion laser at 514 nm. At this wavelength, resonant excitation of the cytochrome Q-band (oriented in plane of the porphyrin ring) could be acquired.[44] The acquisition time was 30 s for all samples.

Acknowledgements

M.A.A. and S.S. contributed equally to this work. The authors would like to thank Luc Trudel and Laurent Smith (U. Laval) for support in the preculture of *G. sulfurreducens*, Richard Janvier for SEM imaging and preparation, and Benjamin Reig for help obtaining the FIB images. S.S. is the recipient of an Ontario Graduate Scholarship. J.M.M. and J.G. are the recipients of Early Researcher Awards from the Ontario Ministry of Research and Innovation and the Fonds de recherche du Québec— nature et technologies, respectively. J.M.M. is the Canada

Research Chair in Micro and Nanostructured Materials. This research was supported by funding through the Natural Sciences and Engineering Research Council and made use of instrumentation from the McMaster Manufacturing Research Institute, Canadian Centre for Electron Microscopy and the Centre for Emerging Device Technology.

Conflict of Interest

The authors declare no conflict of interest.

Keywords

direct electron transfer, electroactive biofilm, microbial fuel cells, wrinkled electrodes

REFERENCES

[1] H. Liu, R. Ramnarayanan, B. E. Logan, *Environ. Sci. Technol.* **2004**, *38*, 2281.

[2] B. E. Logan, *Microbial Fuel Cells*, John Wiley & Sons, New Jersey **2008**.

[3] X.-Y. Yang, G. Tian, N. Jiang, B.-L. Su, *Energy Environ. Sci.* **2012**, *5*, 5540.

[4] B. Logan, *Nature* **2008**, *454*, 943.

[5] D. R. Lovley, *Nat. Rev. Microbiol.* **2006**, *4*, 497.

[6] B. Ringeisen, E. Henderson, P. Wu, J. Pietron, *U.S. Patent Application11/ 308*, 216, **2006**.

[7] M. M. Mardanpour, S. Yaghmaei, *Biosens. Bioelectron.* **2016**, *79*, 327.

[8] M. Hernandez, D. Newman, *Cell. Mol. Life Sci.* **2001**, *58*, 1562.

[9] K. P. Nevin, H. Richter, S. Covalla, J. Johnson, T. Woodard, A. Orloff, H. Jia, M. Zhang, D. Lovley, *Environ. Microbiol.* **2008**, *10*, 2505.

[10] H. J. Kim, H. S. Park, M. S. Hyun, I. S. Chang, M. Kim, B. H. Kim, *Enzyme Microb. Technol.* **2002**, *30*, 145.

[11] C. S. Kang, N. Eaktasang, D.-Y. Kwon, H. S. Kim, *Bioresour. Technol.* **2014**, *165*, 27.

[12] A. E. Inglesby, D. A. Beatty, A. C. Fisher, *RSC Adv.* **2012**, *2*, 4829.

[13] D. R. Lovley, *Energy Environ. Sci.* **2011**, *4*, 4896.

[14] H. Richter, K. McCarthy, K. P. Nevin, J. P. Johnson, V. M. Rotello, D. R. Lovley, *Langmuir* **2008**, *24*, 4376.

[15] N. S. Malvankar, M. T. Tuominen, D. R. Lovley, *Energy Environ. Sci.* **2012**, *5*, 8651.

[16] X. Xie, L. Hu, M. Pasta, G. F. Wells, D. Kong, C. S. Criddle, Y. Cui, *Nano Lett.* **2010**, *11*, 291.

[17] X. Xie, G. Yu, N. Liu, Z. Bao, C. S. Criddle, Y. Cui, *Energy Environ. Sci.* **2012**, *5*, 6862.

[18] B. Logan, S. Cheng, V. Watson, G. Estadt, *Environ. Sci. Technol.* **2007**, *41*, 3341.

[19] Y. Qiao, S.-J. Bao, C. M. Li, X.-Q. Cui, Z.-S. Lu, J. Guo, *ACS Nano* **2007**, *2*, 113.

[20] Y. Fan, S. Xu, R. Schaller, J. Jiao, F. Chaplen, H. Liu, *Biosens. Bioelectron.* **2011**, *26*, 1908.

[21] J. E. Mink, J. P. Rojas, B. E. Logan, M. M. Hussain, *Nano Lett.* **2012**, *12*, 791.

[22] S. Inoue, E. A. Parra, A. Higa, Y. Jiang, P. Wang, C. R. Buie, J. D. Coates, L. Lin, *Sens. Actuators, A* **2012**, *177*, 30.

[23] X. Tang, G. Zhang, Y. Zhao, *Nanotechnology* **2006**, *17*, 4439.

[24] A. L. Kane, D. R. Bond, J. A. Gralnick, *ACS Synth. Biol.* **2012**, *2*, 93.

[25] S. Choi, H.-S. Lee, Y. Yang, P. Parameswaran, C. I. Torres, B. E. Rittmann, J. Chae, *Lab Chip* **2011**, *11*, 1110.

[26] C.-C. Lin, C.-H. Wei, C.-I. Chen, C.-J. Shieh, Y.-C. Liu, *Bioresour. Technol.* **2013**, *135*, 640.

[27] M. Sun, F. Zhang, Z.-H. Tong, G.-P. Sheng, Y.-Z. Chen, Y. Zhao, Y.-P. Chen, S.-Y. Zhou, G. Liu, Y.-C. Tian, *Biosens. Bioelectron.* **2010**, *26*, 338.

[28] S. Saem, Y. Zhu, H. Luu, J. M. Moran-Mirabal, *Sensors* **2017**, *17*, 732.

[29] S. Sonney, N. Shek, J. M. Moran-Mirabal, *Biomicrofluidics* **2015**, *9*, 026501.

[30] Y. Zhu, J. M. Moran-Mirabal, *Adv. Electron. Mater.* **2016**, *2*, 1500345.

[31] C. M. Gabardo, Y. Zhu, L. Soleymani, J. M. Moran-Mirabal, *Adv. Funct. Mater.* **2013**, *23*, 3030.

[32] U. Gill, T. Sutherland, S. Himbert, Y. Zhu, M. C. Rheinstädter, E. D. Cranston, J. M. Moran-Mirabal, *Nanoscale* **2017**, *9*, 7781.

[33] N. Lebedev, S. M. Strycharz-Glaven, L. M. Tender, *Front. Energy Res* **2014**, *2*, 34.

[34] H. Ren, S. Pyo, J.-I. Lee, T.-J. Park, F. S. Gittleson, F. C. Leung, J. Kim, A. D. Taylor, H.-S. Lee, J. Chae, *J. Power Sources* **2015**, *273*, 823.

[35] H. Wang, G. Wang, Y. Ling, F. Qian, Y. Song, X. Lu, S. Chen, Y. Tong, Y. Li, *Nanoscale* **2013**, *5*, 10283.

[36] G. Choi, D. J. Hassett, S. Choi, *Analyst* **2015**, *140*, 4277.

[37] M. P. Zarabadi, F. Paquet-Mercier, S. J. Charette, J. Greener, *Langmuir* **2017**, *33*, 2041.

[38] H. Ben-Yoav, A. Freeman, M. Sternheim, Y. Shacham-Diamand, *Electrochim. Acta* **2011**, *56*, 7780.

[39] R. P. Ramasamy, Z. Ren, M. M. Mench, J. M. Regan, *Biotechnol. Bioeng.* **2008**, *101*, 101.

[40] Z. Ren, R. P. Ramasamy, S. R. Cloud-Owen, H. Yan, M. M. Mench, J. M. Regan, *Bioresour. Technol.* **2011**, *102*, 416.

[41] F. Yu, C. Wang, J. Ma, *Electrochim. Acta* **2018**, *259*, 1059.

[42] J. Shen, C. Wang, Y. Liu, C. Hu, Y. Xin, N. Ding, S. Su, *Biochem. Eng. J.* **2018**, *129*, 44.

[43] F. Qian, M. Baum, Q. Gu, D. E. Morse, *Lab Chip* **2009**, *9*, 3076.

[44] N. Lebedev, S. M. Strycharz-Glaven, L. M. Tender, *ChemPhysChem* **2014**, *15*, 320.

Chapter 4: Benchtop-fabricated lipid-based electrochemical sensing platform for the detection of membrane disrupting agents

This chapter has been submitted as:

Sokunthearath Saem, Osama Shashid, Adree Khondker, Camila Moran-Hidalgo, Maikel C. Rheinstädter, and Jose Moran-Mirabal.* (2019) Benchtop-fabricated lipid-based electrochemical sensing platform for the detection of membrane disrupting agents. *Submitted.*

Author Contributions: SS and JMM planned the study. SS fabricated the lipid sensors, characterized the sensors, and optimized the methodology. OS performed cyclic voltammetry experiments. AK and MCR performed the X-ray diffraction experiments. CMH performed the electrochemical optimization experiments.

Benchtop-fabricated lipid-based electrochemical sensing platform for the detection of membrane disrupting agents

Sokunthearath Saem,[†] Osama Shashid,[†] Adree Khondker,[‡] Camila Moran-Hidalgo,[†] Maikel C. Rheinstädter,[‡] and Jose Moran-Mirabal[†,*]

[†]Department of Chemistry and Chemical Biology, [‡]Department of Physics and Astronomy, McMaster University, Hamilton, Ontario, Canada

Keywords: (biosensor, electrochemistry, DMPC, microstructured electrodes, hemolytic agents, membrane disruption, cell death, benchtop microfabrication)

ABSTRACT

There are increasing concerns about the danger that water-borne pathogens and pollutants pose to the public. Of particular importance are those that disrupt the plasma membrane, since loss of membrane integrity can lead to cell death. Currently, quantitative assays to detect membrane-disrupting (lytic) agents are done offsite, leading to long turnaround times and high costs, while existing colorimetric point-of-need solutions often sacrifice sensitivity. Thus, portable and highly sensitive solutions are needed to detect lytic agents for health and environmental monitoring. Here, a lipid-based electrochemical sensing platform is introduced to rapidly detect membrane-disrupting agents. The platform combines benchtop fabricated microstructured electrodes (MSEs) with lipid membranes. The sensing mechanism of the lipid-based platform relies on the stacked membranes serving as passivating layers that when disrupted; generate electrochemical signals proportional to the membrane damage. The MSE topography, membrane casting and annealing conditions were optimized to yield the most re-

producible and sensitive devices. We used the subsequent sensors to detect membrane-disrupting agents sodium dodecyl sulfate and Polymyxin-B within minutes and with limits of detection in the ppm regime. This study introduces a method with potential for the integration of complex membranes on MSEs towards the goal of developing a Membrane-on-a-Chip sensing platform.

4.1. INTRODUCTION

Bacterial pathogens, pesticides, and parasitic vectors are common risks that need to be screened for in water by using reliable methods of detection, such as ELISA, chromatography, and mass spectrometry. While these methods offer high precision and accuracy, they are expensive, require highly trained technicians, or are time consuming,[99–101] which precludes their use in resource-limited environments.[102–105] Thus, there is an increasing demand for diagnostic tools that do not compromise affordability, sensitivity, and portability for applications in point-of-care (PoC) diagnostics,[105,106] personalized medicine,[107,108] food quality testing,[109,110] and water testing.[111] Biosensors are attractive routes to address these needs because they leverage biorecognition elements to offer rapid and low-cost solutions for the detection of potentially harmful agents and can be adapted to portable platforms.[112–115]

The cell plasma membrane is a complex structure that separates the internal cellular components from external environments. Apart from protecting the cell from its surroundings, the plasma membrane mediates ions and small molecule transport, adhesion, motility, and the uptake of larger foreign bodies through endocytosis. The membrane is primarily composed of a phospholipid bilayer, within which sterols, carbohydrates, and proteins are embedded. These additional components modulate the plasma membrane's physicochemical properties and biological function. Perturbation of a biological membrane through small molecules and proteins that destabilize the phospholipid bilayer can result in membrane damage, cell lysis, and death. This series of events is of particular concern when the destabilizing agents are of synthetic or pathogenic origin and they result in the lysis of cells. Existing biosensors for the detection of synthetic lytic agents mostly rely on catalytic (e.g., enzyme inhibition) or affinity based systems (e.g., antibodies, aptamers, lectin, and bacteriophages).[112–114,116–119] Moreover, lytic factors produced by human pathogens are of particular concern because the severity of bacterial infection increases dramatically for hemolytic bacteria, particularly in immunocompromised populations.[120] Currently, the gold standard for diagnosing hemolytic bacterial infections is the blood agar test, which relies on an overnight culture and visual inspection that make it time-consuming and qualitative. Thus, the complexity of existing sensing systems for the detection of synthetic lytic agents and the shortcomings of the blood agar test present a unique opportunity for the development of innovative sensing solutions for the detection of lytic agents that are low-cost, portable, rapid, and simple to operate.

The past few decades have seen a rapid expansion in the field of biosensors, with optical and electrochemical methods as the dominant sensing techniques.[113,115] This success is best exemplified by commercial PoC glucose-testing amperometric sensors, which present key advantages in miniaturization, rapid detection, quantification, and low production cost. Recently, lipid-based electrochemical biosensors have been proposed for the rapid and quantitative detection of harmful pathogens. A recent study used liposomes loaded with a redox mediator to detect hemolytic bacteria.[121,122] In this system, the liposomes burst upon exposure to the lytic agent, which released the redox mediators to produce a quantifiable electrochemical signal. While effective in a laboratory setting, this system requires multi-step kinetics before signal acquisition, a large number of components, extensive sample preparation, and lacks portability and sensitivity. More recent adaptation of lipid-based lytic sensors use supported lipid bilayers (SLBs) or tethered bilayer membranes (tBLMs) on conductive surfaces coupled with electrical impedance spectroscopy (EIS) for the sensing of lytic compounds.[123–125] However, existing systems use planar electrodes and in the case of tBLMs require surface immobilization of a tethering agent which adds additional production time, complexity, and variability to the biosensor. Additionally, most lipid-based sensing systems employ EIS as an electrochemical technique. Although sensitive, EIS can be time consuming due to the use of large frequency sweeps, expensive and difficult to miniaturize, and often require complex data analysis and fitting for quantification.[126,127] The limitations in such lipid-based biosensing technologies for the detection of harmful lytic agents preclude their application for a growing biosensing market. Therefore, there is a need for low-cost, simple to operate, and quantitative assays to detect lytic agents efficiently and rapidly.

This work presents a platform that exploits the natural barrier properties of lipid membranes for the electrochemical detection of lytic agents. In this platform, simple and low-cost benchtop microfabrication techniques are used to produce highly sensitive gold microstructured electrodes (MSEs),[19,76] which are then coated with model membranes composed of 1,2-dimyristoyl-*sn*-glycero-3-phosphocholine (DMPC). The operating principle of the lipid-based sensor is that while the DMPC membrane is intact, it passivates the MSE shielding it from redox-active molecules in solution and preventing electrochemical signal generation. Exposure to lytic agents permeabilizes the membrane, which reveals the MSE surface to the solution containing redox active reporter molecules and subsequently resulting in the generation of an electrochemical signal proportional to the concentration of the lytic agents. We have performed sensing studies using this platform for the quantitative detection of an ionic surfactant (sodium dodecyl sulfate, SDS) and an antimicrobial drug (Polymyxin-B, PmB). The fabrication of the lipid-based sensors was optimized to produce the fastest response to lytic factors and reduce the material cost. The optimized lipid sensors were able to rapidly (seconds to minutes) and reproducibly detect SDS and PmB, with LODs of 10 and 1 ppm, respectively. The presented platform combines affordable bench-top fabrication techniques and electrochemistry to offer a scalable and versatile method that could be used to rapidly detect lytic agents in aqueous samples. Current efforts in our lab aim to increase the complexity of the lipid membranes used in the sensors to endow them with selectivity towards specific classes of membrane disrupting agents. We anticipate that this type of lipid-based sensor can be used in the future within PoC devices where a range of lytic factors can be detected and quantified, eventually replacing current qualitative gold standards like the blood agar test.

4.2. MATERIALS AND METHODS

4.2.1. Structured Electrode Fabrication

All electrodes were fabricated on pre-stressed polystyrene (PS) films (Graphix Shrink Film, Graphix, Maple Heights, OH, USA). PS films were washed with isopropanol (IPA), ethanol (EtOH), and $18.2\ \mathrm{M\Omega \cdot cm}$ water baths (5 min each) under orbital agitation (60 rpm) and dried under a nitrogen stream. Adhesive vinyl sheets (FDC-4300, FDC graphic films, South Bend, IN, USA) were cut into stencils to define the electrode shapes using a Robo Pro CE5000-40-CRP blade cutter (Graphtec America Inc., Irvine, CA, USA) equipped with a

CB09UA supersteel blade. The vinyl stencils (Figure 4.1A) were peeled and transferred onto the clean shrink films, which were cut with the blade cutter into individual rectangular substrates. The PS substrates were then placed in a Torr Compact Research Coater CRC-600 manual planar magnetron sputtering system (New Windsor, NY, USA), and 99.999% purity gold (LTS Chemical Inc., Chestnut Ridge, NY, USA) was sputtered onto the PS substrates at a rate of 0.5 Å/s to the desired thickness. The argon plasma was generated using a 70 mA DC current and a gas flow of 5 sccm. After Au deposition, the vinyl stencils were peeled-off from the substrates, revealing patterned gold electrodes. The electrodes (PS + Au film) were placed in an oven at 160°C for 5 min to thermally shrink the PS substrate and structure the electrodes. The microstructured electrodes (MSEs) were stored in a sealed container until further needed.

4.2.2. Lipid deposition

Immediately before lipid deposition, the MSEs were rinsed with IPA, EtOH, $18.2\ \mathrm{M\Omega \cdot cm}$ water and dried under a dry nitrogen stream. The electrode surfaces were further cleaned through exposure to UV/O_3 (185 nm and 254 nm, PSD-UV Benchtop UV-Ozone Cleaner, NOVASCAN, IA, USA) for 15 min at room temperature, followed by a 5-minute air plasma treatment (30 sccm air flow, 600 mTorr) in a PDC expanded oxygen plasma cleaner (Harrick, Ithaca, NY, USA) operated in high power setting (30 W). DMPC (1,2-dimyristoyl-sn-glycero-3-phosphocholine, Avanti Polar Lipids Inc, Alabaster, AL, USA) solutions (0.05 – 0.5 mg/mL) were made using a 1:1 mixture of chloroform and 2,2,2-trifluoroethanol ($CHCl_3$:TFE) as a solvent. The electrodes were masked with a rectangular vinyl adhesive mask that left only the circular working electrode area exposed (Figure 4.1B). Once masked, the electrodes were placed on a hot plate preheated to 50°C for 5 min. Then, 15 µL of the DMPC solution were deposited dropwise onto the circular electrode working pad. The electrodes were left on the hotplate for 5 min to ensure complete solvent evaporation. The effect of vacuum, annealing temperature and annealing time were studied to optimize the DMPC lipid bilayer formation on the MSEs. Following DMPC deposition, the lipid-MSEs were annealed at atmospheric pressure or in vacuum, at temperatures between 25 – 50°C, for various lengths of time, and at various relative humidity conditions. The results of these optimization tests are summarized in Supplementary Information Figure 4.S1. Briefly, we determined that vacuum, humidity, and annealing duration had insignificant contribution to the desired electrode passivation effect. However, annealing at 50°C showed approximately 30% greater MSE passivation compared to devices made at room temperature. Therefore, the optimal annealing conditions of 50°C for 1 hour were used. After the annealing process, the electrodes were left to cool in a desiccator for 10 min, and the drop casting mask was removed and replaced by a sensing mask (Figure 4.1B). The electrodes were then used for electrochemical sensing with the sensing mask in place.

4.2.3. Electrochemical sensing

Potassium ferrocyanide (KFeCy – $K_4[Fe(CN)_6]\cdot 3H_2O$, Sigma-Aldrich, Oakville, ON, Canada) was used as redox-active reporter to generate an electrochemical signal when performing cyclic voltammetry (CV) measurements. All sensing solutions used in this study consisted of 2mM KFeCy in 1x PBS (137 mM NaCl, 2.7 mM KCl, 8 mM Na_2HPO_4 and 2 mM KH_2PO_4, pH = 7.4, Sigma-Aldrich, Oakville, ON, Canada). For initial membrane disruption experiments, a variable amount of sodium dodecyl sulfate (SDS, Sigma-Aldrich, Oakville, ON, Canada) was added to the sensing solution to achieve the desired SDS concentration. CV measurements were performed using a CHI600E electrochemical workstation (CH Instruments, Austin, TX, USA) in a three-electrode electrochemical cell setup, where the structured electrode was used as the working electrode (WE), a platinum wire was used as auxiliary electrode (AE), and an Ag/AgCl electrode served as the reference electrode (RE). During sensing, all three electrodes were connected to the electrochemical work station and submerged in 15 mL of the sensing solution. The CV experiments were performed with a voltage sweep from 0 to 0.4 V at 0.1 V/s scan rate for 10 segments. A sensing solution with Polymyxin B (PmB) (Sigma-Aldrich, Oakville, ON, Canada) was prepared and tested for membrane disruption in the same way as SDS solutions. To completely remove leftover lipids after sensing and recycle the electrodes, they were washed successively with IPA, EtOH, and $18.2\ \mathrm{M\Omega \cdot cm}$ water, and dried with a dry nitrogen stream. The clean electrodes were stored in a desiccator to be reused.

4.2.4. X-ray scattering

X-ray scattering data was obtained using the Biological Large Angle Diffraction Experiment (BLADE) at McMaster University. BLADE uses a 9kW (45 kV, 200mA) CuKα rotating anode at a wavelength of 1.5418 Å. Both source and detector are mounted on movable arms, such that the sample stays horizontal during measurements. The beam was focused using multi-layer optics through a 200 mm collimator resulting in a high intensity beam with monochromatic X-ray intensities up to 10^8 counts/s and detected on a HyPix300 two-dimensional detector. The sensors were scanned at a temperature of T = 28°C and ~50% relative humidity (RH). The two-dimensional intensity maps were then used for quantification of lipid organization within the sample. A powder diffraction peak was observed ~1.5 Å^{-1}, corresponding to lipid-lipid distances within a lamellar phase. The spacing in real-space may be determined from $d = 2\pi/q_T$ from Bragg's Law. The peak intensity, proportional to the presence of organized lipids upon the sample surface, was determined from radially integrating from $1.4 < q_{z,||} < 1.6$ for each sample.

4.3. RESULTS AND DISCUSSION

The sensing platform was implemented using model membranes, which simplified the biological membrane down to its major component and allowed us to assess the impact of different device and sample preparation parameters on sensor performance. In the experiments reported we used membranes composed of DMPC, a phospholipid with two 14-carbon aliphatic tails and a zwitterionic phosphocholine head-group that has been widely used as biomimetic membranes.[128,129] DMPC having fully saturated tails will also ensure that we can obtain membranes with high packing density to ensure the best chance of MSE chip passivation. The main concept behind the sensor platform, discussed in detail below, is that lipids deposited on a structured electrode form a passivating layer that prevents a redox-active reporter added to the sample solution from accessing the working electrode surface. This results in negligible current generation during electrochemical sensing with an intact membrane. However, when the DMPC membrane is damaged by a membrane disrupting agent (*e.g.* surfactants, drugs, pathogen-derived hemolytic peptides) and holes are formed in the passivating layer, the redox reporter molecules can diffuse to the electrode surface, generating an electrochemical signal. The strength of the signal depends on the composition and concentration of the membrane disrupting agent and the amount of damage caused to the membrane, as well as on the total surface area of the working electrode used in building the sensor. The platform developed takes advantage of lipid membranes deposited on high surface area structured electrodes and electrochemistry to provide rapid and highly sensitive detection of membrane destabilizing compounds.

4.3.1. Electrode fabrication and characterization

Gold MSEs have increased electroactive surface area (EASA) and thus the signal detected by the sensor, while at the same time decreasing the footprint of the sensing area. The electrodes were fabricated using commercial thermo-responsive polymer substrates (prestressed PS), as previously described[19] and as shown in Figure 4.1A. The final transverse dimensions of the shrunken electrodes were 40% of the original design (circular pad diameter was reduced from 12.5 to 5 mm), which corresponds to an overall reduction to 16% of the original area. The thermal shrinking of the underlying PS substrate caused the electrode surfaces to wrinkle and buckle, with the resulting feature sizes dictated by the thickness of the gold films. SEM and optical images of the electrode surfaces before and after shrinking (Figure 4.1D) show the expected increase in wrinkle size for thicker gold films, which arises from the stress imposed by the shrinking substrate and the mismatch in elastic modulus between the PS and the rigid film.[18] The resulting electrodes showed submicron-sized wrinkles for 20-nm-thick Au films and micron-sized wrinkles at Au thicknesses $\geq$ 50 nm. It must be noted that the wrinkled features were only observed in substrates containing Au films, and that images of bare PS substrates before and after shrinking showed that these substrates remained flat with no observable topographical differences. We have previously reported a comprehensive study on shrinking and wrinkling patterned electrodes and the enhancement of EASA contained within a given footprint to > 600%, when compared to a flat counterpart.[18,76] This enhancement can also be seen in the Supplementary Information, Figure 4.S4 comparing the electroactive surface area of planar Au electrode again the MSE. This EASA enhancement provides an advantage for the implementation of on chip electrochemical sensors, since a working electrode with 16% the footprint of a flat electrode will provide similar current output, offering improved portability and sensitivity. Previous electrochemical results also suggest that, despite the difference in the size of topographical features, there is no enhancement in the charge transfer efficiency when the thickness of the starting Au films is increased, since thin and thick films are compressed into similar final areas. Thus, to minimize the production cost of the sensing devices ($0.08/device for 20 nm *vs.* $1.60/device for 400 nm) we elected to use 20 and

50 nm thick gold films in the fabrication of the wrinkled electrodes used to demonstrate the lipid-based electrochemical sensing platform.

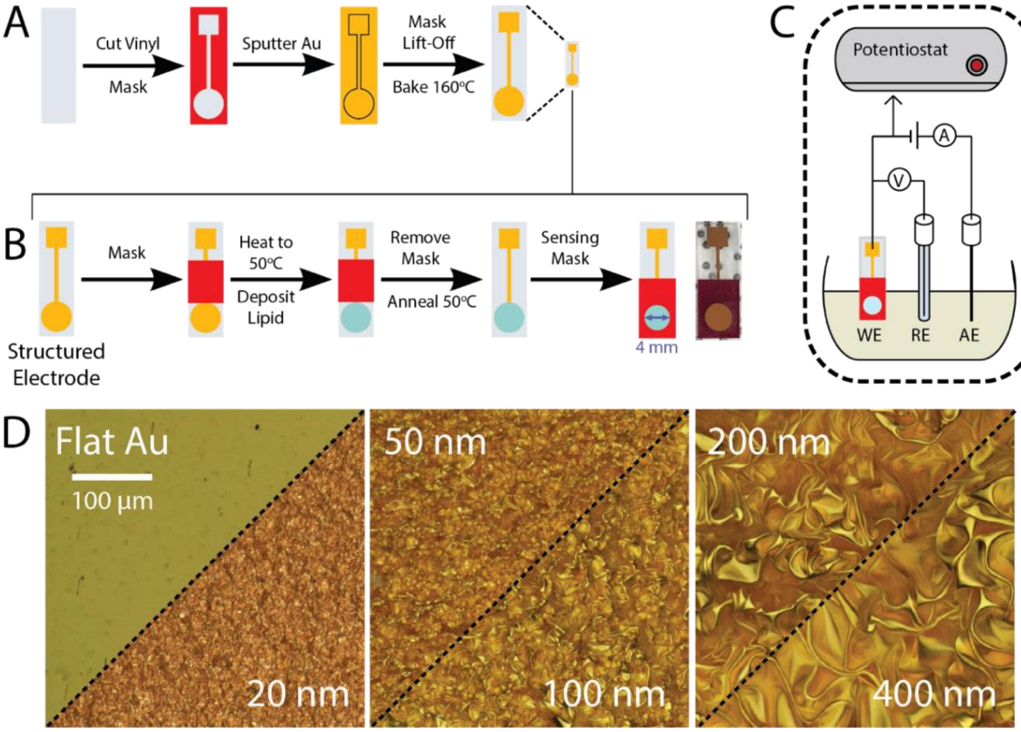

Figure 4.1. Schematic of the sensor fabrication and operation. **(A)** MSEs were fabricated on pre-stressed polystyrene substrates (clear rectangles), which were masked during gold deposition using adhesive vinyl stencils (red). After sputtering a thin gold layer (yellow), the stencils were removed to reveal the patterned electrode. Thermal shrinking of the substrate resulted in structuring of the Au films. **(B)** To form lipid membrane passivation layers the MSEs were masked to allow the deposition of lipid solution solely on the sensing pad. The lipids were deposited from stock solutions and the solvent was evaporated, forming thin lipid films that were annealed under optimized temperature and humidity conditions. Prior to sensing, a mask was applied on the MSE pad to ensure a reproducible membrane sensing surface. **(C)** Schematic of the 3-electrode electrochemical sensing set up. The DMPC-coated MSE was used as the working electrode (WE), with a Pt wire as the auxiliary electrode (AE), and a standard Ag/AgCl as a reference electrode (RE). **(D)** 3D optical reconstruction of 20-nm-thick flat and 20, 50, 100, 200 and 400 nm-thick microstructured Au films. All optical images taken at the same magnification.

4.3.2. Lipid-based sensor fabrication and principle of operation

The sensor fabrication process is shown in Figure 4.1B and explained in detail in the materials and methods section. Briefly, the MSE was masked with a rectangular vinyl adhesive and placed on a 50°C hotplate for 5 min. Fifteen microliters of the DMPC solution were drop cast onto the circular sensing pad. The coated electrodes were then annealed in an oven for 1 hour at 50°C to form stable lipid layers. The deposition mask was replaced by a sensing mask with a 4 mm-diameter cut-out exposing the sensing pad. Figure 4.1C shows the 3-electrode electrochemical setup with the DMPC lipid sensor as the working electrode.

The objective of this study was to create a sensing platform capable of detecting the presence of membrane-disrupting agents in solution by using model DMPC membranes to passivate the surface of gold MSEs. Cyclic voltammetry (CV) was used for the electrochemical detection of membrane damage by factors such as SDS and PmB. The sensing mechanism of the platform (Figure 4.2) relies on the electrochemical signal generated by a redox reporter molecule (KFeCy) added to the solution containing the sample. In CV measurements, when the voltage is cycled between 0 and 0.4 V on a bare MSE, the KFeCy reporter is oxidized and reduced resulting in anodic and cathodic current peaks (Figure 4.2A, inset). When a DMPC membrane is present on the MSE sensing pad, the KFeCy cannot access the Au surface to undergo redox processes, thus suppressing the current signal (Figure 4.2B, inset). In the presence of a membrane-disrupting factor (Figure 4.2C) the DMPC membrane is stripped away until the underlying Au is exposed, leading to the appearance of redox signal from the reporter. The evolution of the current signal is dependent on the concentration of membrane disruptors present in solution. Thus, the performance of the lipid-based electrochemical sensing platform would be dependent on the maximum electrochemical signal achievable, the time required to reach the maximum signal, and the lowest amount of analyte that could be detected.

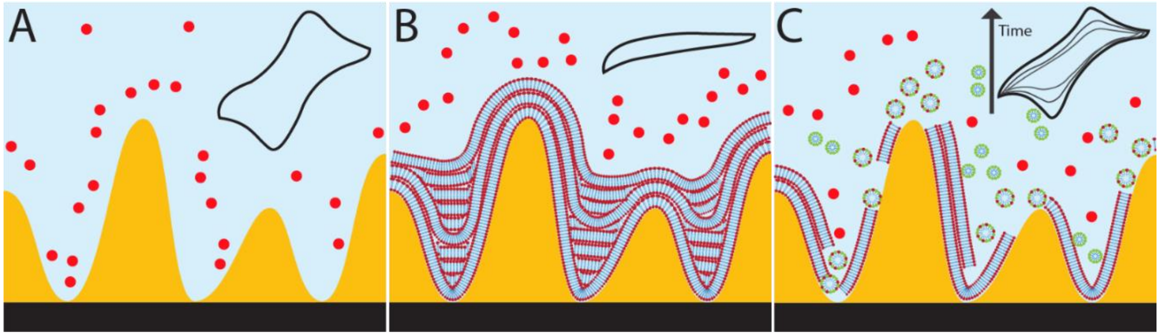

Figure 4.2. Sensing mechanism of the lipid-based electrochemical sensor. **(A)** Bare MSEs produce the maximum electrochemical signal from a redox reporter in solution (red dots); inset: typical CV curve. **(B)** DMPC membranes deposited on the MSEs passivate the electrode surface, preventing redox processes to occur; inset: CV with no signal. **(C)** When the sensor is exposed to a solution containing membrane-disrupting factors, the membrane degradation exposes the electrode surface and increasing redox signals are measured over time as shown in the inset. Gold surface topography and lipid layer drawings not shown to scale.

4.3.3. Influence of wrinkle size on sensor performance

The effect of the wrinkle size of the MSEs on DMPC membrane conformation and sensing ability was examined by depositing DMPC lipid membranes on electrodes fabricated from 20 – 400 nm thick films. To ensure full passivation of the electrodes, irrespective of wrinkle size, a DMPC solution with a concentration of 0.5 mg/mL (relatively high for the purpose of this study) was used to prepare the lipid membranes. Prior to testing the sensors against a membrane disrupting agent, each electrode was immersed in a 2 mM KFeCy solution and a 10-segment CV scan was performed, which helped identify current leakage due to unevenly deposited membranes. Once complete passivation was confirmed (*i.e.,* no current redox signal formation observed), the DMPC-coated electrode was immersed in a sample solution containing 2 mM KFeCy and 0.1% SDS, and sensing was done via CV. The anionic surfactant SDS was chosen as a test compound because it can disrupt the DMPC membrane through a detergent mechanism (Supplementary Information, Figure 4.S2). The speed of this action increases (*i.e.,* reducing the time required for appreciable membrane disruption from hours to minutes) with the concentration of SDS present in solution, which makes it an ideal compound for use as a synthetic lytic factor[130] to test the membrane-based sensors.

Signal arising from membrane disruption was quantified by the integration of the charge transferred during the redox cycling in CV measurements. The membrane-coated sensors were immersed in the SDS-containing solution and sensing was performed at room temperature with no agitation for 10 minutes. As the membrane was disrupted by SDS and more electrode surface became accessible the sweeping voltage in the CV reduced and oxidized the redox reporter (*i.e.,* KFeCy) producing cathodic and anodic peak currents that increased over time until reaching a plateau. To obtain quantitative information from the voltammograms obtained after 10-minute incubation, the cathodic peak was integrated (Figure 4.3A), from which the total charge transferred during the reduction process could be calculated. To eliminate any capacitive currents generated from non-faradaic processes and avoid integration bias, a baseline correction was established through a linear regression to two points in the reduction sweep where the current increased linearly with voltage (Figure 4.3A), as previously reported.[19] The total charge transferred for each DMPC sensor was normalized to that of its bare Au counterpart (*e.g.,* signals from 20 nm MSEs coated with DMPC sensor were normalized to 20 nm MSEs without DMPC), and all experiments were run in triplicate.

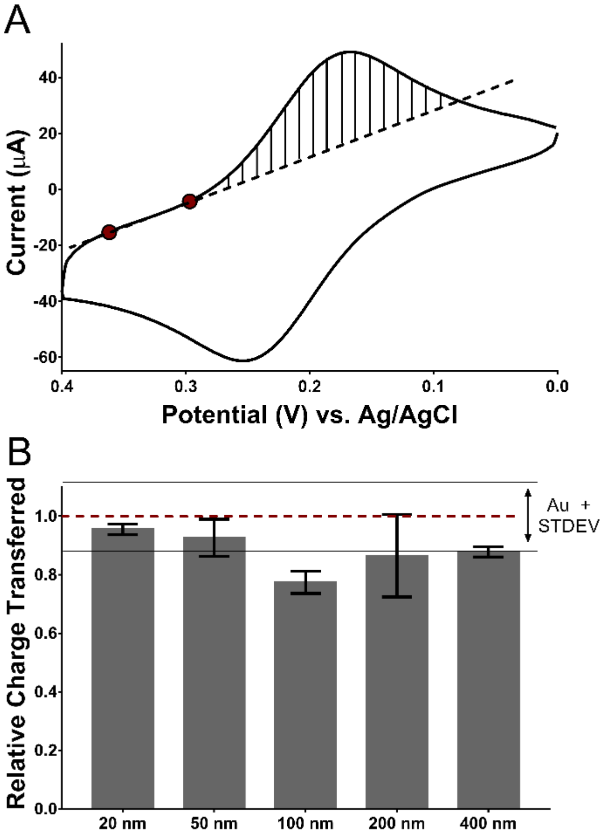

Figure 4.3. (A) Typical cyclic voltammogram of a solution containing 2mM KFeCy showing the linear regression used for the baseline correction of the cathodic peak. The peak was integrated after the linear regression to obtain the total charge transferred from the redox process. **(B)** Relative charge transfer plot of 20 – 400 nm MSEs coated with 0.5 mg/mL DMPC after being exposed to a 0.1% SDS solution for 10 minutes. The charge transferred was normalized to bare electrodes without membranes (dotted line). Bars represent the mean values and error bars shown are standard deviations obtained from n = 3 replicates.

A comparison of the relative charge transferred for the DMPC-coated sensors made from gold films of different thicknesses (Figure 4.3B) showed that sensors with smaller wrinkles led to higher and more reproducible signals given the lower standard deviations. Full signal recovery (with respect to the bare electrodes) was observed for sensors made with 20 and 50 nm wrinkled surfaces, whereas sensors made with 100, 200, and 400 nm wrinkled surfaces showed slightly lower average signal recovery. Overall, it was observed that the 20 nm sensors produced the highest signal to variance ratio compared to all other gold thicknesses. The lack of full signal recovery on sensors made from thicker gold films could be ascribed to lipid entrapment in the grooves of the wrinkled gold films. The data shown in Figure 4.3B suggests that, MSEs with smaller wrinkle spacing and height (i.e. thinner Au films) offer a topography that results in DMPC lipid films that can be more easily removed by a membrane disrupting agent, resulting in a more sensitive membrane-based sensor.

To further probe the membrane conformation on the MSEs, X-ray scattering experiments were performed on 20, 50 and 200 nm sensors coated with different amounts of DMPC. Figure 4.4A shows a typical 2D x-ray intensity plot obtained from membranes deposited on an MSE. Analysis of the diffraction data showed no significant signals at q-values of q_z~0.11 $Å^{-1}$, which would be related to membrane stacking along the out-of-plane (q_z) axis. The absence of lamellar Bragg peaks, which are intense in thick stacked membrane films,[131] was attributed to the presence of only a small number of stacked membranes (< 10) along with the high variability in the orientation of the surface topography, which leads to less ordered planar membranes. This would be consistent with the low amounts of DMPC added, which at the lowest concentration would only yield ~10-bilayer-films (if perfectly stacked and uniformly distributed) over the electrode surfaces. The radial pattern of intensity observed at q-values of ~1.5 $Å^{-1}$ and plotted in Figure 4.4B corresponds to the lipid tail peak (*i.e.,* the average distance between two acyl tails in the lipid membranes). This signal is proportional to the total amount of lipids on the area sampled and was therefore used to evaluate the uniformity of lipid deposition on the sensor. Figure 4.4C shows the total lipid content measured for MSEs coated with increasing lipid amounts. It can be observed that 20 and 50 nm sensors show trends of increasing intensity as more lipids were added, while the 200 nm sensor shows random behavior. Furthermore, the observation that 20 nm MSEs exhibited a linear trend with respect to the concentration of the lipid added implies that casting DMPC on the surface of these electrodes results in a more uniformly distributed membrane film. The radial integration of the lipid peak signal contained within the azimuthal angles $10 < \theta < 60$ also allowed us to determine the degree of orientation of the membranes by using Herman's orientation (HO) function:

$$H = \frac{3}{2} < \cos^2 \theta > -\frac{1}{2},$$

where a value of $H = 1$ represents a perfectly oriented bilayer, whereas a value of $H = 0.25$ represents a membrane with randomly oriented lipids. Typical values for highly oriented lamellar lipid bilayers on flat silicon substrates have been reported in the range of $H = 0.95$-0.98.[132] The HO values for membranes deposited on 20, 50, and 200 nm MSEs increased with increasing wrinkle size (0.65, 0.77 and 0.84 for 20, 50 and 200 nm respectively, Figure 4.4D). The lowest HO value, corresponding to the least order and/or higher membrane curvature was observed for 20 nm MSE. This suggests that the DMPC membranes formed on the surfaces with smaller wrinkles conformed better to the topography, which coupled to a more uniform coverage of the electrodes lead to more randomly oriented lipid bilayers. These results coupled to those obtained through electrochemical measurements indicate that sensors made using 20 and 50 nm MSEs provide the most uniformly deposited membranes with the highest signal to variance in the signal resulting from exposure to high concentrations of membrane disrupting factors. Thus, 20 and 50 nm MSEs were used for all subsequent optimization and sensing experiments.

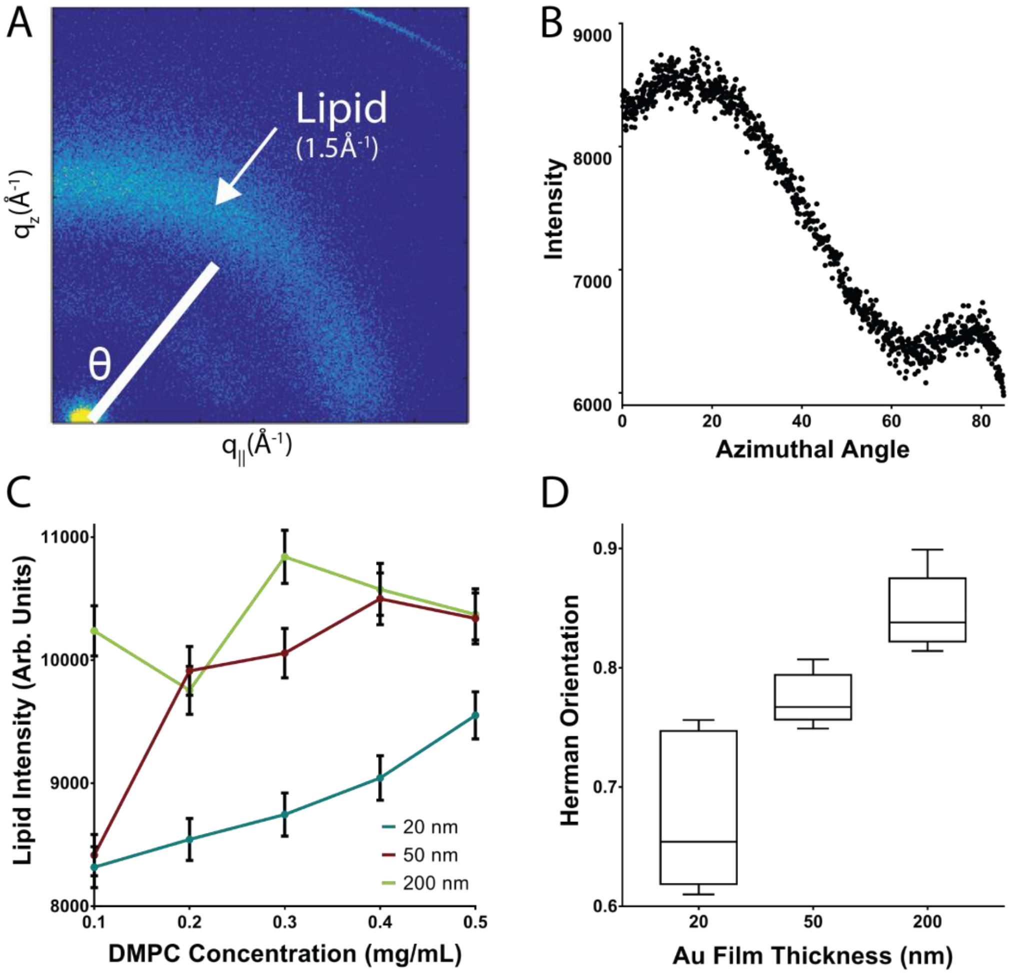

Figure 4.4. The DMPC membrane conformation on MSEs was assessed through X-ray diffraction. **(A)** A 2D reciprocal-space map of the diffraction intensity obtained from DMPC membranes deposited on MSEs. **(B)** Typical diffracted intensity vs azimuthal angle Θ plot. **(C)** Lipid peak intensity signal of DMPC membranes versus different lipid concentrations of the solution deposited. Lines represent data for MSEs made from films with different thicknesses, which led to different wrinkle sizes. **(D)** Plot of Herman's Orientation parameter versus MSE film thickness.

4.3.4. Optimization of membrane sensor response

The temporal response of the lipid-based sensing platform depends on the ability of the redox reporter to reach the electrode surface after the passivating membrane is damaged. Therefore, we sought to optimize the membrane deposition parameters to obtain the thinnest possible membranes while preserving complete passivation prior to exposure to the disrupting agents. The rationale behind this approach was that a thinner DMPC membrane would require a lower concentration of disrupting factors and less time for them to strip away the lipid membranes, allowing a faster and more sensitive electrochemical response. First, the ability to fully passivate 20 and 50 nm-thick MSEs was tested by depositing the membranes from solutions with increasing lipid concentrations (0.05 – 0.5 mg/mL). To ensure that the fabricated DMPC films were uniform, we started by using previously reported conditions for the deposition of lipids from solution.[133,134] Briefly, the DMPC solution was drop cast onto the MSE and the sensor was placed in a vacuum chamber for 24 hours followed by a 24 hours annealing at 100% RH and 50°C. These lipid membrane deposition conditions were used as a starting point to optimize the passivation of the MSEs for sensing applications.

After membrane deposition and annealing, the current leakage was assessed by sensing through CV in solutions containing 2 mM KFeCy, in the absence of disrupting agents. Figure 4.5 shows that at low lipid concentrations, the electrode surfaces were not fully passivated and allowed the generation of current peaks (leakage current). As the lipid concentration in the casting solution was increased, the surface was progressively less accessible and eventually became completely passivated. Full passivation was achieved for 20 nm MSEs at a lipid concentration of 0.2 mg/mL, while 0.4 mg/mL were required for 50 nm electrodes. The observation that electrodes with smaller wrinkles can be passivated by a smaller amount of DMPC can be explained by the topography, where smaller grooves would be easier to fill with lipids and result in a more even coating during drying and annealing. On the other hand, as the wrinkles become larger (*i.e.*, on MSEs made from thicker gold films) membranes have to cover topographies with deeper grooves, which leads to the non-uniform deposition of lipids and the formation of aggregates entrapped within the grooves until enough material is deposited to coat the tips of the wrinkles. These results are also consistent with our fluorescence and X-ray diffraction observations that electrodes with smaller wrinkles aid in the production of more uniform DMPC membranes. In view of the membrane deposition and uniformity results, we opted to use 20 nm MSEs for subsequent optimization and sensing experiments. An additional advantage of using 20 nm-thick gold films for the fabrication of the membrane-based sensors was the concomitant reduction of the production cost per sensor to ~$0.08 CAD.

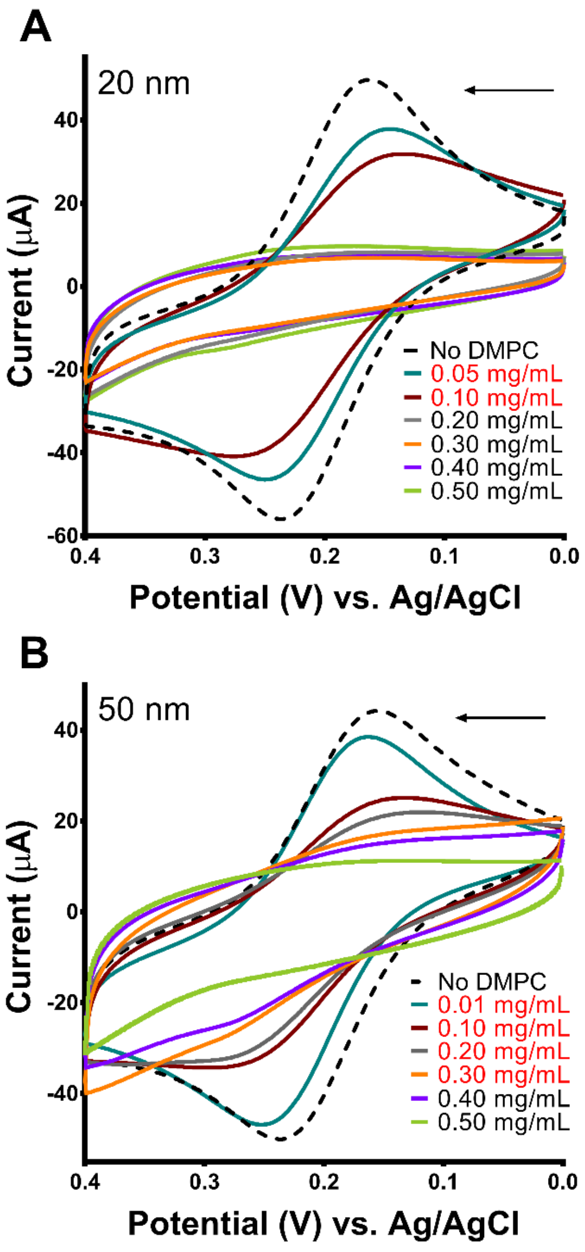

Figure 4.5. Cyclic voltammograms comparing current signal changes in DMPC concentrations between 20 nm and 50 nm thick wrinkled gold electrodes. All CV scans were performed in 2 mM KFeCy sensing solution without SDS. **(A)** Cyclic voltammograms of membranes deposited from DMPC solutions of varying concentrations on 20 nm wrinkled gold electrodes. **(B)** Cyclic voltammograms of membranes deposited from DMPC solutions of varying DMPC concentrations on 50 nm wrinkled gold electrodes.

The DMPC membrane preparation was further optimized by studying the effect of temperature, relative humidity, vacuum, and annealing time – variables that have been reported to affect membrane integrity. All membrane sensors for this optimization were prepared using 20 nm MSEs and 0.2 mg/mL DMPC solution and were immersed in a 0.1% SDS aqueous solution containing 2 mM KFeCy for 10 mins to determine the membrane stability using CV. In these experiments, the goal was to obtain the most stable membranes (*i.e.,* lowest relative charge transfer value for each condition tested), which would translate into sensors with higher reproducibility. No change in membrane stability was observed (Supplementary Information, Figure 4.S1) when the sensors were prepared: i) using solvent extraction in a vacuum for different lengths of time (0, 1, 4, and 24 hours), while maintaining humidity (100% RH), temperature (50°C), and annealing time (24 hours) constant; ii) annealing under different humidity conditions (ambient, 98% and 100% RH), while maintaining the annealing time (24 hours), annealing temperature (50°C), and vacuum time (24 hours) constant; or iii) using different annealing times (0.5, 1, 6 and 24 hours), maintaining humidity (100% RH), temperature (50°C), and vacuum time (24 hours) constant. The only factor that impacted membrane stability was the annealing temperature, where sensors prepared at 50°C produced the lowest charge transfer response at 1 minute of exposure to SDS when compared to those annealed at 25, 30, and 40°C (Supplementary Information, Figure 4.S1), indicating a more stable membrane. While 50°C resulted in a slower response, it still yielded full signal recovery (as compared to a bare electrode) at 10 minutes and, more importantly, presented the most reproducible passivation, with fewer sensors showing leakage current. Thus, the sensor preparation conditions were fixed for all subsequent experiments as no vacuum extraction and 1 hour annealing at 50°C and ambient RH, which yielded reproducible stable DMPC membranes.

4.3.5. Electrochemical sensing of membrane disrupting factors

To demonstrate the capabilities of the lipid-based sensor platform, sensing experiments were performed against two molecules known to degrade lipid membranes through a detergent-like mechanism, an anionic surfactant (SDS) and a cationic antibiotic (PmB). SDS was used as a model disrupting factor because its mechanism of action is well understood. On the other hand, PmB is a cyclic cationic polypeptide antibiotic produced by the soil bacterium

Paenibacillus polymyxa, which is capable of dissolving the hydrophobic regions of cytoplasmic membranes.[135]

SDS and PmB were effective in disrupting the membrane on the lipid-based sensor yield close to full signal recovery at higher concentrations of lytic agents. Figure 4.6A shows typical cyclic voltammograms obtained from sensing experiments performed in sample solutions containing the highest concentration of SDS and PmB. Sensors tested in solutions containing 1000 ppm SDS (cyan curve) or PmB (red) showed appreciable electrochemical signals that increased over time and reached a maximum signal after 10 and 5 min, respectively. This shows that the membrane was actively disrupted, allowing the redox reporter to access the MSE surface, until a point where the maximum membrane removal possible was reached, leading to a levelling off of the signal. On the other hand, sensors immersed in only 2 mM KFeCy solutions (yellow) did not generate appreciable redox signal even after 60 min immersion in the solution. This was expected, since the synthetic DMPC membrane passivating the electrodes should not be dissolved or ruptured in the presence of the redox reporter molecule which lacks lysing qualities. Further sensing experiments were performed in solutions containing SDS or PmB at concentrations ranging from 1 to 1000 ppm. In all cases, the electrodes were left in the test solutions until the redox signal reached the maximum intensity, and the total charge transferred in the cathodic peak was quantified as detailed above (Figure 4.6B). The time for the sensors to reach the maximum signal varied with concentration and is reported above each bar in the graph. As anticipated, SDS and PmB sensing experiments showed an increase in signal generated as the concentrations of the membrane disruptors increased. In particular, sensors incubated with PmB at a concentration of 1000 ppm showed signals comparable to those generated by bare MSEs (dotted line), showing complete removal of the passivating membrane. The sensors reliably detected PmB down to a concentration of 1 ppm, while SDS was reliably detected at concentrations down to 10 ppm. Since the sensors did not yield reproducible electrochemical signals below these concentrations, the limit of detection for SDS and PmB was established as 10 and 1 ppm, respectively.

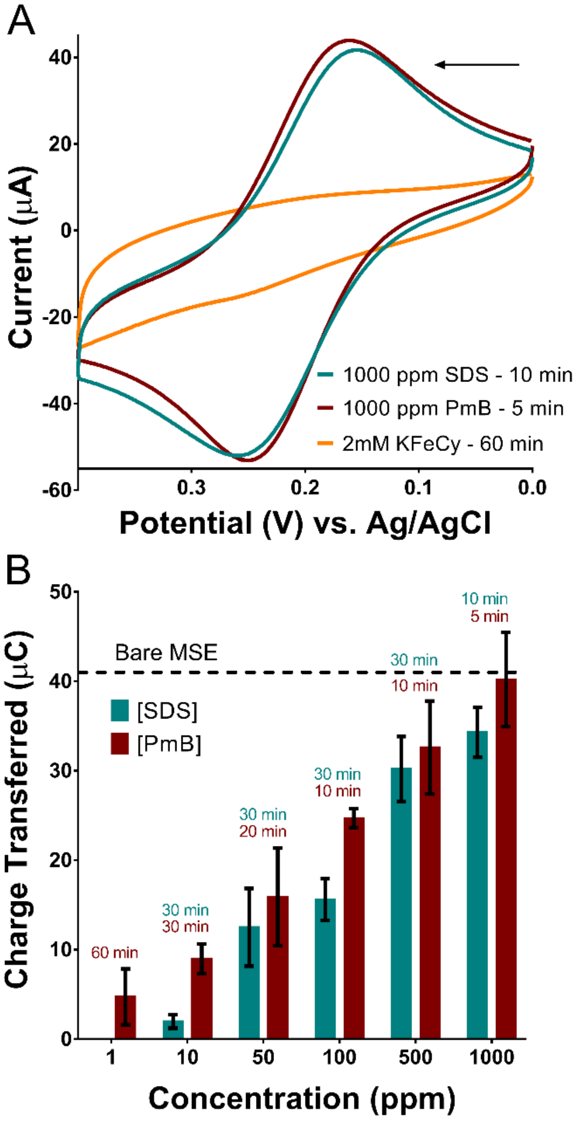

Figure 4.6. Electrochemical sensing of SDS and PmB at concentrations from 1 to 1000 ppm in presence of 2 mM KFeCy redox reporter. **(A)** Cyclic voltammogram overlaying sensing response to SDS (in cyan), PmB (in red), and KFeCy (in yellow). **(B)** Total charge transferred from sensors incubated with solutions containing increasing concentrations of SDS or PmB compared to charge transferred from bare MSEs (black dashed line). Times required for the sensor to reach the maximum electrochemical signal are noted above each bar. Reported charge transfer values are means and error bars are standard deviations of n = 3 replicates.

The DMPC membrane-based sensors produced higher signal and faster response for PmB solutions than for SDS. This increased PmB response can be attributed to the difference in the structure and the membrane disruption mechanism between SDS and PmB. Both molecules rely on electrostatic interactions with the DMPC head group to initiate membrane disruption. In the case of SDS, the binding event initiates the insertion of the hydrophobic tail into the lipid bilayer, which destabilizes and displaces DMPC molecules from the membrane. The insertion and replacement of lipids by SDS also causes an increase in the membrane fluidity. When enough lipids are displaced, the membrane loses its structural integrity resulting in pore formation and ultimately in complete membrane removal (Supplementary Information, Figure 4.S2). The membrane disruption mechanism of PmB, on the other hand, has been described using the carpet and the insertion Barrel-Stave models.[136] Initially, PmB peptides interact electrostatically with the DMPC head groups in the membrane, orienting themselves parallel to its surface and forming aggregates.[137] This leads to thinning of the lipid membrane and compromised lipid bilayer integrity resulting water uptake. This process happens rapidly at high PmB peptide to lipid concentrations, which explains the rapid response time for electrochemical sensing of PmB at 100 to 1000 ppm (Figure 4.6B). The PmB peptides then insert themselves into the membrane to form pores as described by the Barrel-Stave model. Pore formation causes increased membrane instability and increases the water uptake until the membrane is completely disrupted.[138] Furthermore, the head group of PmB consists of 10 amino acids, which makes it much larger than that of SDS, meaning that each PmB molecule can displace more DMPC than SDS and PmB causes greater membrane destabilization than SDS. Thus, the structural properties and mechanism for membrane destabilization explain why a faster response and lower limit of detection are observed for PmB *vs.* SDS. In view of the detection capabilities of this lipid-based platform, we propose that these sensors could provide advantages in sensitivity, turnaround time, affordability, and portability over current gold-standard assays for the detection of membrane disrupting agents.

4.4. CONCLUSION

In this study, we developed an inexpensive electrochemical biosensor for the sensitive and rapid detection of membrane disrupting agents by combining benchtop fabricated MSEs with DMPC phospholipid membranes. DMPC phospholipid membranes were used to passivate the structured electrodes, preventing the interaction of a redox reporter with the electrode surface while the membrane remained intact. When the sensors were incubated with solutions containing a lytic agent (*i.e.*, SDS, PmB), pores formed within the membranes that allowed the reporter molecules to reach the electrode surface and undergo redox cycling, generating an electrochemical signal. We evaluated relevant conditions in the sensor fabrication protocol (*i.e.,* gold wrinkle size, membrane deposition and annealing conditions) and determined that the deposition of DMPC membranes from 200 µg/mL solutions onto MSEs made from 20 nm-thick Au films, followed by annealing at 50°C for 1 hour produced the most reproducible and sensitive biosensors. Using the optimized conditions for biosensor fabrication, SDS and PmB were detected within minutes down to concentrations of 10 and 1 ppm, respectively, highlighting the excellent sensitivity afforded by the MSEs. This novel lipid-based electrochemical biosensing platform offers fast detection times, low cost, reproducibility, and represents a first step towards the realization of Membrane-on-Chip devices with potential for future applications in diagnostics targeted against infectious bacteria, field testing for harmful pesticides, and antimicrobial drug testing.

Acknowledgements

SS was partially supported through an OGS award. JMM is the recipient of an Early Researcher Award from the Ontario Ministry of Research and Innovation and holds the Tier 2 Canada Research Chair in Micro- and Nanostructured Materials. MCR is the recipient of an Early Researcher Award from the Ontario Ministry of Research and Innovation and a McMaster University Scholar. Funding from the Natural Sciences and Engineering Research Council of Canada through Discovery Grants to JM-M and MCR is gratefully acknowledged. This research made use of instrumentation from the Canadian Centre for Electron Microscopy and Biointerfaces Institute at McMaster University.

REFERENCES

(1) Chin, C. D.; Linder, V.; Sia, S. K.; Daar, A. S.; Thorsteinsdottir, H.; Martin, D. K. Lab-on-a-Chip Devices for Global Health: Past Studies and Future Opportunities. *Lab Chip* **2007**, *7* (1), 41–57. https://doi.org/10.1039/B611455E.

(2) Gubala, V.; Harris, L. F.; Ricco, A. J.; Tan, M. X.; Williams, D. E. Point of Care Diagnostics: Status and Future. *Anal. Chem.* **2012**, *84* (2), 487–515. https://doi.org/10.1021/ac2030199.

(3) Yager, P.; Domingo, G. J.; Gerdes, J. Point-of-Care Diagnostics for Global Health. *Annu. Rev. Biomed. Eng.* **2008**, *10* (1), 107–144. https://doi.org/10.1146/annurev.bioeng.10.061807.160524.

(4) Mabey, D.; Peeling, R. W.; Ustianowski, A.; Perkins, M. D. Diagnostics for the Developing World. *Nat. Rev. Microbiol.* **2004**, *2* (3), 231–240. https://doi.org/10.1038/nrmicro841.

(5) Martinez, A. W.; Phillips, S. T.; Whitesides, G. M.; Carrilho, E. Diagnostics for the Developing World: Microfluidic Paper-Based Analytical Devices. *Anal. Chem.* **2010**, *82* (1), 3–10. https://doi.org/10.1021/ac9013989.

(6) Yager, P.; Edwards, T.; Fu, E.; Helton, K.; Nelson, K.; Tam, M. R.; Weigl, B. H. Microfluidic Diagnostic Technologies for Global Public Health. *Nature* **2006**, *442* (7101), 412–418. https://doi.org/10.1038/nature05064.

(7) Yager, P.; Domingo, G. J.; Gerdes, J. Point-of-Care Diagnostics for Global Health. *Annu. Rev. Biomed. Eng.* **2008**, *10*, 107–144. https://doi.org/10.1146/annurev.bioeng.10.061807.160524.

(8) Soper, S. A.; Brown, K.; Ellington, A.; Frazier, B.; Garcia-Manero, G.; Gau, V.; Gutman, S. I.; Hayes, D. F.; Korte, B.; Landers, J. L.; et al. Point-of-Care Biosensor Systems for Cancer Diagnostics/Prognostics. *Biosens. Bioelectron.* **2006**, *21* (10), 1932–1942. https://doi.org/10.1016/j.bios.2006.01.006.

(9) Ahmed, M. U.; Saaem, I.; Wu, P. C.; Brown, A. S. Personalized Diagnostics and Biosensors: A Review of the Biology and Technology Needed for Personalized Medicine. *Crit. Rev. Biotechnol.* **2014**, *34* (2), 180–196. https://doi.org/10.3109/07388551.2013.778228.

(10) Engla, N. E. W. New Engla Nd Journal. *Perspective* **2010**, *363* (1), 1–3. https://doi.org/10.1056/NEJMp1002530.

(11) Gracias, K. S.; McKillip, J. L. A Review of Conventional Detection and Enumeration Methods for Pathogenic Bacteria in Food. *Can. J. Microbiol.* **2005**, *50* (11), 883–890. https://doi.org/10.1139/w04-080.

(12) Kim, T.-H.; Park, J.; Kim, C.-J.; Cho, Y.-K. Fully Integrated Lab-on-a-Disc for Nucleic Acid Analysis of Food-Borne Pathogens. *Anal. Chem.* **2014**, *86* (8), 3841–3848. https://doi.org/10.1021/ac403971h.

(13) Yetisen, A. K.; Akram, M. S.; Lowe, C. R. Paper-Based Microfluidic Point-of-Care Diagnostic Devices. *Lab Chip* **2013**, *13* (12), 2210. https://doi.org/10.1039/c3lc50169h.

(14) Ivnitski, D.; Abdel-hamid, I.; Atanasov, P.; Wilkins, E.; Stricker, S. Application of Electrochemical Biosensors for Detection of Food Pathogenic Bacteria. **2000**, 317–325.

(15) Ahmed, A.; Rushworth, J. V; Hirst, N. A.; Millner, P. A. Biosensors for Whole-Cell Bacterial Detection. **2014**, *27* (3), 631–646. https://doi.org/10.1128/CMR.00120-13.

(16) Ivnitski, D.; Abdel-Hamid, I.; Atanasov, P.; Wilkins, E. Biosensors for Detection of Pathogenic Bacteria. *Biosensors and Bioelectronics*. 1999, pp 599–624. https://doi.org/10.1016/S0956-5663(99)00039-1.

(17) Zhang, S.; Wright, G.; Yang, Y. Materials and Techniques for Electrochemical Biosensor Design and Construction. *Biosens. Bioelectron.* **2000**, *15* (5–6), 273–282. https://doi.org/10.1016/S0956-5663(00)00076-2.

(18) Wang, J. Electrochemical Nucleic Acid Biosensors. *Anal. Chim. Acta* **2002**, *469* (1), 63–71. https://doi.org/10.1016/S0003-2670(01)01399-X.

(19) Wang, J. Electrochemical Glucose Biosensors. *Chem. Rev.* **2008**, *108*, 814–825. https://doi.org/10.1016/B978-012373738-0.50005-2.

(20) Zelada-guille, G. A.; Bhosale, S. V; Riu, J.; Rius, F. X. Real-Time Potentiometric Detection of Bacteria in Complex Samples. **2010**, *82* (22), 9254–9260.

(21) Wu, W.; Zhang, J.; Zheng, M.; Zhong, Y.; Yang, J.; Zhao, Y.; Wu, W.; Ye, W.; Wen, J.; Wang, Q.; et al. An Aptamer-Based Biosensor for Colorimetric Detection of Escherichia Coli O157:H7. *PLoS One* **2012**, *7* (11). https://doi.org/10.1371/journal.pone.0048999.

(22) Vouga, M.; Greub, G. Emerging Bacterial Pathogens: The Past and Beyond. *Clin. Microbiol. Infect.* **2016**, *22* (1), 12–21. https://doi.org/10.1016/j.cmi.2015.10.010.

(23) Kim, H. J.; Bennetto, H. P.; Halablab, M. A. A Novel Liposome-Based Electrochemical Biosensor for the Detection of Haemolytic Microorganisms. *Biotechnol. Tech.* **1995**, *9* (6), 389–394. https://doi.org/10.1007/BF00160823.

(24) Kim, H. J.; Bennetto, H. P.; Halablab, M. A.; Choi, C.; Yoon, S. Performance of an Electrochemical Sensor with Different Types of Liposomal Mediators for the Detection of Hemolytic Bacteria. *Sensors Actuators, B Chem.* **2006**, *119* (1), 143–149. https://doi.org/10.1016/j.snb.2005.12.013.

(25) Alghalayini, A.; Garcia, A.; Berry, T.; Cranfield, C. The Use of Tethered Bilayer Lipid Membranes to Identify the Mechanisms of Antimicrobial Peptide Interactions with Lipid Bilayers. *Antibiotics* **2019**, *8* (1), 12. https://doi.org/10.3390/antibiotics8010012.

(26) Tun, T. N.; Cameron, P. J.; Jenkins, A. T. A. Sensing of Pathogenic Bacteria Based on Their Interaction with Supported Bilayer Membranes Studied by Impedance Spectroscopy and Surface Plasmon Resonance. *Biosens. Bioelectron.* **2011**, *28* (1), 227–231.

https://doi.org/10.1016/j.bios.2011.07.023.

(27) Cranfield, C. G.; Cornell, B. A.; Grage, S. L.; Duckworth, P.; Carne, S.; Ulrich, A. S.; Martinac, B. Transient Potential Gradients and Impedance Measures of Tethered Bilayer Lipid Membranes: Pore-Forming Peptide Insertion and the Effect of Electroporation. *Biophys. J.* **2014**, *106* (1), 182–189. https://doi.org/10.1016/j.bpj.2013.11.1121.

(28) Valincius, G.; Budvytyte, R.; Penkauskas, T.; Pleckaityte, M.; Zvirbliene, A. Phospholipid Sensors for Detection of Bacterial Pore-Forming Toxins. *ECS Trans.* **2014**, *64* (1), 117–124. https://doi.org/10.1149/06401.0117ecst.

(29) Nikolelis, D. P.; Hianik, T.; Krull, U. J. Biosensors Based on Thin Lipid Films and Liposomes. *Electroanalysis* **1999**, *11* (1), 7–15. https://doi.org/10.1002/(SICI)1521-4109(199901)11:1<7::AID-ELAN7>3.0.CO;2-F.

(30) Saem, S.; Zhu, Y.; Luu, H.; Moran-Mirabal, J. Bench-Top Fabrication of an All-PDMS Microfluidic Electrochemical Cell Sensor Integrating Micro/Nanostructured Electrodes. *Sensors (Switzerland)* **2017**, *17* (4). https://doi.org/10.3390/s17040732.

(31) Saem, S.; Abbaszadeh Amirdehi, M.; Greener, J.; Zarabadi, M. P.; Moran-Mirabal, J. M. Microstructured Anodes by Surface Wrinkling for Studies of Direct Electron Transfer Biofilms in Microbial Fuel Cells. *Adv. Mater. Interfaces* **2018**, *5* (13), 1800290. https://doi.org/10.1002/admi.201800290.

(32) Freeman, S.; Harrington, M.; Sharp, J. Lipids, Membranes, and the First Cells. *Biol. Sci.* **2011**, *6* (5), 99–124. https://doi.org/10.1021/mp9000662.Biophysical.

(33) Marquardt, D.; Geier, B.; Pabst, G. Asymmetric Lipid Membranes: Towards More Realistic Model Systems. *Membranes (Basel).* **2015**, *5* (2), 180–196. https://doi.org/10.3390/membranes5020180.

(34) Gabardo, C. M.; Zhu, Y.; Soleymani, L.; Moran-Mirabal, J. M. Bench-Top Fabrication of Hierarchically Structured High-Surface-Area Electrodes. *Adv. Funct. Mater.* **2013**, *23* (24), 3030–3039. https://doi.org/10.1002/adfm.201203220.

(35) Singer, M. M.; Tjeerdema, R. S. Fate and Effects of the Surfactant Sodium Dodecyl Sulfate. **1993**, *133*, 95–96.

(36) Barrett, M. A.; Zheng, S.; Roshankar, G.; Alsop, R. J.; Belanger, R. K. R.; Rheinsta, M. C.; Huynh, C.; Kuc, N. Interaction of Aspirin (Acetylsalicylic Acid) with Lipid Membranes. **2012**, *7* (4), 1–8. https://doi.org/10.1371/journal.pone.0034357.

(37) Alsop, R. J.; Khondker, A.; Hub, J. S.; Rheinstädter, M. C. The Lipid Bilayer Provides a Site for Cortisone Crystallization at High Cortisone Concentrations. *Sci. Rep.* **2016**, *6* (March), 1–10. https://doi.org/10.1038/srep22425.

(38) Bowdish, D. M. E.; Hertz, L.; Rose, M.; Dhaliwal, A.; Wagner, C.; Kaestner, L.; Rheinstädter, M. C.; Verschoor, C. P.; Moran-Mirabal, J. M.; Himbert, S.; et al. The Molecular Structure of Human Red Blood Cell Membranes from Highly Oriented, Solid

Supported Multi-Lamellar Membranes. *Sci. Rep.* **2017**, *7* (1), 1–14. https://doi.org/10.1038/srep39661.

(39) Richter, R.; Mukhopadhyay, A.; Brisson, A. Pathways of Lipid Vesicle Deposition on Solid Surfaces : A Combined QCM-D and AFM Study. *Biophys. J.* **2003**, *85* (5), 3035–3047. https://doi.org/10.1016/S0006-3495(03)74722-5.

(40) Ongena, M.; Jacques, P. Bacillus Lipopeptides: Versatile Weapons for Plant Disease Biocontrol. *Trends Microbiol.* **2008**, *16* (3), 115–125. https://doi.org/10.1016/j.tim.2007.12.009.

(41) Wimley, W. C. R EVIEW. **2010**, *5* (10), 905–917.

(42) Khondker, A.; Dhaliwal, A. K.; Saem, S.; Mahmood, A.; Fradin, C.; Moran-Mirabal, J.; Rheinstädter, M. C. Membrane Charge and Lipid Packing Determine Polymyxin-Induced Membrane Damage. *Commun. Biol.* **2019**, *2* (1), 67. https://doi.org/10.1038/s42003-019-0297-6.

(43) Khondker, A.; Alsop, R. J.; Dhaliwal, A.; Saem, S.; Moran-Mirabal, J. M.; Rheinstädter, M. C. Membrane Cholesterol Reduces Polymyxin B Nephrotoxicity in Renal Membrane Analogs. *Biophys. J.* **2017**, *113* (9), 2016–2028. https://doi.org/10.1016/j.bpj.2017.09.013.

SUPPLEMENTARY INFORMATION

Benchtop fabricated lipid-based electrochemical sensing platform for the detection of membrane-disrupting agents

Sokunthearath Saem,[†] Osama Shashid,[†] Adree Khondker,[‡] Camila Moran-Hidalgo,[†] Maikel C. Rheinstädter,[‡] and Jose Moran-Mirabal[†],*

[†]Department of Chemistry and Chemical Biology, [‡]Department of Physics and Astronomy, McMaster University, Hamilton, Ontario, Canada

* Correspondence: mirabj@mcmaster.ca; Tel.: +1-905-525-9140

Fluorescence microscopy of lipid membranes

For fluorescence imaging of the deposited lipid membranes, DMPC solutions were doped with 1 mol% of Lissamine™ Rhodamine B 1,2-dihexadecanoyl-sn-glycero-3-phosphoethanolamine, triethylammonium salt (LR-DHPE, Invitrogen, Carlsbad, CA, USA) from a 0.25 mg/mL stock solution in chloroform. Fluorescence images were captured using a Nikon Eclipse LV100ND advanced research-grade upright microscope (Nikon, Mississauga, ON, Canada) fitted with a 10x CFI60 Plan Fluor Phase Contrast DLL objective (N.A. 0.3, W.D. 0.16 mm) and excitation/emission filters for Rhodamine dye. Images were taken with a motorized stage at 2 μm z-step size and a high-resolution 3D reconstruction was rendered using the Nikon NIS-Elements Documents software. 3D-reconstructed images were converted to a heat map look-up table using Image-J.

Optical microscopy

White light, bright field electrode images were taken with a Nikon Eclipse LV100ND advanced research-grade upright microscope optical microscope (Nikon, Mississauga, ON, CA) fitted with a 50x TU Plan Fluor air objective (N.A. 0.8, W.D. 1.0 mm), and a Nikon DS-Ri2 Camera with a resolution of 4908×3264 pixel and a pixel-size of 7.3×7.3 μm. The images were 3D reconstructed using NIS-Elements Documents software at a z-step size of 1 μm.

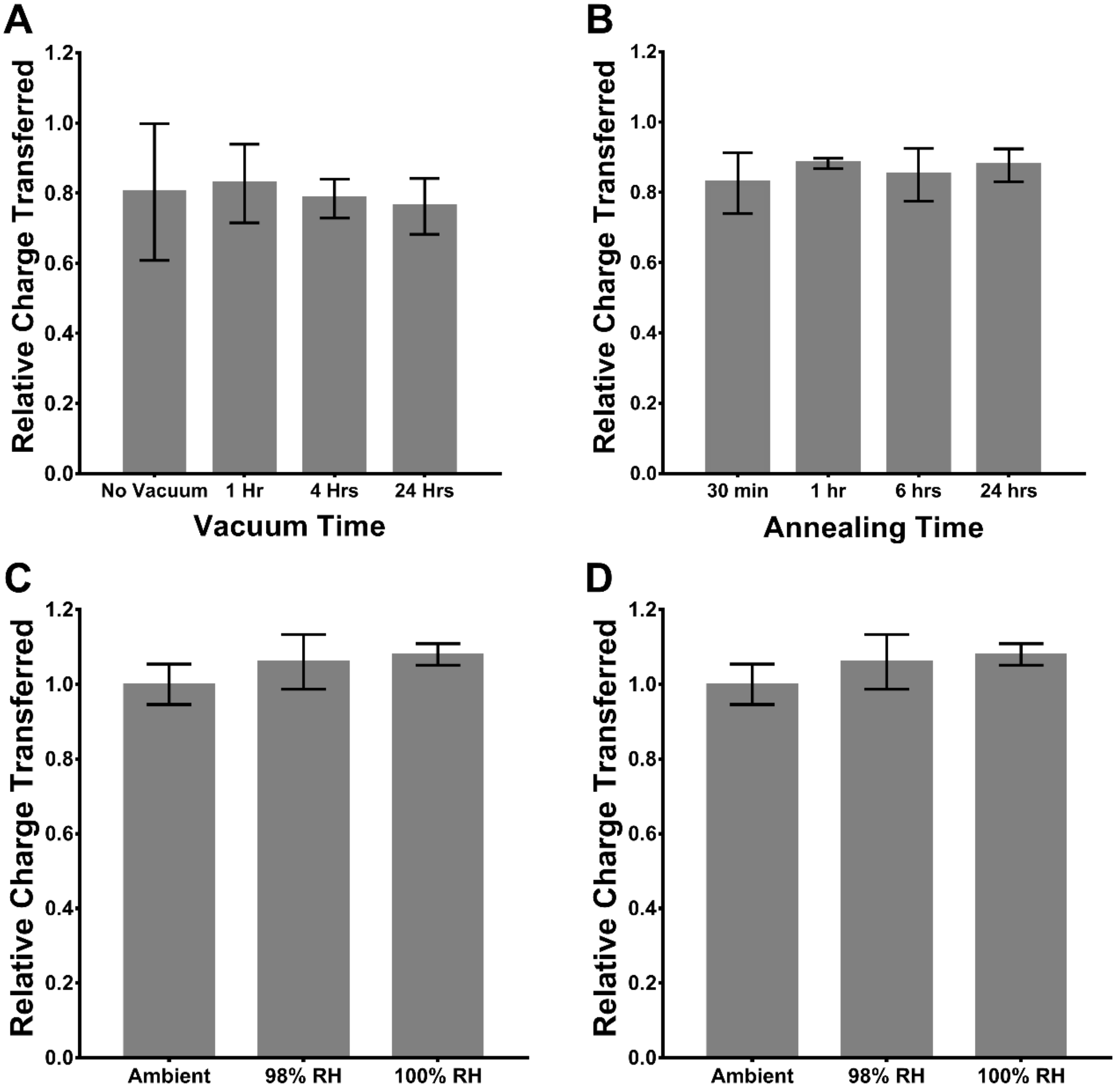

Figure 4.S1. Optimization of vacuum, annealing, relative humidity and temperature for lipid membrane deposition. DMPC films were made on 20 nm MSEs by drop casting 15 µL from a 0.5 mg/mL stock lipid solution. In all cases sensing was performed through CV in 0.1% SDS solutions in presence of 2mM KFeCy redox reporter. All charge transfers are relative to bare Au sensors with no DMPC. **(A)** Relative charge transferred for sensors prepared using solvent evaporation in vacuum for various lengths of time, while keeping 100% RH and 24-hour annealing at 50°C. **(B)** Relative charge transferred for sensors prepared using solvent evaporation in vacuum for 24 hours, and annealing at 100% RH and 50°C over a variable length of time. Trials were also performed on non-annealed electrodes, but signal leakage was observed prior

to exposure to SDS. **(C)** Relative charge transferred for sensors prepared using solvent evaporation in vacuum for 24 hours, and annealing at variable humidity for 24 hours at 50°C. **(D)** Relative charge transferred for sensors prepared using solvent evaporation in vacuum for 24 hours, and 100% RH and 24-hour annealing at variable temperatures.

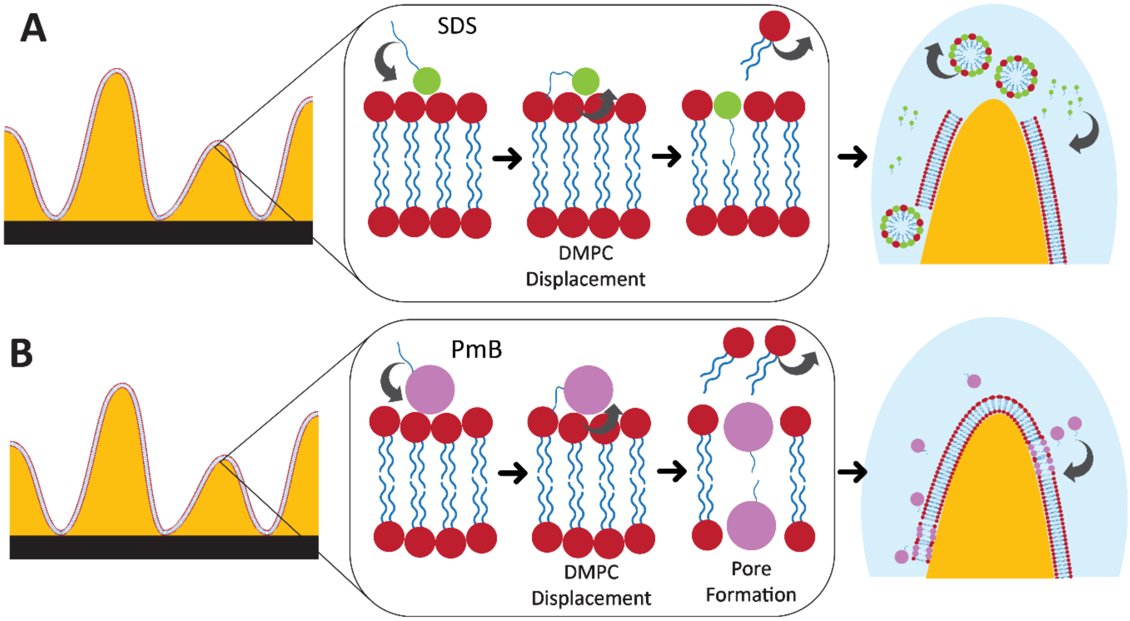

Figure 4.S2. Schematic representation of **(A)** SDS and **(B)** PmB membrane disruption mechanisms.

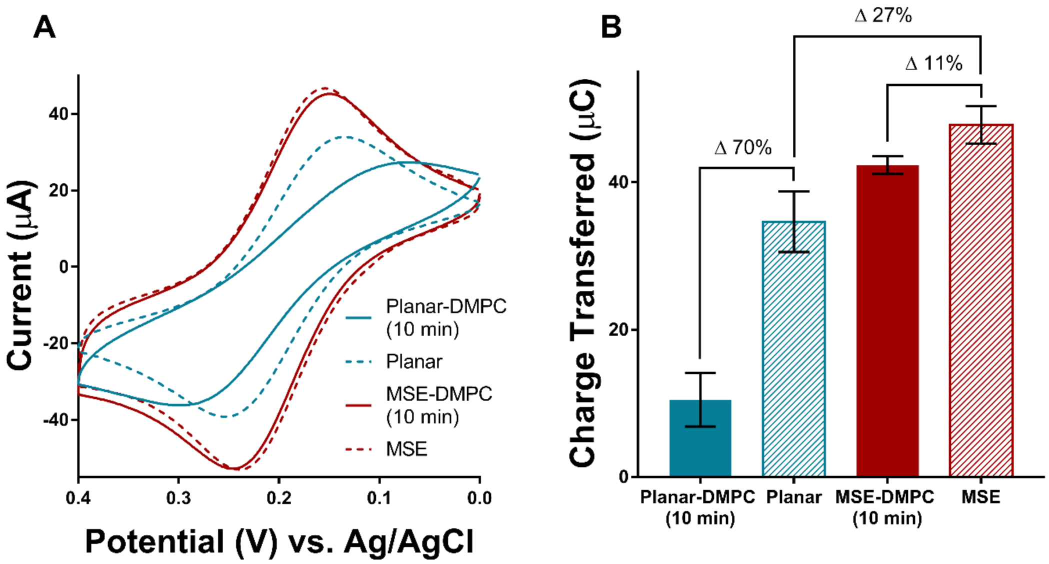

Figure 4.S3. A comparison of signal generation of 20 nm Au planar electrodes (teal) and MSE (maroon) passivated with 0.2 mg/mL DMPC membrane. Cyclic voltammetry was performed in a 1000 ppm SDS and 2 mM KFeCy solution until maximum membrane removal was achieved at 10 min for each device. **(A)** DMPC-MSEs showed full signal recovery at 10 min comparable to clean MSEs, where planar Au electrodes was not able to recover full signal. **(B)** Quantification of CV plots in charge transfer showing signal close to full signal generation from MSE-DMPC devices while planar-DMPC devices only regenerated approximately 30% signal. Furthermore, MSEs showed approximately 27% higher signal output over bare planar Au electrodes, making MSEs the favourable option for high sensitivity electrochemical sensing applications.

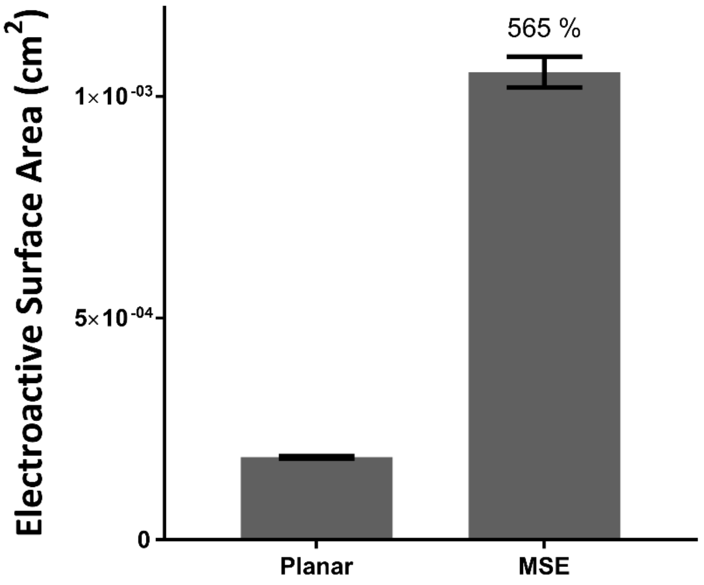

Figure 4.S4. EASA comparison between planar Au electrode and MSEs. The EASA was obtained using CV scanning in a 50 mM H_2SO_4 solution. The MSEs contains improved EASA compared to the planar electrodes allowing for increased sensitivity in electrochemical detection.

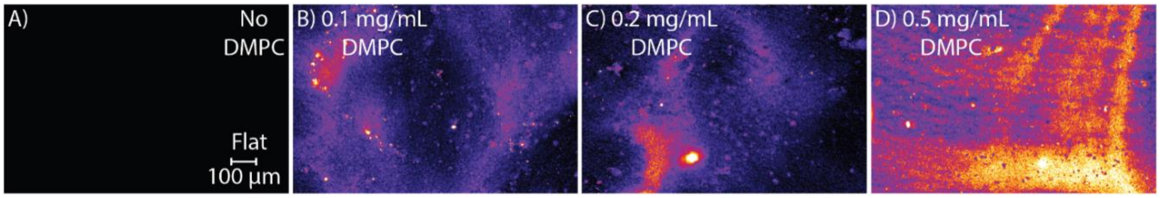

Figure 4.S5. Fluorescence microscopy images of 20 nm-thick MSEs with membranes deposited from **(A)** 0, **(B)** 0.1 mg/mL, **(C)** 0.2 mg/mL, and **(D)** 0.5 mg/mL DMPC solutions.

Chapter 5: Cholesterol Enriched Membrane-based Electrochemical Biosensor for the Detection of Waterborne Lytic Agents

This chapter will be submitted as:

Sokunthearath Saem, Osama Shashid, Nadine Beganovic, and Jose Moran-Mirabal* (2019) Cholesterol Enriched Membrane-based Electrochemical Biosensor for the De-tection of Waterborne Lytic Agents.

Author Contributions: SS and JMM planned the study and analyzed the data. SS fabricated the devices and performed electrochemical sensing. OS performed humidity optimization experiments and lytic sensing. NB performed the Bradford Assay for protein concentration determination.

Cholesterol Enriched Membrane-based Electrochemical Biosensor for the Detection of Waterborne Lytic Compounds

Sokunthearath Saem, Osama Shashid, Nadine Beganovic, and Jose Moran-Mirabal*

Department of Chemistry and Chemical Biology, McMaster University, Hamilton, Ontario, Canada

ABSTRACT

The prevalence of waterborne pollutants and pathogens in developing nations present a significant health risk to local residents. Compounds that disrupt the cell membrane are of particular concern as affected individuals have severe reactions that can result in death. Currently, tests for membrane-disrupting agents (i.e. lytic agents) are performed offsite, require expensive equipment or sample preparation, and are time-consuming. Affordable, robust, and sensitive sensing alternatives are needed to make the quantitative determination of harmful lytic agents accessible to resource-limited nations. Here, we studied the effect of cholesterol as a dopant molecule on the stability of lipid membranes deposited on wrinkled gold microstructured electrodes (MSEs) and the ability of the membranes to serve as platforms to sense cholesterol-dependent hemolytic agents. Supported biomimetic membranes composed of cholesterol and 1,2-dimyristoyl-*sn*-glycero-3-phosphocholine (DMPC) were deposited on the MSEs as passivation layers to prevent the interaction of redox reporter molecules in solution with the electrode surface. Upon exposure to lytic agents, such as sodium dodecyl sulfate (SDS), polymyxin-B (PmB), or pneumolysin (PLY), the membranes were disrupted and exposed the MSE surface, allowing an electrochemical signal to be generated. Cyclic voltammetry showed that addition of cholesterol to DMPC membranes increased the membrane stability against SDS and PmB, but not against PLY. Sensing at different concentrations of the lytic agents yielded limits of detection for the cholesterol rich membrane-based biosensors of 500, 1, and 0.6 ppm for SDS, PmB, and PLY, respectively. This study demonstrates the viability of membrane-based electrochemical biosensors to quantitatively detect lytic agents in solution with the potential to accommodate membranes of increasing complexity for sensitive and selective membrane-on-a-chip sensing.

5.1. INTRODUCTION

Waterborne pesticides and pathogens present a common risk in many parts of the world and are most prevalent in developing countries. Compounds that disrupt the cell membrane (i.e. lytic compounds) such as proteins expressed from infectious bacteria[1–5] and insecticides[6–8] are of particular concern because they can cause hemolysis, or the rupturing of red blood cells. Analytical techniques like HPLC and blood culture test are typically used to detect lytic compounds. Although quite sensitive, they require expensive equipment, highly specialized technicians, and have long turnaround times. This makes accessibility to high quality analytical tests challenging since testing is primarily performed offsite. Therefore, novel medical devices that are affordable, sensitive, reproducible, robust, portable, and easy to operate are needed. A popular platform for the detection of targeted analytes are electrochemical biosensors (ECBs).[9] Inspired by the first commercial enzyme-based glucose sensor by Leland C. Clark Jr., new ECBs are focused on the detection of other relevant analytes such as pathogenic bacteria,[10–12] cocaine,[13–15] or methamphetamine.[16,17] ECBs hold promise for use in point-of-care diagnostics due to their ease of miniaturization, proven sensitivity, rapid detection, operational simplicity, and versatility.[18–24]

The cell plasma membrane is a complex bilayer structure primarily made of phospholipids, proteins that facilitate cross-membrane transport and cell communication, carbohydrates for cell-to-cell recognition, and cholesterol to provide membrane plasticity and increased integrity. The plasma membrane protects the cell from its surroundings and regulates small molecule transport between the intracellular and extracellular environment to ensure cell viability.[25,26] Therefore, perturbations that result in membrane pore formation or rupture (i.e. lysis) could eventually lead to cell death. Their intrinsic attributes make lipid membranes interesting components for use in ECBs as a biological recognition elements. Membrane rupture by lytic compounds can be exploited to develop membrane-based ECBs. Previous studies have used the rupture of vesicles loaded with redox reporters to detect lytic compounds via amperometric sensing.[27,28] Others have used polymer supported lipid bilayers on planar conductive surfaces together with electrochemical impedance spectroscopy (EIS) to detect lytic compounds.[29–31] Although effective, the use of EIS is not amenable to fast portable detection, as the technique requires complex equipment and sophisticated data analysis to achieve quantitative results. Furthermore, the use of planar conductive surfaces presents a miniaturization challenge as reducing the electrode size would result in a reduction in signal and biosensor sensitivity.

Over the past decade, our group has used the thermal shrinking of pre-stressed polystyrene as an inexpensive benchtop method to wrinkle thin metallic films and miniaturize electrode designs.[32–36] The wrinkling of gold electrodes using this approach results in a six-fold enhancement of the electroactive surface area (EASA) over planar electrodes with a similar geometrical footprint, which translates into higher current densities per unit area and therefore increased sensitivity in ECBs. Recently, we reported the integration of stable biomimetic 1,2-dimyristoyl-*sn*-glycero-3-phosphocholine (DMPC) membranes on wrinkled microstructured electrodes (MSEs) without the need of synthetic polymer supports.[37] These lipid membrane-MSE hybrids were used in proof-of-concept experiments to detect membrane disruption, establishing them as viable platforms for the development of membrane-on-chip ECBs (MoC-ECBs). Yet, the model membranes used in this study lacked the complexity of plasma membranes, which could alter the response of the MoC-ECBs and their selectivity towards lytic agents. Therefore, to develop biosensors that more accurately mimic the plasma membrane response, the complexity of the MoC-ECB platform needs to be increased by incorporating other membrane-bound molecules.

Cholesterol is one of the main constituents of animal cell membranes, where it modulates the membrane fluidity in a composition-dependent fashion and tunes the membrane permeability.[38–41] In mammalian cell membranes, cholesterol can be found at concentrations ranging from 20 to 45 mol%, with an average of ~30 mol% for most mammalian cells.[42,43] Some lytic compounds have been found to require the presence of cholesterol to initiate the formation of pores in the cell membrane.[1–4,44] For example, pneumolysin (PLY), a virulence factor expressed by the gram-positive bacteria *Streptococcus pneumoniae,* is known to lyse red blood cell (RBC) membranes in a cholesterol-dependent fashion that can be inhibited by the addition of exogenous cholesterol.[1,2,45,46] The presence of PLY in clinical samples (e.g., urine, blood, sputum) is indicative of *S. pneumoniae* infection, which makes cholesterol an important component for incorporation into MoC-ECBs.

Here, we fabricated MoC-ECBs with supported DMPC membranes containing increasing cholesterol content. We studied the sensor response to three lytic compounds: the anionic surfactant sodium dodecyl sulfate (SDS), an antimicrobial drug known to cause lysis in phospholipid membranes (Polymyxin-B, PmB), and a hemolytic protein isolated from *Streptococcus pneumoniae* (pneumolysin, PLY). We found that cholesterol stabilized the supported membrane against SDS and PmB, but not against PLY. These lytic factors could be quantitatively detected, with limits of detection of 500 ppm for SDS, 1 ppm for PmB, and 0.6 ppm for PLY. By further introducing complexity to the membrane-based sensors (e.g. proteins and carbohydrates) their specificity towards pathogen derived lytic agents could be improved. We anticipate that this supported membrane on a chip platform presents a viable option for the quantitative detection of lytic compounds in solution, translatable to other relevant clinical samples.

5.2. MATERIALS & METHODS

5.2.1. Microstructured Electrode (MSE) Fabrication

The benchtop fabrication and characterization of MSEs has been previously reported in detail.[33,36] Briefly, polystyrene (PS) sheets (Graphix Shrink Film, Graphix, Maple Heights, OH, USA) were washed with isopropanol (IPA), ethanol (EtOH), and ultrapure $18.2\ \mathrm{M\Omega \cdot cm}$ water for 5 min each under orbital agitation at 60 rpm and dried under a nitrogen stream. Adhesive vinyl (FDC-4300, FDC graphic films, South Bend, IN, USA) electrode masks were cut using a Robo Pro CE5000-40-CRP blade cutter (Graphtec America Inc., Irvine, CA, USA) equipped with a CB09UA blade. The vinyl masks were subsequently adhered onto the clean PS to define the electrode shape. A Torr Compact Research Coater CRC-600 manual planar magnetron sputtering system (New Windsor, NY, USA) was then used to deposit gold (99.999% purity, LTS Chemical Inc., Chestnut Ridge, NY, USA) on the PS substrates at a rate of 0.5 Å/s, to a total thickness of 50 nm. Following Au deposition, the vinyl masks were peeled-off from the substrate, revealing patterned electrodes. The electrodes were placed in an oven at 160ºC for 5 min to induce thermal shrinking of the PS substrate resulting in micro-structured electrodes (MSE).

5.2.2. Fabrication of Membrane-on-Chip Electrochemical Biosensors (MoC-ECBs)

The MoC-ECB benchtop fabrication process is shown in Figure 5.1. Briefly, 1 mg/ml DMPC (1,2-dimyristoyl-sn-glycero-3-phosphocholine, Avanti Polar Lipids Inc, Alabaster, AL, USA) and 0.5 mg/ml cholesterol (Avanti Polar Lipids Inc, Alabaster, AL, USA) stock solutions were made using a 1:1 mixture of chloroform and 2,2,2-trifluoroethanol ($CHCl_3$:TFE) as a solvent. The two stock solutions were mixed at the appropriate ratios and diluted to obtain 0.5 mg/ml DMPC:Cholesterol solutions with 0, 15, 30, and 50 mol% cholesterol content. The previously prepared MSEs were rinsed with IPA and plasma treated (30 sccm air flow, 600 mTorr) using a PDC expanded oxygen plasma cleaner (Harrick, Ithaca, NY, USA) operated at high power setting (30 W). Then, an adhesive vinyl drop-cast mask was applied to the MSEs and they were heated to 50ºC on a hotplate. The DMPC:Cholesterol solutions were drop-cast onto the circular MSE pad at 15 µl per electrode and kept on the hotplate for 5 min. Following lipid deposition, the MoC-ECBs were placed in a humidified glass chamber to achieve 100% relative humidity (RH) and annealed at 50ºC in an oven for 1 hour. After annealing, the MoC-ECBs were fully passivated and ready for use in electrochemical sensing experiments.

5.2.3. Recombinant pneumolysin expression, purification, and red blood cell lysis

Pneumolysin (PLY) expression

E. coli BL21(DE3) pET33b(+)-rPly was cultured in 10 – 20 mL lysogeny broth (LB) medium containing 50 µg/mL Kanamycin overnight at 37ºC and under constant agitation at 225 rpm. The optical density at 600 nm (OD_{600}) was determined, followed by a dilution of the overnight culture in fresh LB medium to an OD_{600} of 0.05. The diluted sample was cultured at 37ºC and under constant agitation until an OD_{600} of 0.4 – 0.8 was reached. PLY expression was induced by adding to the culture isopropyl β-d-1-thiogalactopyranoside (IPTG) to a final concentration of 0.5 mM. The culture was further grown for an additional 3 hours at 37ºC and 225 rpm. The final culture was pelleted at 4000 rpm for 10 min and 4ºC. The supernatant was discarded and the pellet was frozen at -80ºC until the purification step.

Cell disruption and protein purification

Cell pellets were suspended in 20 mL equilibrium buffer (1xPBS with 10 mM Imidazole) and the cells were disrupted using a cell disruptor (Constant Systems Ltd, Daventry, UK). The cells were collected in a 50 mL tube and placed on ice. The cell debris was spun down at 10,000 – 13,000 rpm for 30 min at 4°C. The protein was purified from the supernatant via FPLC using a His-Trap column at 4°C. SDS PAGE was performed to extract only the 53 kDa PLY. Briefly, samples containing PLY were loaded onto SDS gels and ran at 200 V for 45 min at room temperature. The subsequent gels were rinsed with water and 53 kDa PLY fractions were pooled into a 50 mL tube and dialysis was performed overnight at 4°C. Aliquots of 100 µL of PLY were stored at -80°C.

5.2.4. Sodium Dodecyl Sulphate (SDS), Polymyxin-B (PmB), and Pneumolysin (PLY) Solution Preparation

All sensing solutions were prepared in 1x PBS buffer (137 mM NaCl, 2.7 mM KCl, 8 mM Na_2HPO_4, and 2 mM KH_2PO_4, pH = 7.4, Sigma-Aldrich, Oakville, ON, Canada) made with ultrapure water. Potassium ferrocyanide (KFeCy – $K_4[Fe(CN)_6]\cdot 3H_2O$, Sigma-Aldrich, Oakville, ON, Canada) served as a redox reporter molecule, and was used at 2mM concentration in 1x PBS. The desired amount of sodium dodecyl sulfate (SDS, Sigma-Aldrich, Oakville, ON, Canada) or polymyxin B (PmB) (Sigma-Aldrich, Oakville, ON, Canada) was added to the KFeCy solutions to achieve the target concentrations. PLY stock solution (54 µg/mL) was thawed and diluted to the desired working concentration in the KFeCy solution.

5.2.5. Electrochemical Sensing

We used cyclic voltammetry (CV) as the sensing technique to monitor membrane disruption in the presence of SDS, PmB or PLY. CV measurements were done using a CHI600E electrochemical workstation (CH Instruments, Austin, TX, USA) where the MoC-ECB was used as the working electrode (WE), a platinum wire auxiliary electrode (AE), and an Ag/AgCl reference electrode (RE). The CV experiments were performed with 0-0.4 V sweeps, at a scan rate of 0.1 V/s and for 10 segments. The MoC-ECBs were rinsed with Milli-Q water and dipped into a 15 ml working solution along with the AE and RE. A background scan was performed in neat 2 mM KFeCy solution to ensure that the electrodes did not contain defective membranes. Following this step, the MoC-ECBs were placed in the working solution of interest (i.e. containing desired amounts of SDS, PmB or PLY). To recycle the chips, any leftover DMPC:Cholesterol on the MoC-ECBs was completely removed using a series of 5 min (each) solvent exposure to IPA, EtOH, and ultrapure water, followed by drying under a N_2 stream. The clean MSEs were stored in plastic dishes and reused to fabricate new MoC-ECBs.

5.3. RESULTS & DISCUSSION

5.3.1. Benchtop Fabrication of MoC-ECBs

The most common barriers to accessibility to clinical analytical techniques are cost, portability, lack of operational knowledge, sensitivity, robustness, and reproducibility. The MoC-ECB was designed with these variables in mind. To increase the sensitivity, portability, and reduce cost we used a previously reported simple benchtop fabrication approach to produce the MSEs (Figure 5.1A).[32,33] The MoC-ECBs were fabricated using commercial pre-stressed PS sheets as the substrate. The thermally induced shrinking of PS reduced the dimensions of the flat circular working Au electrode pad from 12.5 to 5 mm in diameter. The shrinking process wrinkled the electrodes and resulted in a 6-fold increase in electrochemical active surface area. This makes MSEs ideal for use in portable biosensing applications where increased sensitivities, comparable to laboratory instruments is desired. MSE devices were fabricated from 50 nm-thick films to ensure device robustness for transport and device reusability, resulting in fabrication costs of $0.20 per MSE.

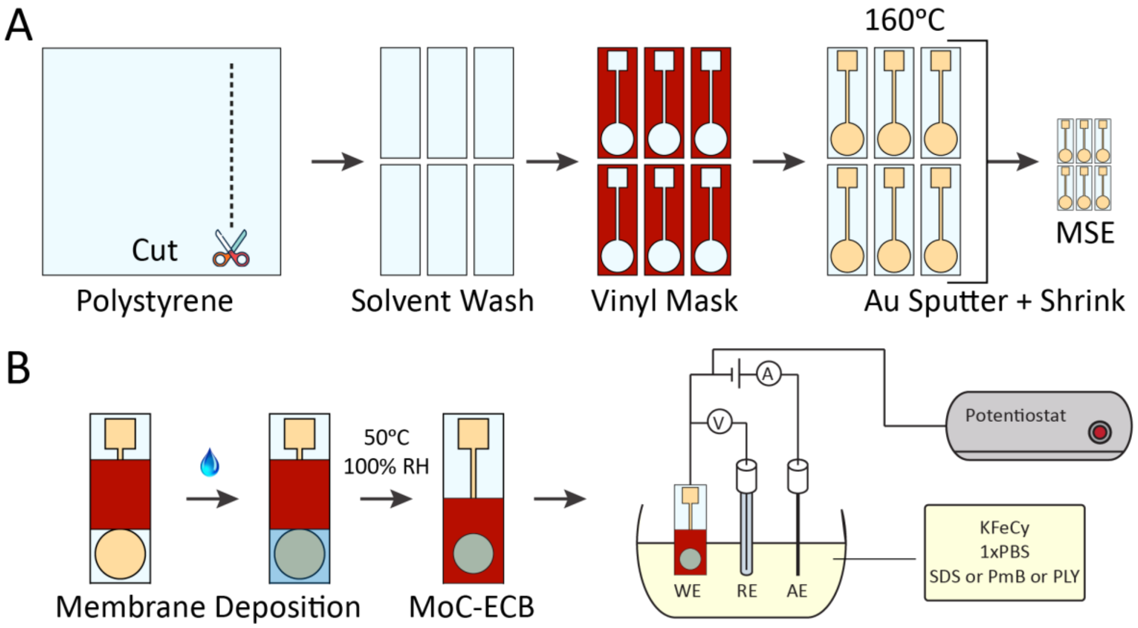

Figure 5.1. Benchtop fabrication and electrochemical sensing configuration. **(A)** PS sheets were cut and cleaned with IPA, EtOH, and H_2O. A vinyl mask was placed on the substrate and 50 nm Au was sputtered onto it. The mask was removed to reveal the patterned electrode, which after shrinking at 160°C yielded an MSE. **(B)** MSEs were masked and a lipid solution was deposited on the working pad followed by annealing at 50°C and 100% RH. The drop-cast mask was replaced with a sensing mask to control the exposed surface. The MoC-ECB was placed in a sensing solution containing 2 mM KFeCy and SDS, PmB, or PLY at a prescribed concentration. CV was used for all sensing experiments.

We have previously shown that to achieve the most reproducible and sensitive ECBs, the membranes deposited should be as uniform and stable as possible.[37] Therefore, the membrane annealing protocol was optimized using DMPC:Cholesterol mixtures containing 30% cholesterol. MoC-ECBs were prepared by annealing the membrane for 1 hour at 50°C in ambient or 100% RH. We observed that both annealing treatments produced membranes that completely passivated the electrodes, as there was no leak current generated when the electrodes were immersed in solutions containing the redox reporter KFeCy. The ECBs were then purposely disrupted by exposure to solutions containing a high concentration (500 ppm) of SDS and 2mM KFeCy, and the CV signal evolution was monitored over time. This experiment was aimed at evaluating the uniformity of the passivating membrane. After a 20-minute incubation, ECBs annealed at 100% RH generated 50% of the signal produced by bare MSEs, while those annealed at ambient humidity produced 70% (Figure 5.S1). Additionally, devices prepared at 100% RH produced much lower variance. This suggests that the membranes annealed at 100% RH are more stable and uniform than those prepared at ambient conditions. Our interpretation is that the increased water content in a humid environment during the annealing step allowed the cholesterol and DMPC molecules to have increased mobility and form more uniformly packed membranes. This is significant because selecting the optimal annealing conditions enables us to use the minimal amount of DMPC:Cholesterol solution to passivate the electrode surface, which translates into faster signal generation from the membrane layer during sensing.

5.3.2. Biosensing Mechanism

Unlike many existing ECBs that rely on anchored biomolecules such as aptamers, antibodies, and enzymes to capture the target of interest, MoC-ECBs use a membrane disruption process (i.e. lysis) coupled with a redox active reporter molecule in solution to generate a quantitative signal in the presence of lytic compounds.[37] In typical CV experiments, a voltage is swept to oxidize and reduce the species of interest and the current measured at the WE (in this case the MSE) is proportional to the scan rate (V/s), redox molecule concentration, and electrode surface area. In the case of a bare electrode, 100% of electrons generated via the redox process flow through the electrode. However, once the surface of the electrode has been blocked by the DMPC:Cholesterol membrane layer, no charge can flow between the redox molecule and the electrode, which reduces the measurable signal practically to zero. In the presence of a lytic compound (e.g. SDS, PmB or PLY), the membrane is progressively disrupted and eroded, producing regions of exposed electrode surface that allow charge to be transferred from the reporter to the electrode. The signal generated is proportional to the concentration of the lytic compound. Through this sensing mechanism, MoC-ECBs are capable of rapidly and efficiently detecting factors that cause membrane disruption.

5.3.3. Cholesterol Effect on Membrane Stability

To determine the impact that cholesterol has on the sensing membrane stability, we fabricated MoC-ECBs with membranes where the DMPC solution was doped with increasing amounts of cholesterol, up to a maximum of 50 mol%. The ECBs were then challenged with solutions containing 500 ppm SDS and PmB, and CV was used to obtain the relative charge transferred (normalized to bare MSEs) over time (Figure 5.2). In all instances, PmB was more efficient at disrupting the DMPC:Cholesterol membranes than SDS, as evidenced by the signal obtained for PmB being higher and the time required to reach the maximum signal (10 minutes) being half of that for SDS. This indicates that PmB, an antibiotic that is used to treat bacterial infections, can still disrupt cholesterol-containing membranes that mimic the those from eukaryotes and is more efficient at doing so than SDS. This can be explained by the fact that in the presence of cholesterol, PmB has increased insertion into the membrane over SDS, which leads to larger water uptake and eventual rupture in the membrane.[47] Furthermore, the larger head groups found in PmB can interact laterally with each other to form clusters and disturb the DMPC packing resulting in an increased water permeation into the membrane core. In contrast, SDS is a surfactant molecule with a much smaller head group compared to PmB, where a larger amount of SDS is needed to destabilize the membrane and cause membrane rupture.

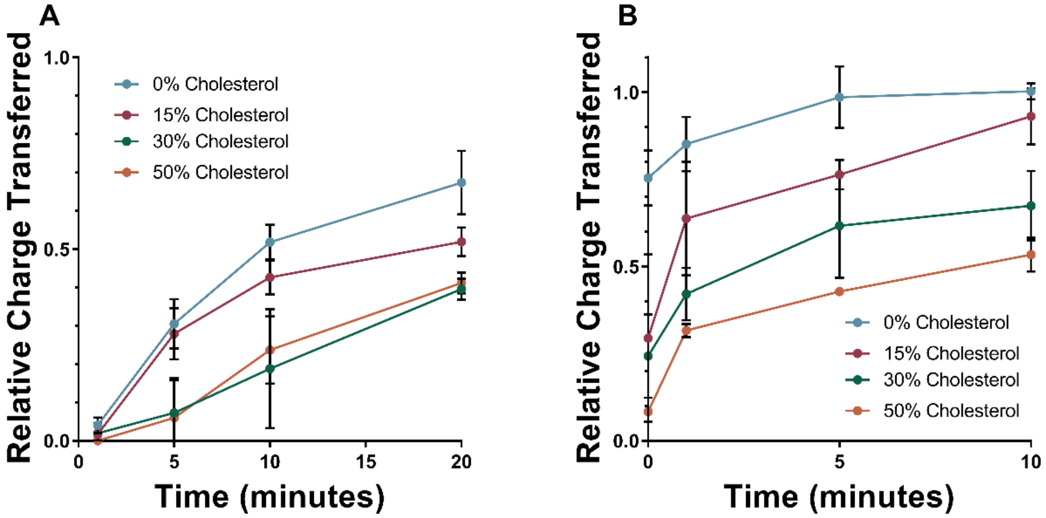

Figure 5.2. Relative charge transferred plot of MoC-ECBs containing 0 – 50 mol% cholesterol monitored in **(A)** 500 ppm SDS solution over 20 min and **(B)** 500 ppm PmB over 10 min. Points represent means and error bars are standard deviations of N = 3 replicate experiments.

It was also observed that when exposed to either SDS or PmB, the presence of cholesterol resulted in lower signals, suggesting that the membranes become more stable and less susceptible to disruption. In the presence of SDS, as the cholesterol concentration was varied from 0 to 50 mol%, the relative charge transferred at 20 minutes was reduced from 68% to 40% (Figure 5.2A). Similarly, when exposed to PmB, an increase in cholesterol content from 0 to 50 mol% resulted in a proportional reduction of the relative charge transferred at 10 minutes from 100% to 52% (Figure 5.2B). These results show that the presence of cholesterol greatly affects the ability of SDS and PmB to solubilize or form pores within the phospholipid membranes. This is consistent with previous reports on the role of cholesterol in membranes, where it serves as a membrane-stabilizing molecule by introducing conformational ordering in lipid chains.[38,47] DMPC is a lipid that exists in the ordered gel phase at room temperature. In the gel phase, DMPC membranes are stiffer and exhibit minimal lateral mobility due to the high van der Waals interactions between the fully saturated alkyl tails leading to a high degree of packing.[48] In the presence of increasing cholesterol, the DMPC membrane transitions into a liquid-ordered phase that exhibits a mixture of solid-like properties of the gel phase but also contains increased lateral mobility like that of the liquid-disordered phase. The increased in membrane fluidity has been shown to minimize membrane deformation upon contact with lytic agents in addition to reducing membrane indentation and thinning.[47] Additionally, high cholesterol concentrations (>20%) have been proposed to increase membrane thickness due to the change in cholesterol tilt angle from high to low compared to the bilayer normal.[38] This increase in membrane thickness could help to explain why DMPC membranes with higher cholesterol content are harder to rupture as seen in the lower signal production in Figure 5.2.

5.3.4. Sensing with MoC-ECBs

Sensing and determining the limits of detection (LOD) for MoC-ECBs when exposed to membrane disrupting agents is important to evaluate their overall sensitivity and potential applicability. Since MoC-ECBs containing different amounts of cholesterol showed similar signal evolution over time (i.e. membrane disruption kinetics), we chose to use membranes with 30 mol% cholesterol for sensing. This concentration is in line with the average cholesterol concentrations found in eukaryote membranes[42,43] and would therefore more closely resemble them. To determine the LOD, sensors were incubated for up to 60 minutes with solutions containing 2 mM KFeCy and SDS or PmB at concentrations ranging from 100 to 5000 ppm and 1 to 500 ppm, respectively. Based on dynamic light scattering (DLS) measurements, the critical micelle concentration (CMC) of SDS and PmB is 2200 ppm (7.5 mM) and 2300 ppm (1.6 mM), respectively (Figure 5.S2). Thus, the concentrations of SDS and PmB used in the sensing experiments were, with the exception of the 5000 ppm SDS treatment, below the CMC and these molecules interacted with the biomimetic membranes in monomeric form.

Consistent with the results from the cholesterol concentration series, PmB was more effective in disrupting the DMPC:Cholesterol membrane than SDS (Figure 5.3). The MoC-ECB sensors were able to detect concentrations of PmB that were two orders of magnitude lower than for SDS. In particular, the LOD for PmB was determined to be 3 ppm at 1min whereas SDS was 200 ppm at 10 minutes of incubation. The LOD for these sensing experiments was determined as the lowest concentration of the molecule at which a signal could be seen in the cyclic voltammogram and the current peak could be integrated. It must be noted that sensors exposed to SDS at 100 ppm did not produce any signal even after 60 min of incubation in the sensing solution. As described above, the difference in sensitivity was attributed to the larger size of the PmB molecules and the different modes of action through which they destabilize the membrane. More specifically, both SDS and PmB will first interact electrostatically with the head groups of the DMPC molecules in membrane, which facilitates the insertion of their hydrophobic tail into the membrane. This has been previously observed in XRD experiments supported by molecular dynamics simulations.[47,49] This process leads to increased membrane curvature and permeability, which continues until the membrane is completely dissolved. In the case of PmB, the widely accepted carpet model involves a charge-induced parallel association between the PmB molecule and the zwitterionic DMPC head group.[47,49] This continued association causes increased stress on the membrane, which results in rapid membrane disruption. In addition, the Barrel-Stave model predicts that PmB inserts its hydrophobic tail into the membrane bilayer leading to pore formation and resulting in membrane leakage.[47,49] It has been proposed that a mixture of pore formation and dissolution of phospholipids occur when PmB interacts with phospholipid membranes, whereas for SDS dissolution is the only mode of membrane disruption.[47,50]

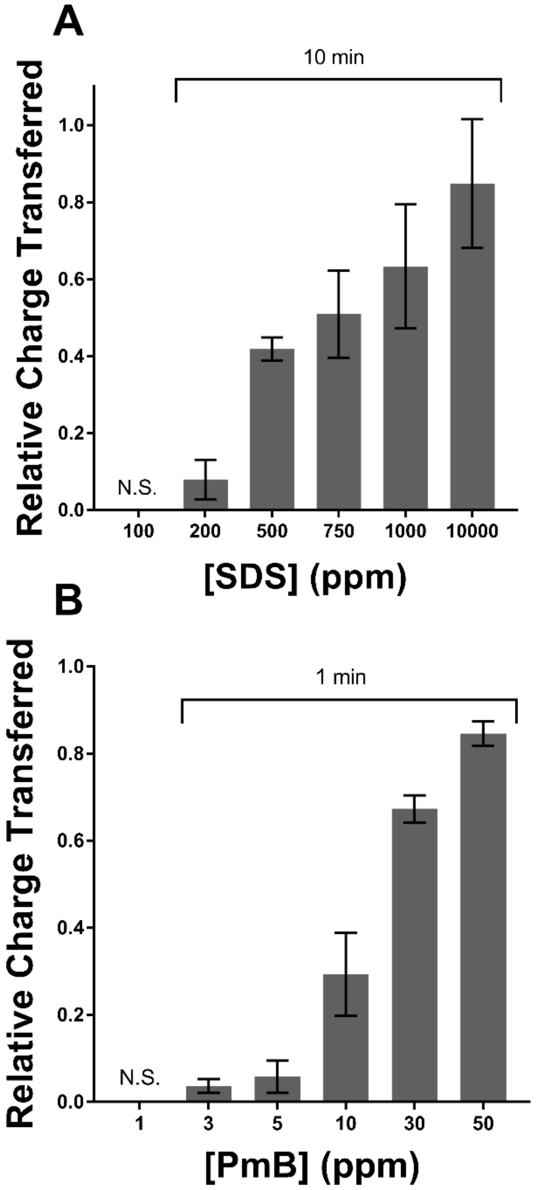

Figure 5.3. Plot of the relative charge transferred (normalized to bare electrodes) in MoC-ECBs prepared with 30 mol% cholesterol exposed to **(A)** SDS and **(B)** PmB. Sensing solutions were prepared in 1x PBS and contained 2 mM KFeCy as a redox reporter. Time indicated is the incubation prior to sensing. Bars represent averages and standard deviations of N = 3 replicate sensors.

To demonstrate the applicability of the sensors to sensing pathogen-derived molecules, we tested the 30 mol% cholesterol-doped MoC-ECBs against the cholesterol-dependent cytolysin pneumolysin (PLY) from *Streptococcus pneumoniae*. The sensors were exposed to PLY at concentrations ranging from 0.2 to 2 ppm and the temporal signal evolution was recorded using CV (Figure 5.S4). Sensors tested in 0.2 ppm PLY (Figure 5.S4A) showed no current response even after 10-minute incubation, indicating no membrane rupturing was achieved and that this concentration is below the LOD of the sensor. MoC-ECBs tested in 1.0 ppm PLY solution (Figure 5.S4B) generated a quantifiable current response with the maximum signal generated at 5 min. When the concentration of PLY was doubled to 2.0 ppm (Figure 5.S4C), the membranes were ruptured much faster where full signal generation was observed in 2.5 min.

A comparison of the cyclic voltammograms generated from MoC-ECBs after 2.5 minutes of exposure to different concentrations of PLY is shown in Figure 5.4A. The legend labels in red correspond to PLY concentrations that did not produce currents that were large enough to be quantifiable, yielding a LOD for PLY of 0.6 ppm. As shown in Figure 5.4b, concentrations between 0.6 and 2 ppm could be reproducibly quantified and produced a linear response (R^2 of 0.972). To evaluate our MoC-ECB's sensitivity for detecting PLY compared to the gold standard test, a hemolysis activity test was performed against sheep red blood cells (RBCs). We used a 1% Triton solution in dialysis buffer as our positive hemolysis control generating 100% lysis. Our negative control of 0% lysis used the dialysis buffer solution. The hemolytic ability of PLY was tested against a concentrated PLY solution followed by diluted PLY samples ranging from 1:10 to 1:32,000 as shown in Figure 5.S5. The PLY concentration was determined to be 54 ppm According to the Bradford Assay performed (shown in Figure 5.S3). The LD50, equivalent to 1 hemolytic unit was determined to be at 1000 times dilution or 54 ppb. To compare, our MoC-ECBs were able to detect PLY concentrations down to 600 ppb or ~ 10 times less sensitive than the gold standard hemolysis assay. The current hemolysis assay requires many sample preparation steps, multistep centrifugation, expensive plate readers, and long turn around times of up to 24 hours. In contrast, the external calibration curve developed for PLY through our MoC-ECBs can be used to determine unknown concentrations of PLY in solution. Furthermore, the 30% M-ECBs are able to achieve rapid detection in 2.5 min at 600 ppb (0.6 µg/mL) and as fast as a few seconds at higher concentrations of 1 ppm (1 µg/mL) and 2 ppm (2 µg/mL). These results are promising and demonstrate the potential for M-ECBs as a platform to quantitatively detect lytic compounds in solution at a rapid and simple way.

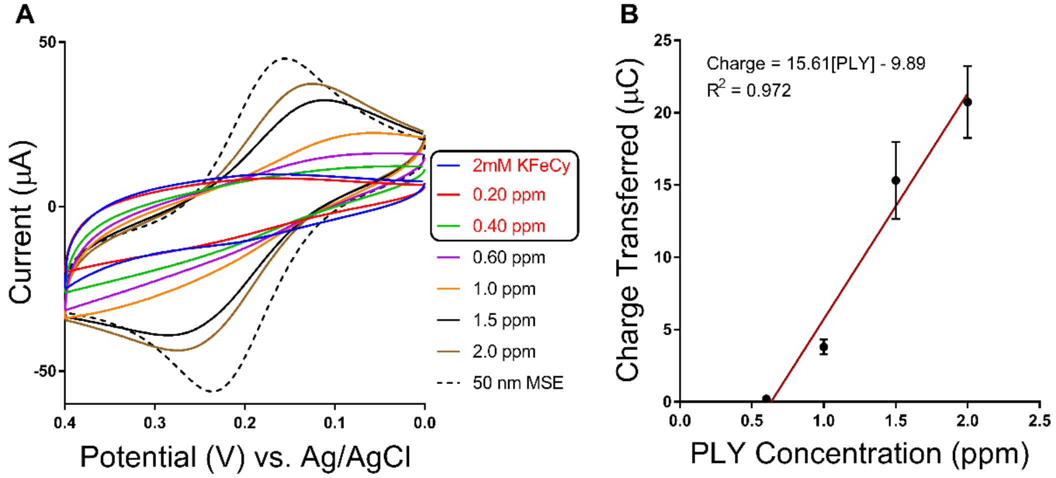

Figure 5.4. Detection of *S. pneumoniae* pneumolysin (PLY) with MoC-ECBs. **(A)** Overlaid cyclic voltammograms generated from MoC-ECBs after 2.5 min exposure to different PLY concentrations. **(B)** Calibration curve quantifying the total charge transferred after 2.5 min exposure to different concentrations of PLY. The LOD for PLY was determined to be 0.6 ppm. Error bars represent the standard deviation of N = 3 replicate experiments.

5.4. CONCLUSIONS

In this work, we fabricated membrane based electrochemical biosensors for the detection of lytic compounds in solution using simple and inexpensive benchtop methods. Microstructured electrodes (MSEs) made by the thermal shrinking of gold-coated polystyrene sheets were passivated with cholesterol-doped DMPC membranes to yield membrane-on-chip electrochemical biosensors (MoC-ECBs). The impact of cholesterol on the stability of the passivating membranes was evaluated by doping the membranes with 0-50 mol% cholesterol and comparing their response to membrane disrupting agents. Increasing the cholesterol content increased the stability of the membranes and made them more resilient against disruption. Membranes doped with 30 mol% cholesterol were then used as biomimetic systems to sense

SDS, PmB, and the cholesterol-dependent cytolysin PLY. Incubation with these lytic agents ruptured the membrane and exposed the underlying electrode surface in a concentration dependent manner, which allowed the generation of signal from a redox reporter in solution. Using this sensing system, we were able to detect concentrations down to 500, 1, and 0.6 ppm for SDS, PmB and PLY, respectively. This biomimetic membrane-on-a-chip device presents a low-cost, quantitative, rapid, and reproducible alternative to detecting membrane disrupting agents with the potential to include additional bio-functionality for the targeted quantitative detection of human pathogens, waterborne pesticides, and pollutants, as well as to evaluate the effect of drugs on membranes.

REFERENCES

(1) Hirst, R. A.; Kadioglu, A.; O'Callaghan, C.; Andrew, P. W. The Role of Pneumolysin in Pneumococcal Pneumonia and Meningitis. *Clin. Exp. Immunol.* **2004**, *138* (2), 195–201. https://doi.org/10.1111/j.1365-2249.2004.02611.x.

(2) Nöllmann, M.; Gilbert, R.; Mitchell, T.; Sferrazza, M.; Byron, O. The Role of Cholesterol in the Activity of Pneumolysin, a Bacterial Protein Toxin. *Biophys. J.* **2004**, *86* (5), 3141–3151. https://doi.org/10.1016/S0006-3495(04)74362-3.

(3) Johnson, S.; Brooks, N. J.; Smith, R. A. G.; Lea, S. M.; Bubeck, D. Report Structural Basis for Recognition of the Pore-Forming Toxin Intermedilysin by Human Complement Receptor CD59. *CellReports* **2013**, *3* (5), 1369–1377. https://doi.org/10.1016/j.celrep.2013.04.029.

(4) Giddings, K. S.; Zhao, J.; Sims, P. J.; Tweten, R. K. Human CD59 Is a Receptor for the Cholesterol-Dependent Cytolysin Intermedilysin. *Nat. Struct. Mol. Biol.* **2004**, *11* (12), 1173–1178. https://doi.org/10.1038/nsmb862.

(5) Bechinger, B.; Lohner, K. Detergent-like Actions of Linear Amphipathic Cationic Antimicrobial Peptides. *Biochim. Biophys. Acta - Biomembr.* **2006**, *1758* (9), 1529–1539. https://doi.org/10.1016/j.bbamem.2006.07.001.

(6) Chaied, I. Saponins as Insecticides. *Tunis. J. Plant Prot.* **2010**, *5* (1), 39–50.

(7) Oakenfull, D. Saponins in Food-A Review. *Food Chem.* **1981**, *7* (1), 19–40. https://doi.org/10.1016/0308-8146(81)90019-4.

(8) Suwalsky, M.; Benites, M.; Villena, F.; Aguilar, F.; Sotomayor, C. P. The Organochlorine Pesticide Heptachlor Disrupts the Structure of Model and Cell Membranes. *Biochim. Biophys. Acta - Biomembr.* **1997**, *1326* (1), 115–123. https://doi.org/10.1016/S0005-2736(97)00019-9.

(9) Ronkainen, N. J.; Halsall, H. B.; Heineman, W. R. Electrochemical Biosensors. *Chem. Soc. Rev.* **2010**, *39* (5), 1747–1763. https://doi.org/10.1039/b714449k.

(10) Ivnitski, D.; Abdel-Hamid, I.; Atanasov, P.; Wilkins, E. Biosensors for Detection of

Pathogenic Bacteria. *Biosensors and Bioelectronics*. 1999, pp 599–624. https://doi.org/10.1016/S0956-5663(99)00039-1.

(11) Ahmed, A.; Rushworth, J. V; Hirst, N. A.; Millner, P. A. Biosensors for Whole-Cell Bacterial Detection. **2014**, *27* (3), 631–646. https://doi.org/10.1128/CMR.00120-13.

(12) Sanvicens, N.; Pastells, C.; Pascual, N.; Marco, M. P. Nanoparticle-Based Biosensors for Detection of Pathogenic Bacteria. *TrAC - Trends Anal. Chem.* **2009**, *28* (11), 1243–1252. https://doi.org/10.1016/j.trac.2009.08.002.

(13) Wen, Y.; Pei, H.; Wan, Y.; Su, Y.; Huang, Q.; Song, S.; Fan, C. DNA Nanostructure-Decorated Surfaces for Enhanced Aptamer-Target Binding and Electrochemical Cocaine Sensors. *Anal. Chem.* **2011**, *83* (19), 7418–7423. https://doi.org/10.1021/ac201491p.

(14) Tavakkoli, N.; Soltani, N.; Mohammadi, F. A Nanoporous Gold-Based Electrochemical Aptasensor for Sensitive Detection of Cocaine. *RSC Adv.* **2019**, *9* (25), 14296–14301. https://doi.org/10.1039/c9ra01292c.

(15) Poltorak, L.; Sudhölter, E. J. R.; de Puit, M. Electrochemical Cocaine (Bio)Sensing. From Solid Electrodes to Soft Junctions. *TrAC - Trends Anal. Chem.* **2019**, *114*, 48–55. https://doi.org/10.1016/j.trac.2019.02.025.

(16) Demir, B.; Yilmaz, T.; Guler, E.; Gumus, Z. P.; Akbulut, H.; Aldemir, E.; Coskunol, H.; Colak, D. G.; Cianga, I.; Yamada, S.; et al. Polypeptide with Electroactive Endgroups as Sensing Platform for the Abused Drug 'Methamphetamine' by Bioelectrochemical Method. *Talanta* **2016**, *161* (September), 789–796. https://doi.org/10.1016/j.talanta.2016.09.042.

(17) Ebrahimi, M.; Johari-Ahar, M.; Hamzeiy, H.; Barar, J.; Mashinchian, O.; Omidi, Y. Electrochemical Impedance Spectroscopic Sensing of Methamphetamine by a Specific Aptamer. *BioImpacts* **2012**, *2* (2), 91–95. https://doi.org/10.5681/bi.2012.013.

(18) Wang, J. Electrochemical Biosensors: Towards Point-of-Care Cancer Diagnostics. *Biosens. Bioelectron.* **2006**, *21* (10), 1887–1892.

https://doi.org/10.1016/j.bios.2005.10.027.

(19) Soper, S. A.; Brown, K.; Ellington, A.; Frazier, B.; Garcia-Manero, G.; Gau, V.; Gutman, S. I.; Hayes, D. F.; Korte, B.; Landers, J. L.; et al. Point-of-Care Biosensor Systems for Cancer Diagnostics/Prognostics. *Biosens. Bioelectron.* **2006**, *21* (10), 1932–1942. https://doi.org/10.1016/j.bios.2006.01.006.

(20) Wang, J. Electrochemical Nucleic Acid Biosensors. *Anal. Chim. Acta* **2002**, *469* (1), 63–71. https://doi.org/10.1016/S0003-2670(01)01399-X.

(21) Wang, J.; Rivas, G.; Cai, X.; Palecek, E.; Nielsen, P.; Shiraishi, N.; Dontha, N.; Luo, D.; Parrado, C.; Chicharro, M.; et al. DNA Electrochemical Biosensors for Environmental. A Review. *Anal. Chim. Acta* **1997**, *347*, 1–8.

(22) Drummond, T. G.; Hill, M. G.; Barton, J. K. Electrochemical DNA Sensors. *Nat. Biotechnol.* **2003**, *21* (10), 1192–1199. https://doi.org/10.1038/nbt873.

(23) Mettakoonpitak, J.; Boehle, K.; Nantaphol, S.; Teengam, P.; Adkins, J. A.; Srisa-Art, M.; Henry, C. S. Electrochemistry on Paper-Based Analytical Devices: A Review. *Electroanalysis* **2016**, *28* (7), 1420–1436. https://doi.org/10.1002/elan.201501143.

(24) Bandodkar, A. J.; Wang, J. Non-Invasive Wearable Electrochemical Sensors: A Review. *Trends Biotechnol.* **2014**, *32* (7), 363–371. https://doi.org/10.1016/j.tibtech.2014.04.005.

(25) Elmore, S. Apoptosis: A Review of Programmed Cell Death. *Toxicol. Pathol.* **2007**, *35* (4), 495–516. https://doi.org/10.1080/01926230701320337.

(26) Edidin, M. Lipids on the Frontier: A Century of Cell-Membrane Bilayers. *Nat. Rev. Mol. Cell Biol.* **2003**, *4* (5), 414–418. https://doi.org/10.1038/nrm1102.

(27) Kim, H. J.; Bennetto, H. P.; Halablab, M. A. A Novel Liposome-Based Electrochemical Biosensor for the Detection of Haemolytic Microorganisms. *Biotechnol. Tech.* **1995**, *9* (6), 389–394. https://doi.org/10.1007/BF00160823.

(28) Kim, H. J.; Bennetto, H. P.; Halablab, M. A.; Choi, C.; Yoon, S. Performance of an

Electrochemical Sensor with Different Types of Liposomal Mediators for the Detection of Hemolytic Bacteria. *Sensors Actuators, B Chem.* **2006**, *119* (1), 143–149. https://doi.org/10.1016/j.snb.2005.12.013.

(29) Tun, T. N.; Cameron, P. J.; Jenkins, A. T. A. Sensing of Pathogenic Bacteria Based on Their Interaction with Supported Bilayer Membranes Studied by Impedance Spectroscopy and Surface Plasmon Resonance. *Biosens. Bioelectron.* **2011**, *28* (1), 227–231. https://doi.org/10.1016/j.bios.2011.07.023.

(30) Cranfield, C. G.; Cornell, B. A.; Grage, S. L.; Duckworth, P.; Carne, S.; Ulrich, A. S.; Martinac, B. Transient Potential Gradients and Impedance Measures of Tethered Bilayer Lipid Membranes: Pore-Forming Peptide Insertion and the Effect of Electroporation. *Biophys. J.* **2014**, *106* (1), 182–189. https://doi.org/10.1016/j.bpj.2013.11.1121.

(31) Andersson, J.; Fuller, M. A.; Wood, K.; Holt, S. A.; Köper, I. A Tethered Bilayer Lipid Membrane That Mimics Microbial Membranes. *Phys. Chem. Chem. Phys.* **2018**, *20* (18), 12958–12969. https://doi.org/10.1039/c8cp01346b.

(32) Gabardo, C. M.; Zhu, Y.; Soleymani, L.; Moran-Mirabal, J. M. Bench-Top Fabrication of Hierarchically Structured High-Surface-Area Electrodes. *Adv. Funct. Mater.* **2013**, *23* (24), 3030–3039. https://doi.org/10.1002/adfm.201203220.

(33) Saem, S.; Zhu, Y.; Luu, H.; Moran-Mirabal, J. Bench-Top Fabrication of an All-PDMS Microfluidic Electrochemical Cell Sensor Integrating Micro/Nanostructured Electrodes. *Sensors (Switzerland)* **2017**, *17* (4). https://doi.org/10.3390/s17040732.

(34) Sonney, S.; Shek, N.; Moran-Mirabal, J. M. Rapid Bench-Top Fabrication of Poly(Dimethylsiloxane)/Polystyrene Microfluidic Devices Incorporating High-Surface-Area Sensing Electrodes. *Biomicrofluidics* **2015**, *9* (2). https://doi.org/10.1063/1.4918596.

(35) Zhu, Y.; Moran-Mirabal, J. Highly Bendable and Stretchable Electrodes Based on Micro/Nanostructured Gold Films for Flexible Sensors and Electronics. *Adv. Electron.*

Mater. **2016**, *2*, 1500345. https://doi.org/10.1002/aelm.201500345.

(36) Saem, S.; Abbaszadeh Amirdehi, M.; Greener, J.; Zarabadi, M. P.; Moran-Mirabal, J. M. Microstructured Anodes by Surface Wrinkling for Studies of Direct Electron Transfer Biofilms in Microbial Fuel Cells. *Adv. Mater. Interfaces* **2018**, *5* (13), 1800290. https://doi.org/10.1002/admi.201800290.

(37) Saem, S.; Shashid, O.; Khondker, A.; Moran-Hidalgo, C.; Rheinstädter, M. C.; Moran-Mirabal, J. Benchtop-Fabricated Lipid-Based Electrochemical Sensing Plat-Form for the Detection of Membrane Disrupting Agents. *Appl. Mater. Inerfaces* **2019**, *Submitted.*

(38) Khelashvili, G.; Harries, D. How Sterol Tilt Regulates Properties and Organization of Lipid Membranes and Membrane Insertions. *Chem. Phys. Lipids* **2013**, *169*, 113–123. https://doi.org/10.1016/j.chemphyslip.2012.12.006.

(39) Xu, F.; Rychnovsky, S. D.; Belani, J. D.; Hobbs, H. H.; Cohen, J. C.; Rawson, R. B. Dual Roles for Cholesterol in Mammalian Cells. *Proc. Natl. Acad. Sci.* **2005**, *102* (41), 14551–14556. https://doi.org/10.1073/pnas.0503590102.

(40) Ali, M. R.; Cheng, K. H.; Huang, J. Assess the Nature of Cholesterol-Lipid Interactions through the Chemical Potential of Cholesterol in Phosphatidylcholine Bilayers. *Proc. Natl. Acad. Sci.* **2007**, *104* (13), 5372–5377. https://doi.org/10.1073/pnas.0611450104.

(41) Trandum, C.; Westh, P.; Jørgensen, K.; Mouritsen, O. G. A Thermodynamic Study of the Effects of Cholesterol on the Interaction between Liposomes and Ethanol. *Biophys. J.* **2000**, *78* (5), 2486–2492. https://doi.org/10.1016/S0006-3495(00)76793-2.

(42) Gerl, M. J.; Sampaio, J. L.; Urban, S.; Kalvodova, L.; Verbavatz, J. M.; Binnington, B.; Lindemann, D.; Lingwood, C. A.; Shevchenko, A.; Schroeder, C.; et al. Quantitative Analysis of the Lipidomes of the Influenza Virus Envelope and MDCK Cell Apical Membrane. *J. Cell Biol.* **2012**, *196* (2), 213–221. https://doi.org/10.1083/jcb.201108175.

(43) Liu, S. L.; Sheng, R.; Jung, J. H.; Wang, L.; Stec, E.; O'Connor, M. J.; Song, S.;

Bikkavilli, R. K.; Winn, R. A.; Lee, D.; et al. Orthogonal Lipid Sensors Identify Transbilayer Asymmetry of Plasma Membrane Cholesterol. *Nat. Chem. Biol.* **2017**, *13* (3), 268–274. https://doi.org/10.1038/nchembio.2268.

(44) Taylor, S. D.; Sanders, M. E.; Tullos, N. A.; Stray, S. J.; Norcross, E. W.; McDaniel, L. S.; Marquart, M. E. The Cholesterol-Dependent Cytolysin Pneumolysin from Streptococcus Pneumoniae Binds to Lipid Raft Microdomains in Human Corneal Epithelial Cells. *PLoS One* **2013**, *8* (4), 1–11. https://doi.org/10.1371/journal.pone.0061300.

(45) Zavascki, A. P.; Goldani, L. Z.; Li, J.; Nation, R. L. Polymyxin B for the Treatment of Multidrug-Resistant Pathogens: A Critical Review. *J. Antimicrob. Chemother.* **2007**, *60* (6), 1206–1215. https://doi.org/10.1093/jac/dkm357.

(46) Shewell, L. K.; Harvey, R. M.; Higgins, M. A.; Day, C. J.; Hartley-Tassell, L. E.; Chen, A. Y.; Gillen, C. M.; James, D. B. A.; Alonzo, F.; Torres, V. J.; et al. The Cholesterol-Dependent Cytolysins Pneumolysin and Streptolysin O Require Binding to Red Blood Cell Glycans for Hemolytic Activity. *Proc. Natl. Acad. Sci.* **2014**, *111* (49), E5312–E5320. https://doi.org/10.1073/pnas.1412703111.

(47) Khondker, A.; Alsop, R. J.; Dhaliwal, A.; Saem, S.; Moran-Mirabal, J. M.; Rheinstädter, M. C. Membrane Cholesterol Reduces Polymyxin B Nephrotoxicity in Renal Membrane Analogs. *Biophys. J.* **2017**, *113* (9), 2016–2028. https://doi.org/10.1016/j.bpj.2017.09.013.

(48) Almeida, P. F. F.; Thompson, T. E. Lateral Diffusion in the Liquid Phases of Dimyristoylphosphatidylcholine/Cholesterol Lipid Bilayers : A Free Volume Analysis. *Biochemistry* **1992**, *31* (29), 6739–6747. https://doi.org/10.1021/bi00144a013.

(49) Khondker, A.; Dhaliwal, A. K.; Saem, S.; Mahmood, A.; Fradin, C.; Moran-Mirabal, J.; Rheinstädter, M. C. Membrane Charge and Lipid Packing Determine Polymyxin-Induced Membrane Damage. *Commun. Biol.* **2019**, *2* (1), 67. https://doi.org/10.1038/s42003-019-0297-6.

(50) Heerklotz, H. Interactions of Surfactants with Lipid Membranes. *Q. Rev. Biophys.* **2008**, *41* (3–4), 205–264. https://doi.org/10.1017/S0033583508004721.

SUPPLEMENTARY INFORMATION

Cholesterol Enriched Membrane-based Electrochemical Biosensor for the Detection of Waterborne Lytic Compounds

Sokunthearath Saem, Osama Shashid, Nadine Beganovic, and Jose Moran-Mirabal*

Department of Chemistry and Chemical Biology

McMaster University, Hamilton, Ontario, Canada

* Correspondence: mirabj@mcmaster.ca; Tel.: +1-905-525-9140

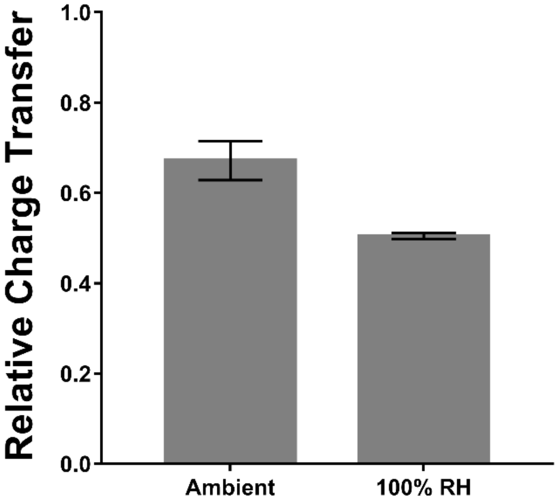

Figure 5.S1. Plot of the relative charge transferr comparing annealing conditions for DMPC:Chol membranes containing 30% cholesterol. The MoC-ECBs were tested in a 15 ml 1xPBS, 500 ppm SDS and 2 mM KFeCy solution. The relative charge transfer values shown were acquired at the 20 min time point when signal had reached a stable value. Error bars represent standard deviation of N =3 replicate devices. The lower charge transfer of the 100% RH samples indicate greater sensor passivation and membrane stability. Additionally, the smaller errors also suggest increased sensor reproducibility.

Measurement of the Critical Micelle Concentration using Dynamic Light Scattering (DLS)

The critical micelle concentrations of SDS and PmB in the sensing solution (2 mM KFeCy in 1xPBS) was determined using a Zetasizer Nano ZS (Malvern Panalytical Inc., Westborough, MA, USA) instrument fitted with a Non-Invasive Backscattering (NIBS) optics with a size resolution range between 0.3 nm to 10.0 µm. The DLS measurements were performed at 25°C with a detection angle of 173° using a He-Ne LASER light source (633 nm) at PmB and SDS concentrations ranging from 1 to 50,000 ppm.

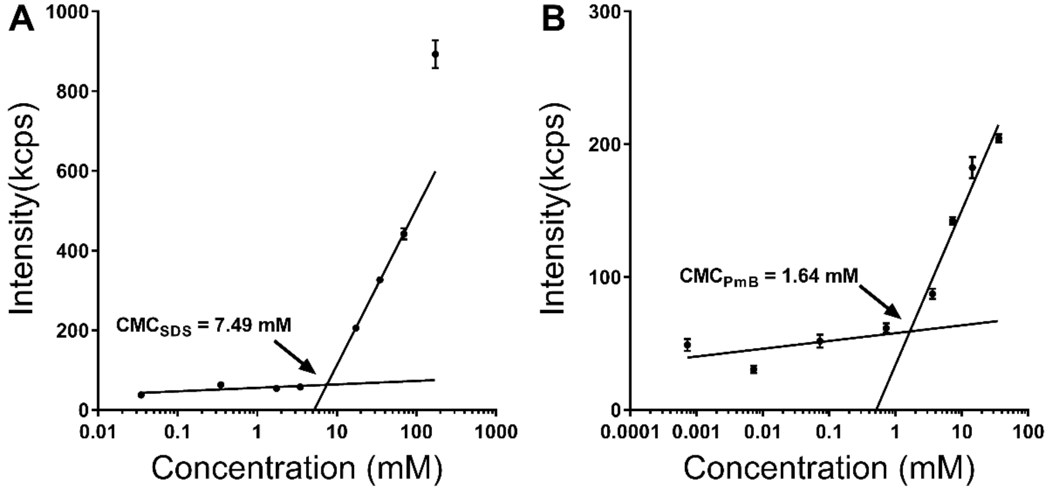

Figure 5.S2. Dynamic Light Scattering (DLS) plots (derived count rate) at known concentrations of **(A)** SDS of 1 – 50,000 ppm (CMC = 2200 ppm or 7.5 mM) and **(B)** PmB of 1 – 50,000 ppm (CMC = 2300 ppm or 1.6 mM). Points on the plot represent mean values with error bars as standard deviation of N =3.

Bradford Assay for Pneumolysin Concentration Determination

The Bradford Assay was used to quantify the concentration of PLY protein. Bovine Serum Albumin (BSA, Sigma-Aldrich, Oakville, ON, Canada) calibration standards were prepared from a 2 mg/mL stock solution in 1x PBS. A serial dilution was performed in PBS solution (pH 7.4) to obtain standards ranging from 5 to 1500 ppm. Each standard solution was vortexed prior to preparing the following standard. For each cuvette, 20 µL of each standard was added to a 1 mL mixture of 1:4 Coomassie Brilliant Blue G-250 (CBB, Thermo Fisher Scientific, Burlington, ON, Canada) dye to Milli-Q H_2O. All standard samples were prepared in triplicate and incubated for 5 minutes prior to analysis. Prior to each run, the spectrophotometer was blanked at 595nm using 1 mL of 1xPBS. The absorbance of each replicate was measured at 595nm starting with the lowest concentration of 5 µg/mL to 1000 µg/mL. The PLY solution of unknown concentration was defrosted (from -20ºC) and prepared identically to the calibration solutions in triplicate. A linear regression of the absorbance vs BSA concentration was performed to obtain the concentration of the unknown PLY.

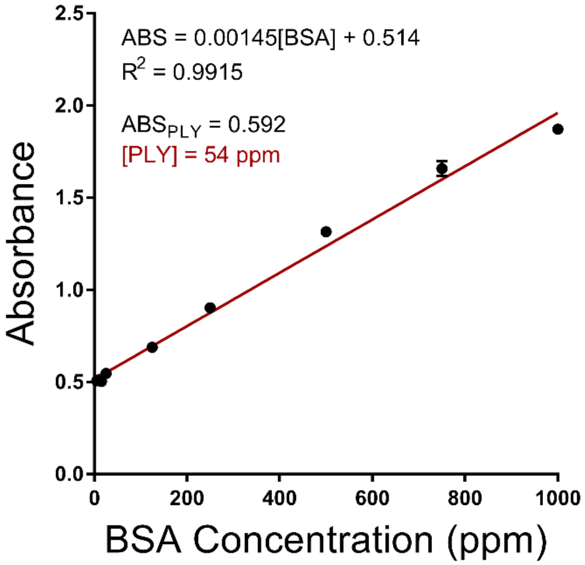

Figure 5.S3. Bradford Assay calibration curve using BSA as protein standard to determine the unknown PLY concentration. The PLY concentration from the stock solution was determined to be 54 ppm.

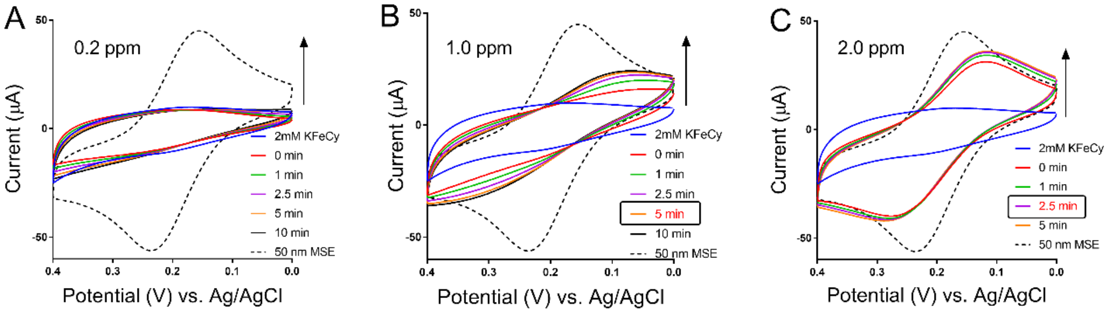

Figure 5.S4. Overlaid CV plots showing the kinetic profile of 30 mol% cholesterol doped MoC-ECBs tested against **(A)** 0.2 ppm PLY, **(B)** 1.0 ppm PLY, and **(C)** 2.0 ppm PLY. Boxed and highlighted in red are the incubation times where maximum signal was achieved. Sensors exposed to 0.2 ppm PLY did not generate Faradaic current indicating insufficient membrane lysis had occurred.

Hemolysis activity assay

A 1 mL volume of sheep red blood cells (RBCs) was added to a 1.5 mL tube and centrifuged at 2000 rpm for 5 min at room temperature. The supernatant was removed and replaced with 1 mL of 1xPBS. This process was repeated 5 – 6x until the supernatant was completely clear resulting in ~30% RBCs. The RBC suspension was diluted 1:10 with 1xPBS to obtain ~3% RBCs. 100 μL aliquots were added to the wells of 96-well round bottom plates. PLY was added to the 3% RBC wells to achieve the desired concentrations as shown in Figure 5.S5 and the plates were incubated at 37°C for 30 min. The OD of the supernatant was measured at 540 nm to determine the hemolytic activity. The LD_{50} shown in Figure 5.S5 is the concentration at which 50% of blood cells are lysed and is equivalent to 1 hemolytic unit.

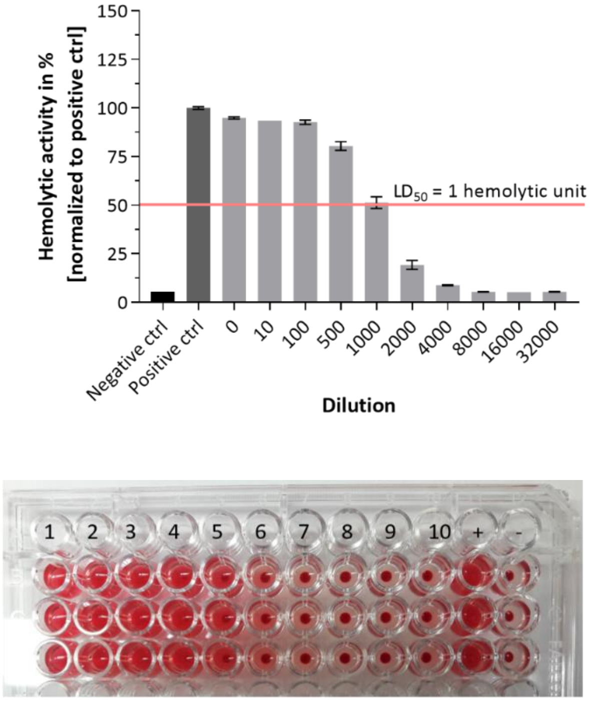

Figure 5.S5. Blood hemolysis assay using sheep RBCs to determine PLY hemolytic activity. The dilution factors are as follows: (1) undiluted pneumolysin, (2) 1:10, (3) 1:100, (4) 1:500, (5) 1:1000, (6) 1:2000, (7) 1:4000, (8) 1:8000, (9) 1:16000, (10) 1:32000, (+) control 100% lysis with 1% Triton, and (-) control 0% lysis with buffer.

Chapter 6: Conclusions and Future Outlook

6.1. CONCLUSIONS

The lack of accessible healthcare technologies in developing countries makes it difficult for people in these regions to live a long and healthy life. Some critical resources that are often lacking in developing nations are safe drinking water, clean energy, and access to healthcare diagnostics. This is largely due to the costly capital investment in laboratories, equipment, highly trained technicians, and technical knowledge. Additionally, most developing countries have significant populations in rural pockets that are far from each other. This presents a challenging logistical problem because most advanced healthcare technologies are centralized in highly populated cities. Therefore, researchers have increased efforts to develop novel biotechnologies with a large focus on making them comply with the ASSURED (affordable, sensitive, specific, user-friendly, rapid and robust, equipment-free, and deliverable to end-users) criteria. One platform that shows promise are portable electrochemical sensors. More specifically, electrochemical biosensors (ECBs) that utilize biological compounds such as proteins, DNA, antibodies, and phospholipid membranes as specific recognition elements and miniaturized high surface area electrodes as electrochemical transducers. On example of a success story is the electrochemical enzymatic glucose sensor first introduced by Leland C. Clark Jr. and Champ Lyons. The sensor allowed patients with diabetes to monitor their blood glucose levels throughout the day. This simple invention helped save the lives of many affected by diabetes and still represents 80% of the biosensing market today. The success of the personal glucose sensor has brought a new perspective to healthcare diagnostics and stimulated new approaches in the design of medical devices. By taking the complexity out of the device operation and data analysis, people without technical training can perform high quality medical testing in the comfort of their own home. Nowadays, researchers are developing new technologies with an emphasis on portability, ease of use, sensitivity, reproducibility, and robustness. The contents of this thesis aim to contribute to this growing field of inexpensive, sensitive, accurate and simple to use sensing devices.

Chapter 1 highlighted the limitations of existing sensing technologies from an accessibility point of view for developing countries and reviewed approaches to produce high sensitivity, portable electrochemical sensors. Although current biotechnologies have high sensitivity, specificity, and reproducibility, the cost to own, operate, and maintain is much too high to be feasible in resource-limited environments. Therefore, researchers have turned to low-cost microfabrication approaches to make portable analytical technologies. Specifically, bench-top microfabrication is of interest due to its process simplicity, scalability, low-cost, and low barrier to entry. Unlike traditional microfabrication techniques that require expensive cleanroom facilities, bench-top fabrication focuses on developing processes that are safe to perform on the laboratory bench with high reproducibility, robustness, and portability. The development and maturation of bench-top microfabrication techniques have already enabled low-cost and rapid production of prototype devices for applications in drug discovery, stretchable electronics, heavy metal detection, illegal drug screening, infectious disease detection, and tissue engineering, among many others. However, increasing portability implies that the physical footprint of the devices produced must be much smaller. In the case of electrochemical biosensors, this means that the sensitivity of the device can suffer. To improve the sensitivity and portability of ECBs, research groups have attempted to modify the electrode surface to enhance electrochemical signal output during sensing. A simple way to enhance the electroactive surface area (EASA) of an electrode is by introducing nano/microstructures; in one approach, this can be achieved through-heat induced polymeric contraction of surface metallic thin films. Whitesides and colleagues introduced a technique in the 1990's where polydimethyl siloxane (PDMS) elastomers were heated to induce thermal expansion followed by surface deposition of metallic thin films such as gold, silver, and platinum. Others have used thermally-induced shrinking of shape-memory polymers (SMPs) to create highly tunable nano/microstructured electrodes. The shrinking and wrinkling in this process helps to reduce the electrode footprint by 84%, with a concomitant increase the EASA by 600%,compared to devices with planar electrodes. Further enhancement of the wrinkled electrodes has been explored with hierarchical nanostructuring through electrochemical deposition and electrochemical nanoroughening. These simple bench-top techniques for electrode miniaturization and enhancement have helped to mitigate the sensitivity issues of portable devices and led to the development of many new technologies in the fields of infectious diseases, oncology, tissue engineering, wearable electronics, energy capture, among others.

Chapter 2 introduced the use of the SMPs to produce microstructured electrodes (MSEs) made of gold (Au) and platinum (Pt) for integration within an all-PDMS microfluidic (μF) device for the electrochemical detection of adherent cells. To our knowledge, this device was the first all-PDMS μF device that combined the high sensitivity of MSEs in an on-chip electrochemical sensor. Through a series of bonding optimization experiments, we found that the PDMS to PDMS-structured electrode bonding protocol to fabricate the μF chip had excellent bond strength, able to withstand up to 100 mL/min flow rates. The sensing capabilities of the on-chip electrochemical cell were demonstrated by using cyclic voltammetry to monitor the adhesion of murine 3T3 fibroblasts in the presence of a redox reporter. Upon cell adhesion, the charge transfer across the working electrode was reduced. This signal suppression was used as the detection mechanism, allowing the detection of the binding of as few as 24 cells. This all-PDMS μF sensing platform has the potential to incorporate other techniques such as fluorescence microscopy to perform cross-method analysis. The platform demonstrates the potential for low-cost bench-top fabrication as an effective method to develop LoC technologies and bring PoC diagnostics closer to the patients' bedside.

Sustainable energy is an increasing concern, especially in developing countries with limited resources. Chapter 3 utilized the SMPs to produce hierarchical wrinkled gold surfaces as high-surface area miniature bioanodes in a microbial fuel cell (MFC) for enhanced energy capture. In this work, we studied the effect of the wrinkled anode topography on the power output from the direct electron transfer process generated by *Geobacter sulfurreducens* biofilms, avoiding competing effects associated with additive manufacturing approaches. The resulting structures contained wrinkle heights and spacings in range of the < 1 – 8 μm, and 4 – 25 μm, respectively. The different wrinkle sizes made from varying Au thickness contained the same EASA. However, with respect to energy capture the tall and well-spaced features performed best. Anodes with the shortest, most closely packed structures, did not perform any better than planar surfaces with the same footprint and 6-fold lower EASA. This result suggests that large interfold spacing can accommodate increased bacterial packing density at the electrode surface. Therefore, structural dimensions rather than total EASA is proposed to have greater contribution to future bioanode fabrication in MFCs that utilize direct electron transfer from electroactive biofilms.

As mentioned in Chapter 1, waterborne pathogens and synthetic contaminants present a large global issue. Of particular concern are compounds that disrupt the cell membrane (i.e. lytic compounds). This limits the amount of safe drinking water available in developing nations especially in times of drought. In Chapter 4 we developed an inexpensive electrochemical biosensor for the rapid detection of membrane disrupting agents. 1,2-dimyristoyl-*sn*-glycero-3-phosphocholine (DMPC) phospholipid membranes were used to passivate the MSEs, preventing the interaction of a redox reporter with the electrode surface while the membrane remained intact. When the sensors were incubated with solutions containing a lytic agent (*i.e.*, SDS, PmB), the membrane dissolved allowing the reporter molecules to reach the electrode surface and undergo redox cycling to generate an electrochemical signal. We optimized the sensor fabrication conditions (*i.e.,* gold wrinkle size, membrane deposition and annealing conditions) and determined that the deposition of DMPC membranes from 200 μg/mL solutions onto MSEs made from 20 nm-thick Au films, followed by annealing at 50°C for 1 hour produced the most reproducible and sensitive electrochemical biosensors (ECBs). We were able to detect SDS and PmB within minutes down to concentrations of 10 and 1 ppm, respectively, highlighting the excellent sensitivity afforded by the MSEs. This membrane-based electrochemical biosensing platform offers fast detection times, low-cost, and reproducibility, representing a first step towards the realization of Membrane-on-Chip (MoC) devices with potential for future applications in diagnostics targeted against infectious bacteria, field testing for harmful pesticides, and antimicrobial drug testing.

The membrane-based ECB developed in Chapter 4 is proof of concept of a working platform for membrane-based detection that offers a high degree of portability and rapid turnaround times that is lacking in current gold-standard techniques. However, real biological membranes are much more complex and are made up of more than a single type of phospholipid. In fact, biological membranes consist of a complex mixture of phospholipid variants, membrane proteins, and carbohydrates to help regulate the flux of small molecules between the internal and external cellular environments. This strict regulation helps to maintain cell viability and allow cell proliferation. In Chapter 5 we increased the biomimetic membrane complexity by introducing cholesterol. Cholesterol is known to modulate the membrane fluidity, depending on the type of phospholipid content found in the cell membrane. We combined cholesterol with DMPC to create highly stable supported biomimetic membranes on MSEs. We employed the same sensing mechanism discussed in Chapter 4, where the signal generated in the MoC-ECBs is proportional to the concentration of the lytic compound in solution. We observed increased membrane stability when cholesterol was added to DMPC, validated with cyclic voltammetry (CV) experiments where lower signal generation was observed with increasing cholesterol content. Additionally, sensors prepared with 30 mol% cholesterol were capable of detecting SDS down to 500 ppm, PmB down to 1 ppm, and pneumolysin (PLY, a hemolytic virulence factor) down to 600 ppb. Using CV, we produced a calibration curve for PLY with an R^2 value of 0.972 that can be used to quantify an unknown concentration of PLY. This MoC-ECB device offers a low-cost, quantitative, rapid, and reproducible alternative to detecting lytic agents with the potential to incorporate additional bio-functionality for the targeted detection of human pathogens, waterborne pesticides, and pollutants, as well as to evaluate the effect of drugs on membranes.

6.2. FUTURE OUTLOOK

This thesis presented the methodology to fabricate highly sensitive and miniaturized wrinkled electrodes for electrochemical applications using a low-cost bench-top technique that enables affordability, accessibility, sensitivity and portability. We have demonstrated some potential applications of such electrodes in the first all PDMS μF electrochemical cell sensing, in MFCs for enhanced energy capture, and in electrochemical biosensing as a membrane-based ECBs. The future seems promising for this versatile fabrication platform as numerous materials can be incorporated onto SMPs to form wrinkles, such as cellulose, graphene, carbon nanotubes, hydrogels, and polymer composites.

Chapter 2 presented an all PDMS cell sensor using NMSEs to enhance the electrochemical sensitivity. This was a good first proof-of-concept to highlight the bench-top fabrication and implementation of an all in one electrochemical sensing device. However, this sensor lacked specificity and relevant biological application. Moving forward, we can introduce specificity to the platform through the use of biological recognition elements such as aptamers, proteins, and antibodies to name a few. Using gold-thiol chemistry, we can immobilize these biorecognition elements on the surface of the working electrode to capture our analyte of interest. One potential application is in developing microfluidic based electrochemical immunoassays for the detection of circulating tumor cells and cannabinoids in blood or other clinically relevant samples. In this way, the sensor can be integrated in series to existing technologies used to draw patient blood while monitoring the effectiveness of the therapeutic treatments. This technology would enable clinicians to deliver medical diagnostics to the patients' bedside. Another option is to produce an array sensor consisting of 4 – 10 working electrodes that can be functionalized with thiolated aptamers selective for range of small molecules for illegal drug testing applications. This electrode array could be targeted to detecting the top 10 most trafficked drugs such a methamphetamine, cocaine, and cannabis. Additionally, the all PDMS chips should allow the integration of additional analysis techniques such as fluorescence microscopy and SERS as a form of cross-method analysis.

Electrochemical and polarization experiments in Chapter 3 determined that the increased wrinkle sizes from the MSEs produced microbial fuel cells with power outputs two times greater than the planar and smaller wrinkle size MSEs. This was attributed to the radial accessibility that the bacteria has to the 2.5D topography allowing increased electron transfer between bacterial biofilms and the gold anode surface. Since the wrinkle size is determined by the stiffness mismatch between the underlying polymer substrate and the top gold thin films, a larger mismatch can be used to produce larger wrinkle sizes. Therefore, to increase the wrinkle sizes proven to benefit power output in MFCs, we can either increase the top layer film stiffness or modify the underlying polymer substrate to reduce the intrinsic stiffness. One limitation to increasing gold thickness is that beyond the 400 nm thickness used, the gold begins to crack upon shrinking as the compressive stress becomes too large to dissipate by wrinkling. To avoid film cracking but still increase the wrinkle size, we can explore new shape-memory polymeric substrates. Polyolefin shrink-wrap could offer a softer substrate that increases the stiffness mismatch while also contain a larger shrinking ratio where previously reported values are as high as 95%. The option to modify the substrate or film stiffness would enable us to optimize for the best fabrication conditions to produce the largest possible wrinkle sizes for MFC power capture enhancement.

Chapters 4 and 5 introduced a novel supported membrane-based electrochemical biosensor for the detection of lytic agents using NMSEs as solid membrane supports. We were able to showcase the detection of SDS, PmB, and PLY with limits of detection in the range of ppb to ppm in seconds to minutes. Cholesterol doping showed signal improvement in sensors tested against cholesterol specific lytic agents like PLY but signal suppression for SDS and PmB. This platform has extremely high potential for sensing applications in the area of portable lytic agent detection in water, urine, blood, and other clinically relevant samples. Although we showed successful sensing using biomimetic membrane systems, we can begin to isolate and deposit real cell membranes onto the NMSEs and use the membrane surface proteins as selective capturing agents for targeted detection of clinically relevant analytes. For example, intermedilysin is a cytotoxic protein expressed by *Staphylococcus intermedius* bacteria which requires both membrane-bound cholesterol and CD59 membrane protein found in human red blood cells to form pores and lyse the membrane. Therefore, by using human red blood cell membranes, we can produce ECBs capable of detecting hemolytic compounds specific to humans that would otherwise be undetected using the current gold standard blood agar test. Mammalian cell membranes can also be isolated through artificial cell blebbing techniques and integrated onto this platform. Similarly, bacterial membranes can be incorporated for antibiotic drug screening applications. These membrane-based ECBs can also be used to evaluate and benchmark the effectiveness of new surfactants against current commercial standards like SDS or Triton-X. With the capability to change membrane types supported on the MSEs, a range of validation tests can be designed.

In an attempt to consolidate fabrication processes and make them bench-top compatible, we can explore alternative methods of metal deposition onto polymeric substrates and replace the instrument-intensive, lengthy and costly sputter deposition step. One option is to use polydopamine to coat the polymeric surfaces and through electroless metal deposition, create metallic working electrodes. Polymerization of dopamine at a solid-liquid interface has been shown to produce uniform thin polydopamine coatings on metallic, polymeric, and ceramic surfaces. These polydopamine coatings can be used to nucleate metallic salts from solution to grow thin films. We can use this technique as a low-cost bench-top approach to making metallic electrodes out of copper, silver, or gold.

We have shown electroactive surface area enhancement of planar gold electrodes by ~6x through our heat induced shrinking method. This results in a 2.5D wrinkled electrodes, however the electroactive surface area can be further enhanced by introducing three-dimensional nanoporosity or high aspect ratio nanostructures onto the wrinkled gold films. For example, in the presence of sulfuric acid, high voltage and high frequency electrochemical pulsing can be used to dissolve and redeposit the gold onto itself to create nanopores and nanostructures. This should increase the electroactive surface area as 2.5D wrinkles turn into hierarchical 3D porous networks. The nanopores and high surface area has been shown to increase packing density of DNA and antibody-based ECBs. Since the sensitivity is often determined by the number of DNA or antibody probes that can be immobilized on a electrode, having increased probe packing density should increase the biosensor sensitivity. This would present a very cost-effective bench-top approach to making hierarchically structured porous gold electrodes without the traditional use of dual alloy deposition and metal stripping.

Last, some preliminary CV experiments performed on wrinkled electrodes made from thin gold films (< 50nm) hinted at ultramicroelectrode properties. UMEs offer increased signal-to-noise ratio for electrochemical sensing due to their radial diffusion at the tips and small size versus the large diffusion layer. We can exploit the controllable wrinkle spacing and height produced using our shrinking method to fabricate UMEAs. Using an insulating material (e.g., photoresist, Parylene) we can fully passivate the surface of the MSEs. Upon air plasma oxidation or reactive ion etching, we can etch away the insulating material to expose the tips of the wrinkles. The exposed tips can be fabricated to contain tip spacing and size based on the gold thickness and etching time. This could prove to be an excellent low-cost alternative to traditional photolithography used today to make UMEAs. These examples only capture a small fraction of the potential applications involving structured wrinkled materials. The work included in this thesis is an important start to demonstrating proof of concept applications for the young and growing field of wrinkled devices with potential to impact the work of future generations of researchers and consumers of successful biotechnologies.